Dissertation
Submitted to the
Combined Faculty of Mathematics,
Engineering and Natural Sciences
of Heidelberg University, Germany
for the degree of
Doctor of Natural Sciences

Put forward by
M.Sc. Andreas Fink

born in: Mettmann, Germany
Oral examination: 12.07.2024

Engineering Polarity in Bottom-Up Synthetic Cells

Referees: Prof. Dr. Joachim P. Spatz
Prof. Dr. Kerstin Göpfrich

Abstract

Polarity and spatial molecular organization are key features found in life at scales from the single cell to the whole organism. It determines cell fate in asymmetric cell division as well as the direction in migrating cells. Polarity in cells can generally be defined as a result of an asymmetric distribution of molecules and evolves in directly observable changes such as rearrangement of cell shape and actin distribution. Cell deformation, induced by adhesion to micropatterned surfaces, is used to standarize and normalize cells and can control polarity depending on the underlying shape of the micropatterns. The controlled deformation induced by micropatterning, which can lead to defined polarity in natural cells, is applied in this work to bottom-up synthetic cell models based on giant unilamellar vesicles (GUVs) to create a simple induced-polarity system. GUVs were adhered to micropatterned surfaces using biotin and streptavidin as linking systems, as well as complementary DNA oligomers, leading to a controlled deformation of the vesicles on differently shaped micropatterns. While GUVs have been deformed before using tools like microfluidic chips, micropatterns allow for the controlled deformation of large amounts of vesicles in a similar manner to natural cells. The deformation of adherent GUVs is quantified on stripes of 15 µm in length and 5 µm in width. Here, it is observed that GUVs deform most when the GUV size is comparable to the size of the underlying micropatterns. The effects of the GUV deformation on encapsulated actin bundled with fascin is investigated, as the organization of parallel stress fibers is a hallmark in mesenchymal cell migration. In adherent GUVs, I could show for line shaped micropatterns that actin bundles orientate along the major axis due to confinement. Additionally, I demonstrate using a simple theoretical model, that actin bundles, modeled as rigid rods, are most affected inside of GUVs adhered to line-shaped micropatterns, compared to other patterns commonly used to deform cells, such as cross or crossbows. In the next step, I polymerized actin in the presence of dextran as a crowding agent inside of the GUVs, which leads to the generation of cortex-like structures. These synthetic actin cortices organize due to the high membrane curvature at the adhesion site, where the GUV membrane transitions from the adherent to the free part, leading to spiraling actin patterns in the GUVs. Synthetic actin cortices further inhibit GUV deformation, when adhered to micropatterned surfaces. I show, that the deformability is only reduced when both components, actin and crowders are present in the GUVs. This indicates that the cortex-structure leads to the decreased deformability of the GUVs. These results are confirmed using real-time deformability cytometry (RTDC), which provides data for large populations of GUVs. Last, I try to use phase separated GUVs as a model system for polarity. Lipid phase separation creates domains with distinct physical and chemical properties of the membrane, which allows for the selective functionalization of a single phase. Using adhesive micropatterns, the biotin-rich phase accumulates at the micropatterned surface, as was reported before. Additionally, the geometric change in the adherent GUV leads to a cap-formation, where a domain of the minority phase is stably localized on top of the deformed GUV. I use Monte Carlo simulations to demonstrate that the cap-formation can be explained by line-tension. To conclude, I show that micropatterns provide a tool in bottom-up synthetic biology to controllably adhere and deform GUVs. Further, I show that the geometrical cues lead to changes in actin organization inside of the GUV and that synthetic actin cortices can hinder the GUV deformation. Ultimately, I establish that the arrangement of domains within phase-separated GUVs can be attained through adhesion and deformation of GUVs on micropatterned surfaces. For prospective applications, this organization could serve as a scaffold, leveraging the controlled localization of domains to organize proteins inside synthetic cells leading to polarity formation. Additionally, it may facilitate interfacing synthetic and natural cells, as synthetic actin cortices can provide mechanical cues, which, when combined with the spatially controlled presentation of ligands at the surface, open new ways to modulate and create signaling in such combined systems.

Zusammenfassung

Polarität und räumliche Organisation von Molekülen sind Hauptmerkmale, die auf Skalen von einzelnen Zellen bis zum gesamten Organismen zu finden sind. Diese Eigenschaften bestimmen das Verhalten von Zellen bei asymmetrischer Zellteilung sowie die Richtung in die Zellen sich bewegen. Polarität in Zellen kann als eine asymmetrische Verteilung von Molekülen definiert werden, welche zu leicht beobachtbaren Eigenschaften wie einer asymmetrischen Zellform oder Verteilung von Aktinfasern führt. Wenn Zellen deformiert werden, indem sie an Mikropattern adhäriert werden, kann dies die Richtung der Polarisation bestimmen. Mikropattern sind mikrostrukturen auf passivierten glasoberflächen, auf die adhäsionsmoleküle aufgebracht werden. Die kontrollierte Verformung, die durch Mikropattern induziert wird, wird in dieser Arbeit auf synthetische Zellmodelle angewendet. Als synthetische Zellmodelle dienen gigantische unilamellare Vesikel (GUVs). Mithilfe der Wechselwirkung von Biotin in der GUV Membran und Streptavidin auf den mikrostrukturierten Oberflächen werden die GUVs auf diesen adhäriert. Dies führt zu einer kontrollierten Deformation der Vesikel in Abhängigkeit der Form der Mikrostrukturen. Während die Deformation von GUVs, beispielsweise in Kanälen in Mikrofluidik-Chips, bereits bekannt ist, ermöglicht die Nutzung von mikrostrukturierten Oberflächen eine kontrollierte Deformation großer Mengen von Vesikeln auf die gleiche Weise, wie sie für natürliche Zellen verwendet wird. Die Deformation der anhaftenden GUVs wurde auf Linien mit einer Länge von 15 µm quantifiziert. Dabei wurde beobachtet, dass GUVs am stärksten deformiert werden, wenn die GUV Größe mit der Länge der Mikrostrukturen an denen sie haften vergleichbar ist. Die Auswirkungen der GUV Deformation auf die Organisation von in GUVs eingebrachte Aktinfasern, die mit Fascin gebündelt sind, wurde untersucht. In natürlichen Zellen ist eine bestimmte Organisation des Aktins beispielsweise für die mesenchymalen Zellmigration wichtig. Bei deformierten GUVs konnte ich für linienförmige Mikrostrukturen zeigen, dass sich das Aktin aufgrund der Begrenzung durch die Membran entlang der langen Seite orientiert. Darüber hinaus wurde mit einem einfachen theoretischen Modell gezeigt, dass Aktinbündel auf linienförmigen Mikrostrukturen stärker beeinflusst werden als auf anderen Mikropattern wie Kreuzen und Armbrüsten. Im nächsten Schritt polymerisiere ich Aktin zusammen mit Dextran als Crowding-Agent innerhalb der GUVs, was zur Entstehung von synthetischen Aktin-Cortices führt. Im Grenzbereich der Adhäsionsstellen, wo die Membran vom anhaftenden zum freien Zustand übergeht, weisen diese synthetischen Aktin-Cortices eine spiralförmige Organisation von Aktinbündeln auf. Das ist auf die starke Krümmung der GUV-Membran in diesem Bereich zurückzuführen. Die synthetischen Aktin-Cortices mindern die Deformation der GUVs, wenn sie an mikrostrukturierten Oberflächen haften. Es wird gezeigt, dass die Deformation nur gemindert wird, wenn sowohl Aktin als auch Crowder in den GUVs vorhanden sind, was darauf hinweist, dass die Cortex-artige Struktur benötigt wird, um die Verformbarkeit der GUVs zu verringern. Diese Ergebnisse wurden mit Real-Time Deformability Cytometry (RTDC) Messungen bestätigt, welche Daten für große Mengen von GUVs liefern. Zuletzt verwende ich phasenseparierte GUVs als Modell für Zellpolarität. Die Phasentrennung der Lipide führt zu Bereichen mit unterschiedlichen physikalischen und chemischen Eigenschaften in der GUV Membran, was die selektive Funktionalisierung einer einzelnen Phase ermöglicht. Durch die Verwendung von adhäsiven Mikrostrukturen sammelt sich die biotinreiche Phase an der mikrostrukturierten Oberfläche an. Zusätzlich führt die Deformation zur Bildung einer Kappe auf dem oberen Teil des GUVs, die aus der Phase besteht, welche zu einem geringeren Anteil in der Membran vorhanden ist. Ich verwende Monte Carlo Simulationen um zu zeigen, dass die Bildung dieser Kappe allein durch Line-tension an der Phasengrenze erklärt werden kann. Ich zeige, dass Mikrostrukturen ein Werkzeug in der bottom-up synthetischen Biologie sind, um GUVs kontrolliert an Oberflächen anzuhaften und zu deformieren. Darüber hinaus wurde gezeigt, dass die Deformation der Membran zu Veränderungen in der Aktinorganisation innerhalb der GUVs sowie zur Organisation in phasenseparierten GUVs führen kann. In Zukunft könnte diese Organisation genutzt werden, um Proteine innerhalb synthetischer Zellen zu organisieren und so zu Polarität in synthetischen Zellen zu führen. Zusätzlich könnten synthetischen Aktin-Cortices in GUVs die Verbindung von synthetischen und natürlichen Zellen erleichtern, da diese die mechanischen Eigenschaften natürlicher Zellen nachahmen, und, kombiniert mit der kontrollierten Präsentation von Liganden an der Oberfläche neue Möglichkeiten eröffnen, solche Systeme aus lebenden und synthetischen Zellen zu bauen und modulieren.

Your heart is a muscle the size of your fist, keep on loving, keep on fighting
- Ramshackle Glory

Acknowledgements

I would like to acknowledge all the wonderful people, that helped me throughout this journey with their valuable input and support. Without you this work would not have been possible.

I want to thank Prof. Dr. Joachim Spatz for his unwavering support and for providing me with the freedom to cultivate my ideas. I am profoundly grateful for the nurturing environment he fostered, one that embraced the exploration of concepts and the encouragement to experiment. His mentorship and trust have not only enriched my academic pursuits but have also nurtured my personal and professional development.

Further, I owe my deepest gratitude to my direct supervisor, Prof. Dr. Dr. Ada Cavalcanti-Adam for her constant support, for her trust, optimism and guidance throughout this work. I want to thank her for igniting my passion for cellular biology and for entrusting me, as a former theoretician, with the opportunity to contribute to laboratory research. Her belief in my abilities and willingness to integrate theoretical perspectives into experimental work have been invaluable in broadening my understanding of cells natural, and synthetic.

I want to thank Prof. Dr. Kerstin Göpfrich, for her support whenever I felt lost in the vast synthetic biology space. For reminding me to keep things simple, which is the beauty of bottom up synthetic biology.

I would like to thank Prof. Dr. Peer Fischer, who showed interest in this project and agreed to participate and discuss this work in my defense.

I want to thank Dr. Alba Diz Muñoz, for her guidance throughout this project. I am deeply grateful for her kind reminder to ”Focus!” on one project at a time, rather than juggling multiple tasks simultaneously.

I would like to thank Dr. Dimitris Missirlis for for engaging in insightful discussions and posing challenging questions, always accompanied by a warm smile. You have inspired a level of reflection and insight that I wouldn’t have achieved otherwise. Also, thanks to you, the title was one of the first things this thesis got, because ”you cannot write a thesis without having a title!”

To Dr. Ilia Platzman, I am sincerely grateful for the helpful discussions along the way and for keeping an eye open for potential applications in basic research.

I want to thank Dr. Nadanai Laohakunakorn for his incredible help with using the PURE system, and for amazing discussions during a conference.

My partner, Ana, I owe you my gratitude for your constant support throughout this time and for your optimism. I want to thank you for believing in me, especially when I was dramatic. Your trust, empathy, and understanding has created a safe space where I could freely express myself and seek guidance. I also want to thank you for showing me the field of synthetic biology, as well as discussing and developing ideas.

I would also like to acknowledge the friends I've made along the way. Yannik! - There is no way to thank you without a cup of coffee in the hand and some sketch-figures on the desk. Our gradient descent might have increased in energy, but that doesn't mean, the code is wrong, right? Thank you so much for your support in the office and while bouldering. Tobias Abele, Thank you for doing the RTDC experiments with me. Tobias Walther, I want to thank you for fun afternoons with mario kart and for many promising and failed experiments with RNA. Erik, for answering my theory questions and geeking about GUV-GPT, as well as showing me the most obscure music I never knew existed. Michelle Kemper, just because you can change the number π in numpy to 3, doesn't mean, you should! Thank you for brightening office-life with some awesome music! Ann-Kathrin, I want to thank you for your friendship, for the experiments we did together, and many coffee breaks that sparked ideas and discussions. I would like to thank William for the help with electroformation of GUVs. Julia, the attack-part of the B-Team during the kicker tournament, thank you for making the time during my PhD more enjoyable than it would have been without you. Meline, I want to thank you for sharing your knowledge of cells, but also for being a friend outside of the lab.

I would like to extend my appreciation to Martin Lukat and everyone from the mechanical workshop, I want to thank you for building the small devices, that made my day to day work in the lab much easier.

I want to thank the students, who did their internships and theses under my supervision, Charlotte, Sunnatullo, Thien, Lera, and Tanja. I want to thank you for the trust, the ideas and discussions we had together. I have to thank you for bringing new perspectives into the project.

I want to thank my family, Sylvia, Peter and Emilia Fink, whose unwavering support, encouragement, and love have been the cornerstone throughout my academic journey. Without you i would not be where I am now. Their endless encouragement during both the triumphs and challenges during all of my studies have been invaluable.

I want to thank Piet Becker for your friendship since our school days. Our ability to confide in each other, discuss ideas, and navigate the complexities of life has enriched not only my academic pursuits but also my personal growth.

Further, I want to extend my gratitude to Matthias, Tamara, David, Lotte, and Felix.

From late-night study sessions to sharing moments of joy and laughter, their presence has made every challenge more bearable and every success more meaningful. For proof reading, I would like to acknowledge, in random order, Ana, Julia, Meline, Ann-Kathrin, Anastassiya, Erik and Michelle.

Finally, I would like to thank the whole research group for many helpful and fun discussions over many cups of coffee, you have bettered my days and given me a lot of ideas and inspiration.

Thank you.

Contents

List of Figures

List of Tables

1 Introduction

NASA defines life as *a self-sustaining chemical system capable of Darwinian evolution*[1]. This provides a general framework, guiding not only the discovery of alien lifeforms in the outskirts of the observable universe. It can also serve as a guideline for bottom-up synthetic biologists working on creating alien, or synthetic cells on earth, who are inevitably confronted with the question of what life is[1,2]. Although the question may seem simple at first glance, it is not yet fully answered and thus focus is laid on defining single characteristics living beings have in common[3,4]. One key aspect mentioned by Erwin Schrödinger in the book *What is life?*, is that organisms maintain a high degree of orderliness throughout their lifespan. While this would seemingly defy the second law of thermodynamics if organisms were closed systems, they expend energy to maintain such an organized state and by that decrease the orderliness of their environment[4]. Thus, living systems are far from equilibrium, energy dissipating systems, which are hypothesized to potentially emerge in the presence of pronounced energy gradients, as observed on earth at hydrothermal vents, or the surface of oceans due to intense sun radiation, with the thermodynamic aim to dissipate energy more rapidly[5]. Increasing energy dissipation has been argued to be a possible driving force in the emergence of life, as well as continuation of evolution[6].

1.1 Molecular organization and motility in cells

Cells, called the basic units of life, can be described as complex, biochemical reactors, which in return are molecular assemblies that are able to divide and move[7,8]. In order to perform these, seemingly simple, tasks, the molecules necessary for the task at hand have to organize and assemble at the correct spots, in the correct order, thus highlighting the importance of molecular organization in natural cells[8]. In this work I will focus on the intricate processes of cell migration and polarity, stemming from the molecular organization inherent in natural cells. I will then introduce ways, these functions are tried to be simplified and reproduced, and will explain the overarching goals of this thesis, on approaches to engineer polarity into synthetic cells.

1.1.1 Cell motility

One of the most recognizable features of living organisms is the ability to actively change their location[9]. Motility is a fundamental function that is found in single- as well as multicellular organisms. One remarkable example of single cell migration are slime molds, such as the up to 10 square meter large *Physarum polycephalum*, which moves due to pulsing movements of the membrane to explore the environment and find new food sources[10]. But also microscopic single celled organisms can display motility, such as *Euglena gracilis* that swims using a beating flagellum, a thin, periodically beating hairlike tail. *Euglena gracilis* harnesses the motility to move in dependence of outer cues such as light, in a manner called phototaxis[11]. Motility is found in many single celled organisms, such as bacteria or amoeba, as it enables them to more towards better conditions or colonize and spread[12]. But also in large, multicellular organisms, single cells move to execute their respective functions, such as wound healing and angiogenesis[13]. In wound healing, epithelial cells move in a collective, coordinated manner. Here, a follower-leader dynamic is established, where single cells facilitating the movement of subsequent cells to follow behind. Such a dynamic is not only found in healthy tissue, but also in disease, such as cancer, where single cells and collectives can migrate out of the tumor and spread throughout the organism[14,15]. Arguments have been brought forward, that motility might have emerged at the origin of life, or even in an prebiotic environment, and might thus be closely intertwined[16]. Motility has played an important role throughout evolution, as it helps cells to react to to unfavorable environmental conditions and thus increasing the adaptability, colonize new environments and plays important roles for the functioning of multicellular organisms[17].

1.1.2 Minimal cell migration

A well established minimal model system for mesenchymal cell migration are fragments of the lamellipodium of keratocyte cells, shown in Figure 1.1. The actin (cyan) in the polarized fragment (Figure 1.1**a**), is polymerized into a dense network at the leading edge of the lamellipodium (top of the image). The rear shows a high concentration of myosin II (red), hinting towards strong contractility in this region. Such motile fragments fragments indicate, that directed cell motility can be achieved by actin polymerization in the front and actomyosin contractility in the rear, without the need of a nucleus or additional cytoskeletal proteins like microtubuli[18]. Stationary, non-polarized fragments show a

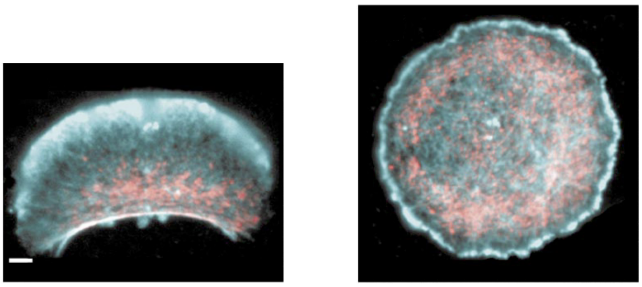

(**a**) Polarized, motile lamellipodia fragment

(**b**) Unpolarized lamellipodia fragment

Figure 1.1: A polarized **a**, and a non-polarized **b** keratocyde fragment of the lamellipodium is shown. Actin is stained in cyan, myosin II in red. The polarized fragment shows a strong localization of myosin II in the rear of the fragment. The non-polarized fragment appears circular, with actin and myosin spread evenly throughout the fragment. Scale bar is 2 µm. The Figure was adapted from Alexander B. Verkhovsk et al.[18]

circular morphology, and a homogenous distribution of actin and myosin (Figure 1.1**b**). Furthermore these can become motile upon deformation induced from the outside (Figure 1.1**a**), and can change back to a circular, stationary state, pointing out the importance of geometry and molecular distribution on cell functions, such as motility[18,19]. This further emphasizes the interplay of geometry and molecular organization, as well as the direct effect of changes in geometry that can induce polarity. Further, the importance of the actin cytoskeleton for locomotion, and with this actin organization is reflected in these minimal model systems. Actin, together with various proteins that bind and modulate the actin behavior is able to generate a vast array of structures with different functions, such as branched actin networks that polymerize at the plasma membrane at the leading edge of motile cells, which builds up the lamellipodium. Observing motility in such a minimal system indicates, that potentially only a hand full of the correct components are needed to create systems that can reproduce the means of migration found in lamellipodium fragments. The reversible change from unpolarized to polarized upon external stimuli further hints, that the correct organization might be induce from external cues, if a system includes the correct components. Actin thus plays a vital role in the force-generation and motility of cells, and can also be used to identify polarity in natural cells. Some of the various actin structures are introduced in the following sections.

1.1.3 Cell polarity

Polarity is a hallmark feature in living cells that enables many cellular functions, like directed migration or asymmetric cell division[20,21]. Cell polarity is often defined over cell shape and an asymmetric molecular distribution[20]. In natural cells both are closely coupled, as cells actively control their shape. An asymmetric distribution of molecules, such as actin and myosin leads to a change in cell shape, as seen well when polarized and non-polarized lamellipodia fragments are compared (Figure 1.1). Migrating mesenchymal cells have a distinct shape (Figure 1.2**a**) and show a polarization between front and rear. Other cells, that typically exhibit polarity are neurons with an axis of polarity along the axon (Figure 1.2**b**)[21]. One hallmark of the axon of a neural cell is the axon initial segment, which is localized where the axon emerges from the cell[22]. Another marker of polarity in neural cells is Wnt activity, that gradually increases along the axon with increasing distance to the cell body[23]. Epithelial cells show a polarity between the apical and basal site, allowing for a distinct functionality at each end (Figure 1.2**c**). Further, cell polarity can be induced in a controlled manner by deforming cells on micropatterned surfaces. In these cases where a shape is imposed in the cell, polarity can be observed in the molecular and organelle distribution inside of the cells. This heterogeneous distribution and organization of proteins inside of the cell is what is generally referred to as cell polarity, and will be used a marker to identify and define polarity through-out this work. In natural cells, polarity is actively established and maintained via various mechanisms and can stretch from single cells to several cells up to whole organs, prominently found in embryonic development[20]. Mechanisms for establishing cell polarity include the activation of bacterial min proteins, rho family proteins, that, in migrating eukaryotic cells, activate Wiskott-Aldrich syndrome protein (WASP) which in return enables actin polymerization by activating actin related protein 2/3 (arp2/3) at the cell front. At the cell back, actomyosin contraction leads to retraction of the rear. The resulting polarity of the actin cytoskeleton in mesenchymal migrating cells, where the front is protruding and the back contractile, which pushes the cell forward is commonly observed. Cells actively maintain this organization of molecules, which are, for example in the case of Min and Rho proteins reaction diffusion systems[24,25]. The minCDE system has been shown to create different protein patterns, depending on the cell geometry, when reconstituted in *in vitro* systems such as microwells and GUVs[26]. This indicates some potential mechanisms of geometry censing in cells, as well as an adaptive way to organize molecules depending on the cell shape.

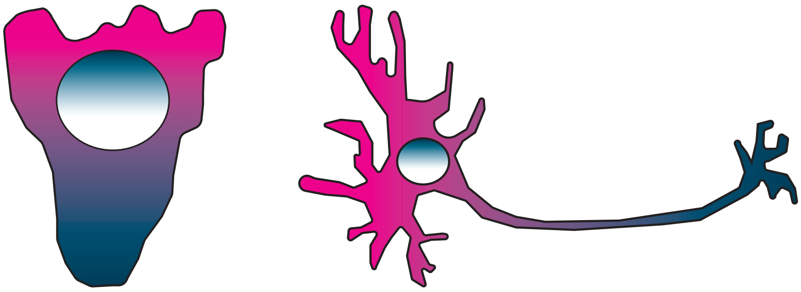

(a) Polarized migrating cell

(b) Neuron

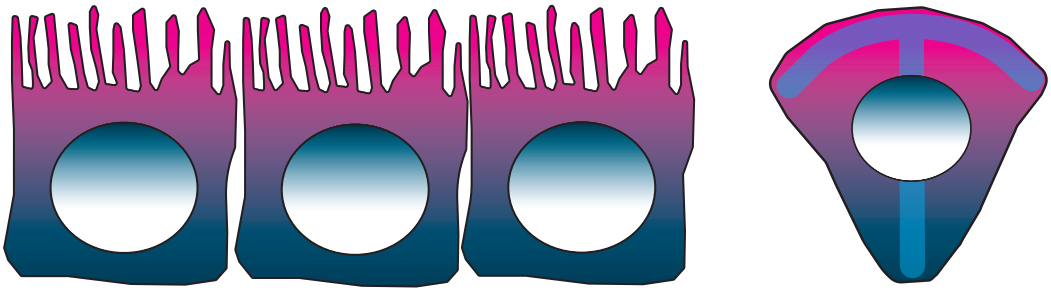

(c) Apical and basal polarity in epithelial cells

(d) Polarized cell on crossbow micropattern

Figure 1.2: Sketch of naturally occurring polar cells. Polarity is indicated by the magenta-blue gradient. **(a)** Migrating cells show front-back polarity, and a triangular shape. **(b)** Neurons are polarized along the axis of the axon. **(c)** Apical and basal polarity is found in monolayers of epithelial cells. d) Polarity can be induced when cells are adhered to crossbow micropattern.

1.1.4 Micropatterning to control cellular behavior

Micropatterns are a tool used to control cell shape and behavior and improve comparability of various cells[27]. Micropatterns enable the controlled presentation of various molecules and ligands in well defined shapes. It thus also allows to decouple chemical from geometrical effects by using various micropatterned shapes. Micropatterns have been used to study cell polarity and polarity induced effects, such as the axis of cell division and stem cell differentiation in dependence of geometrical and chemical cues. They are also used to study coordination of cell collectives under confinement[28]. Several methods exist to create micropatterns, such as microcontact printing, laser-patterning and photolithography. The methods to generate micropatterns are generally based on creating areas that are functionalized with a protein, that are surrounded by areas passivated with polyethylene glycol (PEG). In micro contact printing, a PDMS stamp with the pattern is pushed directly onto the glass substrate to print extracellular matrix (ECM) proteins directly onto the glass. The substrate is passivated with PEG afterwards, so only the patterned region is adhesive to cells. Deep UV LASER light can be used directly to pattern on passivated surfaces by destroying the PEG layer locally and thus allow for the binding of ECM proteins in the illuminated areas. Maskless photolithography also starts from a PEG passivated glass surface. The light sensitivity of the PEG layer is increased by the addition of molecules that release free radicals upon UV irradiation. With this, the PEG is destroyed locally, similar to the direct laser patterning but with lower laser powers, and can now be filled with the desired protein where the PEG layer is destroyed[28,29]. In this work, I used maskless photolithography to generate the micropatterns, as it allowed for a fast and simple production of the desired pattern. Further, the pattern can be changed without much effort and planning, as only the digital image serving as template has to be remade[29].

1.1.5 Connecting cell shape and function

The controlled presentation of ligands in certain shapes can determine cell shape and function. In living cells, function and shape are often directly coupled and intertwined. The physiological role of cells can determine their morphology, as it can be crucial for various functions to assume a certain shape[30]. Generally, cell-types in many organisms can be categorized by the cell shape.

Neurons, for example relay signals over long distances and build convoluted networks, that make up the central nervous system. A schematic shape of a neuron is shown in Figure 1.2**b**, where the long axon can be seen, that allows for the communication over large distances. The shape of dendrites can further contribute to the computational functionalities[31].

Erythrocytes (red blood cells) transport oxygen from the lungs throughout the body. While flowing through blood vessels for up to 120 days, they withstand considerable stresses, such as shear stresses, due to their high mechanical stability[32,33]. At the same time they have to be able to pass small capillaries to reach all parts of the body. Many capillaries are smaller than the 7.5-8 µm diameter of the red blood cell, meaning they have to be highly deformable. The shape of erythrocytes is generally described as a biconcave disk, which is the energetic optimum if the membrane bending energy is minimized for a deflated cell[33,34]. The shape of these cells allows them to flow optimally through blood vessels, and thus lead to an optimal supply of oxygen throughout the body[35].

Epithelial cells, and their packing regulates the shape of large structures such as organs, which in return is crucial for the organs function. Epithelial cells can form sheets that act as a barrier. To this end the cells have to be densely packed together to allow the barrier to work efficiently. Epithelial cells generally have an apical and basal polarity, which can be functional as well as structural, and are bound to their neighbors by tight junctions. One example of functional epithelial sheets is found in the kidney, where they generate a sodium gradient, that can be used to move other ions[36]. Disruptions or dysfunction of epithelial barriers can lead to diseases, such as atopic dermatitis when the skin barrier is chronically damaged[37].

In short, cell structure is important to provide the various functions cells have in organisms. Variability in cell shape is also found in single-cell organisms, where it can aid in motility or feeding[38]. Many factors play into cell shape, such as forces induced by the cytoskeleton, surface to volume ratio and external cues, such as confinements or adhesive structures[38]. Natural cells can thus, in part, change their shape to adapt to their environment and function while their shape is still governed by physical principles[39].

1.1.6 Actin Cytoskeleton

We have established before, that actin plays a crucial role in mesenchymal cell migration. Actin is a globular protein, with a molecular weight of 43 kD that is able to reversibly polymerize into fibers with a diameter of 7 nm in an adenosine 5'triphosphate (ATP) dependent manner[40,41]. Filaments have a fast growing plus and a slower growing minus end. ATP-actin associates stronger with other actin monomers in filaments than hydrolyzed ADP-actin. Thus, ATP-actin is incorporated into the filament at the plus end, hydrolyzes over time to adenosine 5'diphosphate (ADP) bound actin in the filament, which leads to an unstable ADP-actin cap at the slower growing and easier dissociating minus end. This then leads to the slow dissociation of the old filament-part at the minus end, while it keeps growing from the plus end. At certain conditions his results in a steady state, where the plus end keeps growing while the minus-end is disassembling, leading to the so-called tread-milling of filaments. Under these conditions, the actin filaments seem to move towards the plus end. The polymerization and depolymerization is further affected by various adaptor proteins, such as Arp2/3 and Formins, which nucleate and polymerize filaments. Further myosin motor activity can break up actin filaments through mechanical force, leading to faster depolymerization. The importance of actin dynamics in living cells becomes even more evident, cells are killed by addition of phalloidin, which binds to actin filaments and prevents their disassembly[42].

Actin is often found associated with various proteins that heavily modulate its behavior, dynamics and function, such as the afromentioned actin nucleators and elongators, but also bundling proteins, such as fascin and $\alpha-$ actinin and capping protein, that can inhibit actin assembly by blocking the addition of new subunits[43].

Three important actin based structures that are found in natural cells are actin stress fibers, which are long bundles of actin filaments that span throughout the cell, the lamellipodia and filopodia at the leading edge of the cell, that are strongly involved into cell migration and the actin cortex, a thin layer of branched actin network that is located directly beneath the cell membrane. While all these structures are based on actin filaments, their shape and functionality is mainly determined by additional proteins. Actin stress fibers are long structures of bundled actin, that can span the whole cell[44,45].These are typically bundled by proteins, such as myosin II and α-actinin and connect focal adhesion points throughout the cell. Stress fibers range from dynamic, contractile structures in migrating cells, to quasi-static ones[46]. Lamellipodia, found at the leading edge of migrating cells are protrusive structures, utilizing the force generated by actin polymerization, which pushes against the cell membrane. Actin nucleators and elongators, as well as their inhibitors modulate the actin polymerization in these structures to generate a highly polarized and dynamic structure. The directionality of cell-migration can mainly be attributed to the directionality and stability of these lamellipodia structures, which is consistent with the motility observed for fragments of the lamellipodium of keratocytes[47]. Typical for these structures is the establishment of a stable retrograde flow, where actin monomers diffuse to the leading edge, get incorporated into actin filaments at the cell membrane, which get pushed by myosin activity into the lumen of the cell, where they depolymerize again[48]. Another structure relevant for the here presented work is the actin cortex, a dense actin network with a thickness of around 250 nm, that is bound to the cellmembrane[49]. It has been shown, that changes in the distance of the actincortex to the plasma membrane can modulate the mechanical properties of the cell. The actin cortex further is the foundation of the viscoelastic properties of cells, which behave elastic at short timescales, but viscous at longer ones due to the remodeling of the cortex[50].

1.2 Synthetic biology

Synthetic biology is considered to consist two broad fields. One employs biological molecules and systems to induce alterations which prompt them to exhibit novel functionalities. One of the simplest examples is the transfection of a cell to produce a protein it naturally would not make. The other field tries to assemble synthetic, purified molecules *in vitro* to recreate parts and functions of living systems, with the aim of creating an artificial cell. Constructing artificial cells from the bottom up is an incredibly interdisciplinary challenge, combining the fields of physics, engineering, chemistry and biology[51].

1.2.1 Top-down synthetic biology

Building a synthetic cell is tackled in two complementary ways, a bottom-up and a top-down approach. In the top-down approach, one starts with a living cell where every component, that is not deemed essential is removed, leaving one, in principle, with a set of indispensable components that are required to maintain life. The probably most notable example for this approach is the minimal cell *JCVI-syn3.0*. To generate this minimal cell, the bacterium *Mycoplasma genitalium*, that incorporates only 525 genes in the wild-type and thus the smallest known genome of a natural cell was chosen as a starting point. The total gene count was reduced from the 525 genes in the wild-type to 473 genes to give birth to the first version of the minimal cell *JCVI-syn3.0*[52]. This approach allows for the identification of functions and components that are vital to life and survival and thus allowing to focus and the most important components. Such a minimal, functional cell can help understand the function of single genes, as, in comparison to organisms that encode a larger number of proteins, it cannot circumvent mutated or silenced genes by relying on alternative pathways. But *JCVI-syn3.0* also reflects the complexity inherent to all known life-forms. At the time of publication of the minimal genome, 149 of the 473 considered essential genes are not, or only partially understood[53]. This still demonstrates our lack of understanding of what components are essential to make up a living, minimal cell.

1.2.2 Bottom-up synthetic biology

In the bottom-up approach on the other hand, the goal is to assemble a living cell starting from well defined, synthetic or purified components. The goal of building an artificial cell quickly gives rise to the question of what life is and what properties it needs to possess to be life-like. For this, NASAs definition of life as *a self-sustaining chemical system capable of Darwinian evolution* allows to imagine a broad array of systems, that can potentially be considered life-like while, while simultaneously bearing no resemblance to known terrestrial life[1]. This opens up fundamental questions, such as under which conditions life can exist and what components are needed to achieve these properties. These questions are also of great importance to the exploration of life outside of earth. Looking at extremophiles, organisms that can live and thrive in extreme environments, it quickly becomes clear, that many, on first glance hostile environments are home to specialized organisms[54]. It furthermore allows us rethink what is considered extreme. One example is an environment that is characterized by the presence of oxygen. Oxidative stress is a serious issue for living cells and life on earth is believed to have started under anaerobic conditions. The day-to day environment we live in could thus be considered extreme and hostile[54,55]. Bottom-up biology is a promising approach to build and develop life-like systems, that are potentially set up very differently than life as it is commonly found on earth and gives us thus the tools to create life deemed alien here on earth. Bottom-up synthetic biology further forces us to think in novel ways about problems, where classical engineering-based approaches, where a certain outcome is expected based on a well defined input, are failing. While small perturbations to living systems, like common techniques to express unnatural proteins inside of cells are readily performed, we have yet to put together a fully synthetic organism, pointing out the need of new technologies and approaches[44,56,57].

Synthetic biology allows the change from a mainly descriptive point often found in biology point to actively design and create molecular systems[58]. In contemporary synthetic biology, numerous naturally occurring biomolecules, such as DNA or proteins, are utilized. However, their inherent functionality is not always retained, but sometimes expanded upon in ways not found in nature[58]. DNA origami is a great example, where a biomolecule was harnessed to, in this case build structural elements, as well as forms of catalysts called DNAzymes[59,60]. De-novo design of proteins, where, thanks to novel computational methods, such as AlphaFold, structures can be predicted based on their amino-acid sequence, are utilized to expand the shape and functionality of proteins[61].

1.2.3 Giant unilamellar vesicles as cell models

Giant unilamellar vesicles (GUVs) are commonly used as cell model systems. They are closed compartments similar to natural cells in size, with the inside separated from the outside bulk by a lipid bilayer[62]. In Figure 1.3**a**, a schematic view of a GUV is shown next to a confocal image of GUVs with a fluorescently labeled membrane (Figure 1.3**b**, magenta). GUVs are usually composed of a low number of different phospholipids, resulting in a much lower complexity than the lipid mixtures found in natural cell membranes. While cell membrane derived vesicles, called giant plasmamembrane vesicles (GPMVs) exist, they lack the controllability of such a fully synthetic system[63]. In this work, we will therefore focus on GUVs comprised of synthetic lipids to reduce the influence of variables outside our experimental control. The usage of synthetic lipids also allows for the controlled incorporation of single lipids of interest into the GUV membrane, if it is required for protein function. It thus enables the study of the specific effects that single components have on the system in a well controlled manner. This gives rise to easy to interpret results, when the function of a single component is investigated, in comparison to natural cells, where the change of a single component might have an effect on various parts[64,65]. On the other hand, it can be difficult to introduce complex functional modules into GUVs. Although several methods exist to create giant vesicles, the precise goal usually dictates the method best suited for the challenge at hand. While swelling-based methods, like gentle hydration or electroformation allow for a precise control of the lipid composition of the GUVs, they are inefficient at encapsulating macromolecules, like proteins[66]. These methods provide valuable tools, when the membrane-composition plays an important role in the experimental setup, such as for phase-separated vesicles. Emulsion-based methods, such as emulsion transfer and cDICE allow for the efficient encapsulation of various cargo on the inside, but lack control of the precise lipid composition in the membrane. These methods can be used to encapsulate actin networks with various binding proteins, pattern generating reaction-diffusion systems like the Min system and protein expression systems like PURE, consisting of the transcription-translation machinery[67–70]. Although reports have shown the successful production of phase separated vesicles using cDICE and emulsion transfer protocols, a precise control over the lipid composition remains a challenge with these methods[71,72]. Microfluidic approaches were developed, that allow the sequential construction of vesicles inside of surfactant stabilized droplets in oil, called droplet stabilized GUVs (dsGUVs). Such microfluidic systems allow for the creation of monodisperse vesicles, as well as the loading of various cargo, such as actin and tubulin inside of the GUVs[73]. This method is once more constrained by the range of lipid mixtures that can be feasibly utilized for the GUV production[74]. Recently, a bulk-method based on the microfluidic approach was presented, also yielding droplet stabilized vesicles that enable the encapsulation of various cargo without the need for complex microfluidic setups[75]. DsGUVs also allow for the functionalization of the membrane with transmembrane proteins that are readily incorporated into small unilamellar vesicles, but remain a challenge to reconstitute into GUVs[73].

As it can be seen, various methods for the production of GUVs are used, each with their respective strengths and shortcomings. The choice of method is thus very dependent on the exact application. In this work, I mainly use the emulsion transfer method, as it allows for the efficient incorporation of cytoskeletal proteins. I further use electroformation when

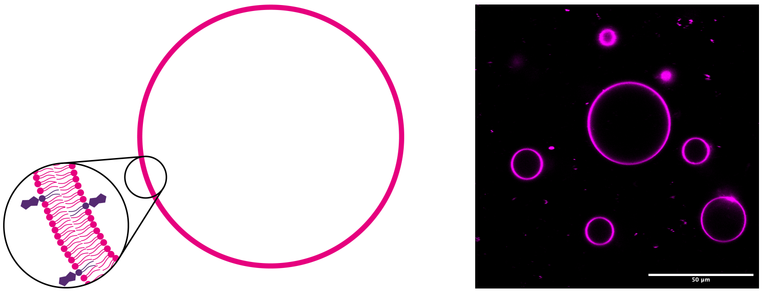

(a) Schematic view of a GUV

(b) Confocal image of GUVs

Figure 1.3: Schematic view of a GUV as a cell modelsystem, providing a lipid bilayer membrane, that separates the inside from the outside of the confinement. In **b**, a confocal image of GUVs can be seen. Scale bar is 50 µm

GUVs with a precise membrane composition were needed, to generate phase separated GUVs.

1.2.4 Reconstitution of cytoskeletal elements in GUVs

The cytoskeleton of the cell is a remarkably versatile structure and the main force-generating mechanism in eukaryotic cells[76]. Reconstituting this complex assembly into GUVs is thus very desirable. While the cytoskeleton is comprised of three main building blocks, actin, tubulin and intermediate filaments, the first two received the majority of attention in attempts to recreate parts of the cytoskeletal system in synthetic cells[77,78]. Since actin has been identified as a major component in cell motility, much work has been done towards encapsulating actin into GUVs. There actin generates with various accessory proteins contractile actomyosin rings, allows for the investigation of compartment size and bundling agent dependency on the organization of actin networks, as well as membrane deformation induced by rigid actin-fascin bundles[67,69,79]. Most of these studies are performed in quasi-equilibrium conditions, that include actin and some few actin modulating components. While actin remains the main component in an actin cytoskeleton, the wide variety of structures found in cells, that are based on this molecule is astonishing and can only be explained by the interplay of actin with a huge array of modulator molecules that fine-tune the interaction and functionality to the task at hand. This is further elucidated, when actin is encapsulated in *in-vitro* experiments with only a number of selected components, that allows for the observation of such a variety of structures that are all based on the same protein assembly. In GUVs, membrane-associated actin polymerization has been induced by the activation of Arp2/3 by membrane-bound VCA (verprolin, cofilin, acidic) domain of the wiskott-Aldrich syndrome protein (WASP), that lead to the polymerization of actin cortex-like structures[80].

Many works have shown to incorporate static actin networks into GUVs, which resemble some structures found in natural cells, such as stress fibers and cortex-like structures. Dynamic structures tend to be more complex to encapsulate, but will have to be an essential part on the way to build a synthetic cell[81].

1.2.5 Synthetic cell motility

In eukaryotic cells, actin plays a major role in the motility. Reconstituting a dynamic actin skeleton is therefore of great interest towards the goal of recreating artificial cell motility. Enas Abu Shah and Kinneret Keren showed that actin could be dynamically polymerized at the interface of water in oil droplets, creating a cortex-like structure[82]. To this end, they reconstituted *Xenopus* egg extracts in water-in oil droplets. When they immobilized ActA, and Arp2/3 activator, at the droplet periphery, they observed the emergence of a actin shell, that polymerized at the membrane and depolymerized further in the lumen[82]. They further saw that these cortices could undergo spontaneous symmetry-break, leading to an actin-rich cap and thus a polar actin cortex, as long as myosin functionality was not disturbed. This further points to the importance of both, actin nucleation and elongation activity as well as myosin contractility in the spontaneous emergence of polarity in actin cortices. While using *Xenopus* egg extracts limits the ability to determine key parameters, such as identifying the proteins and their respective concentrations that are essential to generate such a behavior, it still proves, that symmetry break inside such compartments is possible to achieve. Purified actin networks together with myosin were shown to position clusters of these networks asymmetrically in water-in-oil droplets depending on the droplet size[83]. Further, dynamic, polar patterns have been reported for short actin filaments that glide inside of GUVs, driven by myosin motors anchored at the membrane[84]. Reconstituting the full actin machinery, that can lead to cortex formation and force generation from the bottom-up remains challenging, as very good knowledge of the requirements of the single components is needed. This is partially because cells tend to have complex, but robust regulatory networks in place to cope with non-optimal conditions, that are not implemented, when simple regulatory networks consisting of only a couple of components are reconstituted from the bottom-up and require ideal conditions for all parts[56].

1.2.6 Deformation of GUVs

Since cell-shape is an important factor in cell polarity, controlling and changing the shape of GUVs promises to allow for the reconstitution of cellular functions in a more cell-like environment. It has been shown theoretically, that protein patterns can emerge directly from geometric changes[85]. As presented earlier, living cells can polarize controllably when adhered to micropatterned surfaces. Thus, controlling GUV shape is an important part towards the goal of creating synthetic cells. In the past, various strategies have been employed to deform GUVs from the outside, as well as inside, such as trapping and deformation in microfluidic devices, electrical and acoustic fields, as well as optical traps[86,87]. Electric, acoustic and electromagnetic fields tend to be limited to inducing an elliptical shape to GUVs. Microfluidic devices on the other hand allow GUVs to assume different shapes, from simple elongated, ellipsoid shapes in channels, to the trapping and controlled deformation of GUVs to cubic, or star-shapes using pH sensitive hydrogels[87,88]. Protein organization of the bacterial microtubuli homologue FtsZ, which is believed to play a crucial role in the cell division of *E.Coli* has been studied in elongated vesicles in microfluidic traps[86]. There it was observed, that FtsZ shows a a preferential organization along the neck of deformed, elongated vesicles, perpendicular to the major axis.

The encapsulation of cytoskeletal proteins together with various accessory-molecules and proteins can lead to shape changes from inside of GUVs. In the simplest case, long, straight actin bundles, induced by addition of fascin, can yield strong deformations of the GUV membrane with thin protrusions, that are stabilized by the actin bundles[79]. Using an HIV TAT peptide, actin filaments inside GUVs can be organized to deform the membrane in GUVs by interaction with the peptides, that can penetrate the GUV membrane[89].

1.2.7 Phase separation in model membranes

Lipid membranes play a vital role in all known forms of life. They compartmentalize the inside from the outside and provide a semi-permeable barrier. Although cel lmembranes are mainly composed of phospholipids and cholesterol, many amphiphilic molecules have the capability to self-assemble into bilayered membranes under the right conditions[90,91]. Extracts from meteorites, containing amphiphilic molecules have been shown to form vesicles in aquaeous solutions, underlining the possibility of membrane-formation in a prebiotic world[91,92].

In this work, the focus is laid on vesicles comprised mainly of phospholipids, as they are found in the membrane of natural cells. The chemical structure of the main lipids used in this work are shown in Figure 1.4. Phospholipid based GUV are widely used in the bottom-up synthetic cell community, as they readily form lipid memnbranes[93]. Another feature found in many phospholipid based membranes is the tendency to phase separate. The membrane in a vesicle with a homogeneous lipid mixture can spontaneously demix into two or more phases. In vesicles comprised of saturated DPPC, cholesterol and unsaturated DOPC lipids, this demixing happens at room temperature (The chemical structure of the lipids is shown in Figure 1.4)[94]. A schematic view of a phase separated

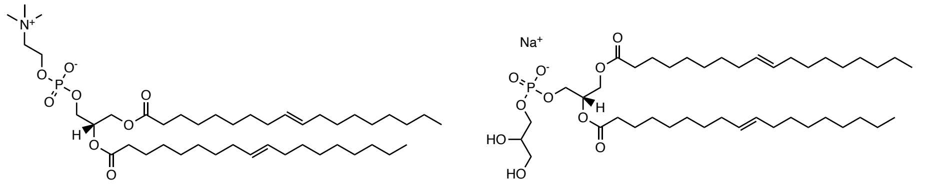

(a) DOPC **(b)** DOPG

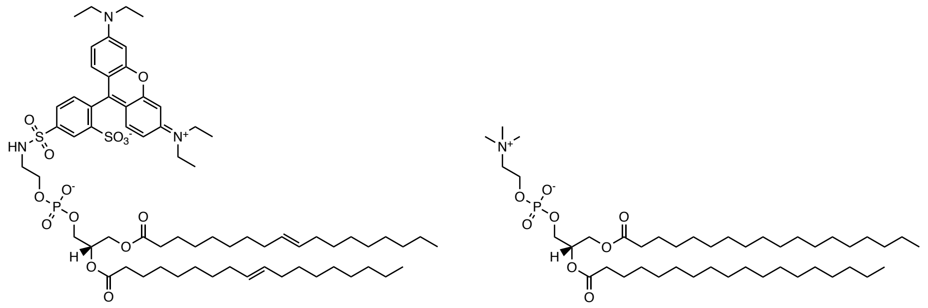

(c) LissRhod PE **(d)** DPPC

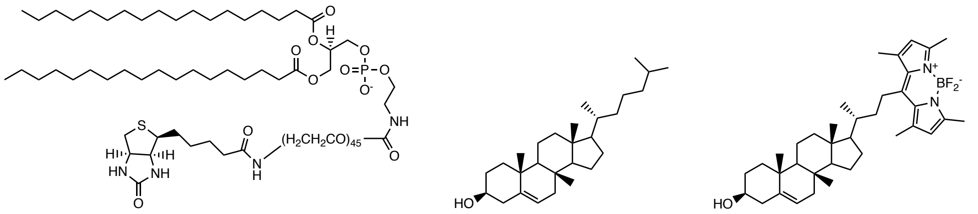

(e) Biotin-PEG2k-DSPE **(f)** Cholesterol **(g)** Top-Fluor cholesterol

Figure 1.4: Chemical structure of the lipids used in this work. DOPC, DOPG, and LissRhod PE have unsaturated hydrocarbon tails, which tend to localize in the Ld phase, while DPPC and Biotin-PEG2k-DSPE have a saturated tail, and are expected to localize to the Lo phase.

membrane containing DPPC, DOPC and cholesterol is shown in Figure 1.5[95]. The two phases have both different physical properties, such as membrane thickness due to their different chemical composition. This leads to the emergence of the line-tension, as the lipids at the phase boundary cannot obtain their optimal conformation, resulting in an energy penalty proportional to the length of the phase boundary.

In uncharged membranes, lipids with saturated tails tend to coexist in the Lo phase together with cholesterol, while unsaturated lipids tend to prefer the Ld phase. From the lipids used in this work, this leads to LissRhod PE to label the Ld phase (See Figure 1.4)[96]. Top-Fluor tagged cholesterol on the other hand can be used to visualize the Lo Phase.

Lipid phase separation is used for organization in synthetic biology, as well as living cells. In natural cells, nano domains and lipid rafts are believed to have important effect on the functionality of many proteins, as well as in signaling. Microvilli in T-cells are believed to exhibit sorting of lipids at their tips due to their high local curvature[97]. This can lead in turn to a differential concentration of various proteins and clustering and thus aid in

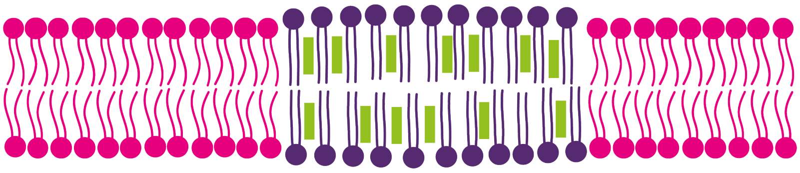

Figure 1.5: Scheme ofa phase separated lipid bilayer membrane. DOPC, in the liquid disordered (Ld) phase is shown in magenta, DPPC in violet, and cholesterol in green phase separate into the liquid ordered (Lo) phase. The thickness mismatch between the two leaflets results in the emergence of the linetension[95].

functions like signaling[98]. Domain formation seems to exist also in bacterial membranes, although their occurrence seems correlated to antimicrobial effects[99]. Further, the distinct properties of each phase allow for the selective functionalization *in-vitro*. In the past, this has been used, to bind proteins, such as GFP to a single domain in a phase separated GUV membrane, and thus functionalize it in an asymmetric way[71]. Phase separation has further been used for the controlled deformation of deflated GUVs. Additionally, GUVs have been split at the domain-boundary, utilizing line tension in phase separated vesicles[96]. The ability to control deformation of deflated GUVs by phase separation leads to the idea, that domain localization could, in return be controlled by externally applied deformation. This principle was shown by K. Nakazawa et al. that in some cases, the minority phase localized at the end section in rod-shaped GUVs under confinement in microfluidic channels[100].

Control over domain organization has also been reported for adherent vesicles. Here, GUVs with a phase separated lipid composition containing biotinylated lipids were adhered to surfaces. Depending onwhether the biotinylated lipids were present in only one, or both phases, they showed that the biotinylated domains could be enriched at the adhesion site[101]. Further, when GUVs were placed on microstructured surfaces, a domain organization resembling the underlying pattern was observed[102].

On supported lipid bilayers (SLBs), it was shown, that actin filaments tethered to biotinylated lipids, would reorganize the domains in phase separated SLBs to resemble the actin network on top[103]. These findings show, that it is possible to organize lipid domains by increasing the local concentration of one phase-separating lipid, as well as through geometric effects.

1.3 Computer simulations

Simulations allow to do experiments on a computer, giving access to variables and quantities that are otherwise difficult to measure. They allow for the identification of key parameters in convoluted, complex systems with several mechanisms in parallel at play. Computational methods are used over many scales, from highly accurate *ab-initio* quantum computational methods to elucidate the behavior and electronic structure of small molecules, to molecular dynamics (MD) simulations that are used to describe large molecules, such as proteins and clusters of molecules using force-fields[104,105]. Where atomic accuracy is not needed, reactions and cellular processes, using experimentally known data can be simulated, which enabled the simulation of the whole *JCVI-syn3A* minimal cell[106].

In synthetic biology, computer modeling is often used to predict the structure and dynamics of macromolecules, such as DNA-origami. Software packages, like oxDNA allow for the simulation of DNA structures to aid in the design of DNA origami[107]. Static protein structures can be predicted from their amino-acid sequence using neural networks, such as Alpha-Fold[61]. These neural networks have been trained on the vast structural data available for proteins and can be used as a starting point for further MD simulations. MD simulations can shine light on the dynamic behaviors of proteins, that are in many cases important to understand the function. Often used are MD simulations to investigate the binding of small molecules to proteins. Such simulations give access to the coordinates relevant for the process at hand, as well as insight into the energy landscape[108]. Simulations in general help to gain a deeper understanding of the systems at hand, as each variable of interest can be modified and examined independently from others. This is especially valuable for variables, that are either not experimentally accessible, or cannot be changed in an independent manner in an experimental settings. Simulations thus allow for the estimation of the contributions of various components in complex systems[109].

1.3.1 Monte Carlo Simulations

Monte Carlo (MC) simulations can be seen as experiments on a computer and are useful for systems with many degrees of freedom, that cannot be computed analytically. MC simulations are statistical methods, in comparison to MD simulations that are deterministic. MC simulations utilize random numbers in their algorithm, with each simulation yielding a different result. Although no individual trajectory calculated by the simulation is expected to represent a real trajectory, the average over many such trajectories should represent the results found experimentally, assuming the equations used describe the effects at play well enough[110]. Here, we focus on random walk Monte Carlo, where a trial configuration is created based on the current configuration of the system and the probability of the transition into the proposed state is easily computable. Based on the transition probability, which can take values between zero and one, one can now accept or reject the proposed state. This decision is taken, by generating a random number from a uniform distribution between zero and one and comparing it to the probability of transitioning from the current configuration to the proposed state. One key point of Monte Carlo based methods is, that the trajectory is purely stochastic, where the practical viability of transitioning from one state to another is ignored[111]. This can increase the speed at which configuration space is explored, and thus lead to conclusions with low computing power.

In the presented work Monte Carlo simulations are used to explore domain localization in phase separated, deformed vesicles. Assuming, the energy of such a system is readily computed, the probability of a state in thermal equilibrium is given by the Boltzmann distribution :

$$p_i \propto e^{-\frac{\epsilon_i}{k_B T}} \tag{1.1}$$

with the energy ϵ_i corresponding to the state i. from there, we can take the probability ratio of two states i and j, as the Bolzmann factor:

$$\frac{p_i}{p_j} = e^{-\frac{1}{k_B T}(\epsilon_i - \epsilon_j)}. \tag{1.2}$$

In this case, state i would be the current state, and state j the proposed trial state. If the energy of state j is lower than the current state i, the move will be accepted. If the energy of the trial state j is higher than the energy of state i, the move will be accepted with a probability of $\frac{p_i}{p_j}$, given by equation 1.2, by comparing the value with a randomly drawn number $w \in [0, 1]$[112]. The higher energy state will thus be accepted, if $w < \frac{p_i}{p_j}$.

This allows us to sample the configuration space, in dependence of the probability of the occurrence of a particular state, and thus gain information experimentally relevant configurations. One should note, that the practical possibility of transitioning from state i to state j is ignored and a transition assumed to be possible.

Monte Carlo simulations were used earlier to explain domain organization in phase separated vesicles , showing that competition between line tension and vesicle curvature could lead to the emergence of complex pattern at the membrane of spherical GUVs[113]. In these simulations, the domain distribution is affecting the underlying vesicle shape, changing the equilibrium shape. This allowed for the investigation of complex domain shapes, which emerge in the presence of complex lipid mixtures. They showed, that contributions from membrane curvature together with the line tension contributions account for the phase morphologies examined in experiments[113]. In the simulations presented in this thesis, the underlying equations are simpler, as I assume the total energy to be line tension governed. In the here presented studies, I further fix the vesicle shape, as we want to explore the effect of a defined vesicle shape on the domain organization in phase separated vesicles.

1.4 Motivation and aims

Towards the creation of a synthetic cell, I am interested in exploring the emergence of polarity and molecular organization. This is a first step towards directed synthetic cell migration and strategies to recreate these using a bottom-up synthetic biology approach. The goal of this project is to induce polarity in GUVs by affecting the molecular organization inside using external cues.

In natural cells, the incredible complexity can mask effects and behaviors of proteins that are only visible in *in-vitro* experiments[114]. In order to be able to use a rational design approach, a deep understanding of the vital components and their interplay in confinement is of great importance. I want to explore pathways to induce polarity inside cell model systems, using a minimal set of components. The bottom-up synthetic approach allows for this endeavor in a controlled fashion, as every single component is intentionally added with the aim of recovering a function as simplistic as possible.

I utilize micropatterned surfaces to adhere and deform GUVs with the aim of affecting the molecular distribution inside. The general approach is depicted in Figure 1.6.

In the first step I show that micropatterns can be used to adhere and deform GUVs, similar to natural cells. I quantify the deformation of GUVs adhering to line-shaped micropatterns, and examine the deformation in dependence of GUV size.

Actin stress fibers orientating along the axis of migration are a hallmark in mesenchymal cell migration[45]. I investigate wether such an organization of actin bundles can be achieved by GUV deformation using only geometrical cues. I reconstituted actin bundles using the bundling protein fascin inside of adherent, deformed GUVs and assess the angular distribution of the bundles. Assuming the bundles to be straight rods inside a rigid confinement, i compare the experimentally obtained distributions with the results from such a simple theoretical model. Next, I use dextran as a crowder to bundle actin filaments which additionally localizes them at the GUV periphery by depletion effects, creating a synthetic actin cortex-like structure. I show, that actin organizes in such deformed GUVs, by avoiding the strong membrane curvature at the adhesion-site. I further show that these synthetic actin cortices decrease the deformability of GUVs using the adhesion based assays, as well as RTDC experiments.

In the last step I utilize phase-separated GUVs as a model for a system that exhibits polarity and attempt to control the domain organization using adhesive micropatterns. Phase separated membranes can be used as scaffolds to guide protein organization to potentially induce polarity[71]. I show that the domains in a phase separated GUV organize by localizing biotinylated lipids at the adhesion site, as it has been reported before, as well as using the deformation to localize phases. Finally, I use Monte Carlo simulations to explain the domain localization induced by GUV deformation, as observed in the experimental results.

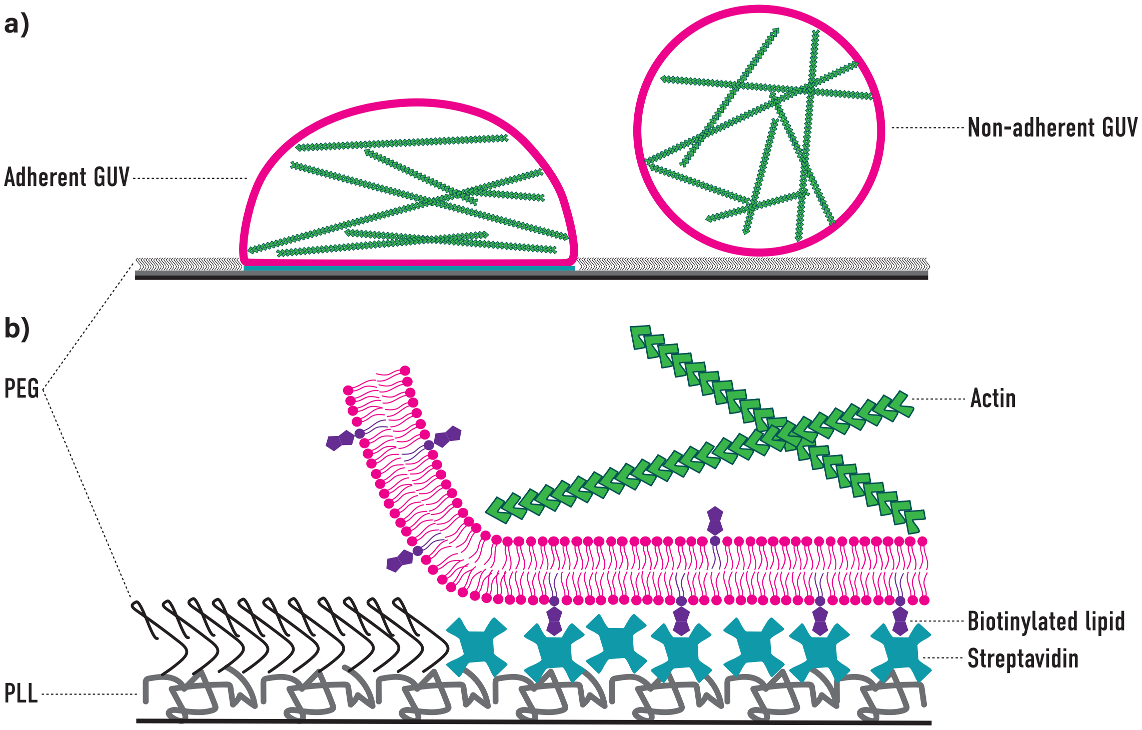

Figure 1.6: Sketch visualizing a GUVs adhering to a micropatterned surfaces. In **(a)**, an adherent GUV on a micropattern is shown next to a non-adherent GUV. The GUV membrane (magenta) is functionalized with biotinylated lipids, shown in violet. In **(b)**, the molecular structure of the micropattern is visualized. The micropatterned area is filled with streptavidin (cyan), allowing trough adhesion of GUVs mediated by the interaction of biotin and streptavidin. The efffect of the deformation induced by the adhesion on cellular components, such as actin filaments (green) is then observed. Figure adapted from Fink et al.[29].

2 Materials and methods

2.1 GUV compositions

2.1.1 GUV compositions used for the emulsion transfer method

Table 2.1: GUV composition 0

Lipid	mol%
DOPC	80.0
DOPG	20.0

Table 2.2: GUV composition 1

Lipid	mol%
DOPC	79.5
DOPG	20.0
Liss-RhodPE	0.5

Table 2.3: GUV composition 2

Lipid	mol%
DOPC	79.5
DOPG	20.0
Atto488-DOPE	0.5

Table 2.4: GUV composition 3

Lipid	mol%
DOPC	78.5
DOPG	20.0
Liss-RhodPE	0.5
Biotin-PEG2k-DSPE	1.0

Table 2.5: GUV composition 4

Lipid	mol%
DOPC	78.5
DOPG	20.0
Atto488-DOPE	0.5
Biotin-PEG2k-DSPE	1.0

Table 2.6: GUV composition 5

Lipid	mol%
Biotin-PEG2k-DSPE	0.5
Chol	79.5
DOPC	9.5
DPPC	9.5
Liss-RhodPE	0.5
TF-Chol	0.5

Table 2.7: GUV composition 6

Lipid	mol%
Chol	80.0
DOPC	9.5
DPPC	9.5
Liss-RhodPE	0.5
TF-Chol	0.5

Table 2.8: GUV composition 7

Lipid	mol%
DOPC	78.5
DOPG	20.0
Atto-647n DOPE	0.5
Biotin-PEG2k-DSPE	1.0

2.1.2 GUV compositions used for electroformation

Table 2.9: GUV composition 8

Lipid	mol%
Biotin-PEG2k-DSPE	2.0
Chol	19.0
DOPC	39.5
DPPC	38.0
Liss-RhodPE	0.5
TF-Chol	1.0

Table 2.10: Lipid stock solutions

Lipid	concentration
Atto488-DOPE	1 mg/ml
Biotin-Peg2k-DSPE	10 mg/ml
Chol	50 mg/ml
DOPC	25 mg/ml
DOPG	25 mg/ml
Liss-Rhod-PE	1 mg/ml
Tf-Chol	1 mg/ml

2.1.3 Buffers used for emulsion transfer

Table 2.11: Outside buffer

Reagent	concentration
Imidazole buffer, pH 7.6	5 mM
Glucose	250 mM (to adjust outside buffer to 305mOsm)

Table 2.12: Inside buffer, empty GUVs

Reagent	concentration
dPBS	1x
Opti-Prep	20 %)

Table 2.13: Inside buffer, GUVs with actin and fascin

Reagent	concentration
Imidazole buffer, pH 7.6	5 mM
Tris buffer, pH 8.0	2 mM
KCl	50 mM
$MgCl_2$	2 mM
EGTA	1 mM
Opti-Prep	20 %)
Actin	5 µM
Fascin	0.5 µM
Adenosine 5'triphosphate	1 mM

2.2 Reagents and machines

Table 2.14: Inside buffer, GUVs with actin and dextran

Reagent	concentration
Imidazole buffer, pH 7.6	5 mM
Tris buffer, pH 8.0	2 mM
KCl	50 mM
$MgCl_2$	2 mM
EGTA	1 mM
Opti-Prep	20 %)
Actin	Depending on experiment
Dextran	Depending on experiment
Adenosine 5'triphosphate	1 mM

Table 2.15: List of reagents

Reagent	Company
d-PBS buffer pH7.4	Gibco, Thermo Fischer Scientific, Waltham, USA
3’-Biotin-TEG-aaaaaaaaaaaaaaaaaaaa-5’	biomers.net, Ulm, Germany
3’-Cy5-aaaaaaaaaaaaaaaaaaaa-5’	biomers.net, Ulm, Germany
3’-Cy5-tttttttttttttttttttt-5’	biomers.net, Ulm, Germany
3’-Cholesterol-tttttttttttttttttttt-5’	biomers.net, Ulm, Germany
PLPP gel	Alveole, Paris, France
Surfactant mix	Alveole, Paris, France
DOPC	Avanti Polar Lipids, Alabaster, USA
DPPC	Avanti Polar Lipids, Alabaster, USA
Biotin-PEG2k-DSPE	Avanti Polar Lipids, Alabaster, USA
DOPG	Avanti Polar Lipids, Alabaster, USA
Top Fluor-Cholesterol	Avanti Polar Lipids, Alabaster, USA
Cholesterol	Avanti Polar Lipids, Alabaster, USA
18:1 Liss Rhod PE	Avanti Polar Lipids, Alabaster, USA
Atto 488 DOPE	Sigma-Aldrich, St. Louis, USA
Albumin, Fraction V	Merck, Darmstadt, Germany
Dextran 100	Carl Roth, Karlsruhe, Germany
Opti-Prep	Merck, Darmstadt, Germany
n-Decane	Merck, Darmstadt, Germany
Mineral Oil	Merck, Darmstadt, Germany
Silicone Oil, 50 cSt	Merck, Darmstadt, Germany
Poly-l-lysine 0.01% solution	Merck, Darmstadt, Germany
Sir-actin,	Spirochrome, Stein am Rhein, Switzerland
Streptavidin, Alexa Fluor 405 conjugate	Life Technologies, Eugene USA
Adenosine 5’triphosphate magnesium salt	Merck, Darmstadt, Germany
Rabbit smooth muscle actin	Hypermol, Bielefeld, Germany
Fascin, human, recomnbinant	Hypermol, Bielefeld, Germany
Imidazole	Sigma-Aldrich, St. Louis, USA
NaCl	Emsure, Darmstadt, Germany
$CaCl_2$	Carl Roth, Karlsruhe, Germany
Coverslips, 60x24 mm, #1.5	Carl Roth, Karlsruhe, Germany
Imersol 518F	Carl Zeiss, Oberkochen, Germany
Imersol W2010	Carl Zeiss, Oberkochen, Germany
Ni-NTA magnetic agarose beads (5%)	Serva Electrophoresis, Heidelberg, Germany

Table 2.16: List of devices

Device	Company
LSM800	Carl Zeiss, Oberkochen, Germany
LSM880	Carl Zeiss, Oberkochen, Germany
Zeiss 40x W, 1.1 wDicIII Objective	Carl Zeiss, Oberkochen, Germany
Zeiss 63x Plan Apochromat Obective	Carl Zeiss, Oberkochen, Germany
5425R benchtop centrifuge	Eppendorf, Hamburg, Germany
Mikro 200 R benchtop centrifuge	Hettich Zentrifugen, Tuttlingen, Germany
Vesicle Prep Pro electroformation chamber	Nanion Technologies, Munich, Germany
Osmomat 0-30D	Gonotec Mess- und Regeltechnik, Berlin, Germany

2.3 GUV production

2.3.1 General remarks

GUVs presented in this work have been produced using either the emulsion transfer, also known as inverted emulsion or the electroformation method, depending on the experimental requirements[29,86,115]. In general, electroformation gives GUVs with a well defined lipid composition, in the here presented case especially used for the production of phase separated GUVs[96,116]. The inverted emulstion method allows for the encapsulation of various proteins, macromolecules and buffers into the inside of GUVs, but suffers from a not well defined lipid composition due differential partitionning of various lipids, such as cholesterol into the oil, as well as contamination of the produced GUVs with oil from the production process[70,71]. Due to this, it is generally assumed, that the lipid composition of GUVs formed using the emulsion transfer method might not be precisely the parts added to the oil phase. If the question arises, which oil to use, mineral oil tends to give lower yield, but less defects (like oil-residues and llipid remnances) than silicone oil, so if a very large amount of GUVs is not needed, and no lipids, that heavily partition into the oil phase, like cholesterol is used, I would generally advice to use mineral oil to form GUVs. One should note, the lipid compositions listed in part 2, section 2.1 refer to the compositions used for making the lipid-in oil mixtures, and not the final compositions found in the GUVs. Lipids were stored at -20 °C as stock solutions dissolved chloroform, unless noted otherwise.

2.3.2 Emulsion transfer

The general scheme of emulstion transfer is shown in Figure 2.1. Lipids dissolved in chloroform were mixed in 2 mL low-adhesion glass vials to a final concentration of 643 µM (for GUV composition 1 - 4) or 1 mM (GUV composition 5 - 6), see part 2, section 2.1 at 1 ml final volume. The lipids were dried in vacuum and redissolved in 60 µL n-Decane. 940 µL oil was added (For GUV composition 1- 4 mineral oil, for GUV composition 5-6 silicone oil), and the mixture was mixed. 500 µL outside-buffer (5 mM imidazole-HCl buffer, pH 7.6, with sucrose added to match the osmolarity of the inside solution of 305 mOsm if not noted otherwise, see Table 2.11) was added to a 2 mL eppendorf tube. 400 µL of the lipid-in-oil mixture was layered carefully on top of the outside buffer to not disturb the interface and left to incubate for at least 45 min. The remaining oil was kept under nitrogen gas. Then 10 µL of inside-buffer was added to the remaining lipid-in-oil mixture in the low-adhesion glass vial (Inside solution composition is dependent on the experiments, and listed in Table 2.12, 2.13, and 2.14). An emulsion

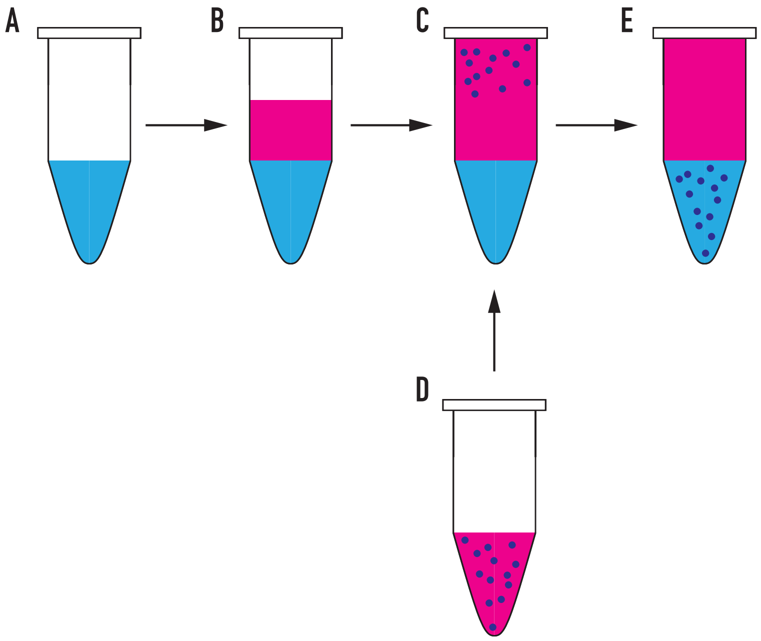

Figure 2.1: Scheme of GUV production using emulstion transfer. The outside-buffer shown in blue in an eppendorf tube (A) is layered with the lipid-in oil solution (magenta) as shown in B and let to rest. Then, the remaining oil is mixed with the inside phase (lila) to create a water-in-oil emulsion (D), which is then added on top of the oil layer. The mixture is then centrifuged, and the GUVs can be obtained after removal of the oil layer on top.

was generated by pipetting the mixture up and down vigorously using a pasteur glass pipet and added on top of the oil layer in the 2 mL eppendorf tube. The tube is then centrifuged at 380 rcf for 3 min. Then the oil layer is removed together with the interface layer, that 200 µL solution is left. The GUVs are vortexed for a second before being used.

2.3.3 Electroformation

GUVs were produced as described before[96]. In short, 40 µL lipid mixture, dissolved in chloroform at a concentration of 1 mM was spread on an ITO glass slide using a coverslip to obtain an even coating. The ITO slide was then placed under vacuum for 30 min to dry the lipid film. An 18mm rubber o-ring was covered with silicone fat and carefully placed on the lipid coated ITO slide to create a chamber. The ring was filled with 280 µL 300 mM sucrose solution. A second ITO slide is aded on top to seal the chamber. A programmable AC field, was used to generate the GUVs at 70°C, as described in [96]. GUVs were stored for up to one week at 4°C. Before Usage, GUVs were diluted 20x in 300 mM glucose to let them sediment.

2.4 Micropatterning

2.4.1 General remarks

Micropattern were generated using established protocols using maskless photolithography, which allowed for fast changes and optimization of pattern sizes and design, in comparison to the often used chromium masks. I would like to point out, that much lower UV doses, than the parameters suggested by the alveole application note of 20-30 mJ/mm^2 gave the best results in terms of GUV adhesion and pattern quality[117]. Further, the protocol was optimized to reduce material consumption and manual labor, as well as increase throughput.

2.4.2 Micropatterning protocol

60x24 mm glass coverslips were plasma treated for 3 min, at 300 W, 0.5 mBar O_2 pressure. Then the silicon part of ibidi removable 12 well chambers was attached to the upper side of the coverslips. Then, 100 µL PLL, 1% was added to each well and incubated for 30 min. The wells were washed 2x with 300 µL PBS, PH 7.4. Then 100 µL PEG-SVA(MW 5000) at a concentration of 5 mg/ml in PBS was added and left to incubate for at least 1 h. The wells were washed 2x with purified water. 5 µL surfactant mix were added to 600 µL ethanol. Then, 1 µL PLPP-gel was added to each well and spread evenly using the ethanol-surfactant mix, while the coverslip was tilted from one side to the other.The surfactants ensure hereby an even coating of the wells. The ethanol was then evaporated on a hotplate at 100°C for 5 min. The wells were then patterned using the Alveole Primo setup at a power of 5 mJ/mm^2, the used patterns are shown in figure 2.2 and 2.3. The focus was set to the top of the coverslip, using Nikons Perfect Focus System (PFS), to keep the distance of the coverslip, and thus the focus stable during the complete patterning process. The white areas in the digital masks are the areas, where the coverslip will be illuminated. The wells were then washed 3x with 300 µL PBS and stored at 4°C in PBS for up to 2 months. For functionalization with protein, the well was incubated with 100 µL protein for at least 1 hour at a concentration of 40 ng/ml in PBS. The wells were then washed 2x with 300 µL PBS and 1x with the same buffer used as the outside buffer for making the GUVs, without letting the surface get in contact with air. The functionalized surfaces were used immediately.

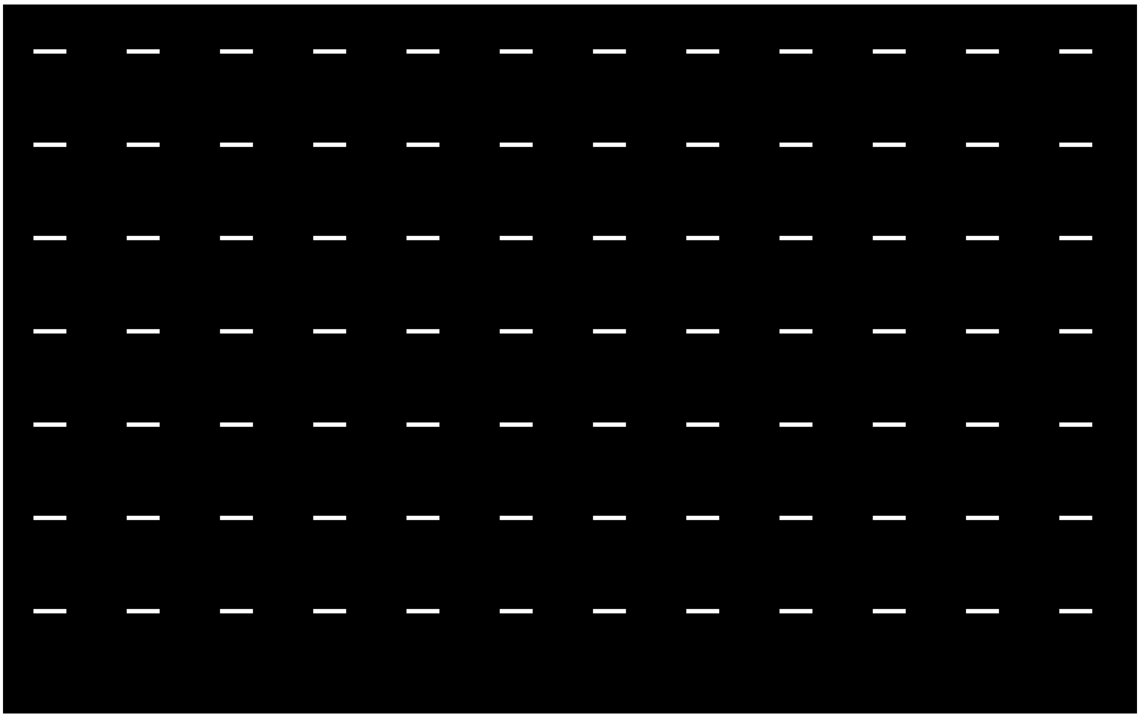

Figure 2.2: Line micropattern used for GUV deformation and adhesion. The length of the lines corresponds to approx. 15 µm, and the width 2 µm.

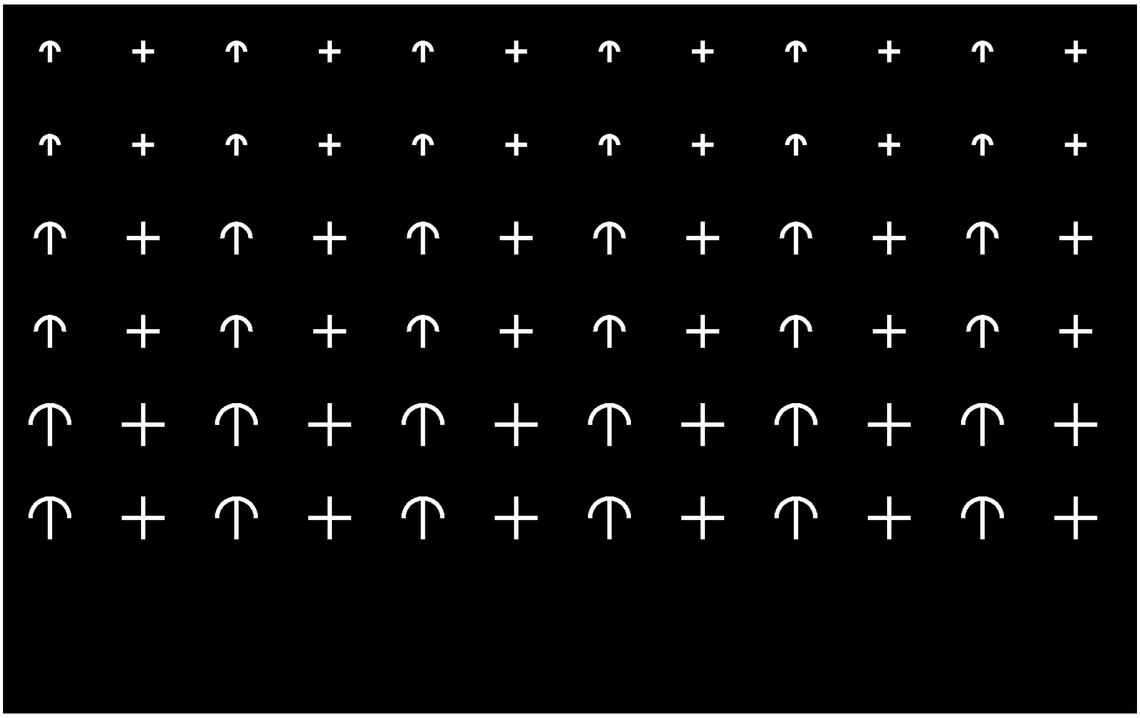

Figure 2.3: Cross and crossbow micropattern used for GUV deformation and adhesion. The width of the pattern corresponds to approx. 10 µm for the first 2 rows, 15 µm for for rows 3 and 4, and 20 µm for rows 5 and 6, with a linewidth of 2 µm.

2.5 GUVs on micropattern

The images shown in this work were obtained on a Zeiss LSM 800 or LSM 880 inverted confocal microscope, with a 63x/1.4 Plan Apochromat oil immersion and a 40x/1.1 DicIII water immersion objective. The images were adjusted for brightness and contrast in Fiji. When GUVs were not adhered to micropatterned surfaces, they were imaged in wells, where the silicone part of ibidi 12-well slides was stuck to a 60x24 mm coverslip. Then the well was passivated with a 1% BSA solution in PBS for 15 min and washed 2x with PBS. 100 µL of the GUV solution was added. The wells were imaged immediately.

2.5.1 Adhering GUVs on micropattern

Micropatterned wells were functionalized using Af405 labeled streptavidin as described in part 2 in section 2.4. GUVs were produced using either electroformation or emulsion transfer, with lipid compositions, as shown in Table 2.4, 2.5, 2.6 or 2.9. 100 µL of the GUV solution was added to a well and imaged immediately using confocal microscopy.

2.5.2 DNA mediated adhesion

The micropattern were functionalized with streptavidin, as described before. Then, 100 µL 20-A DNA oligomers functionalized with biotin (3’-Biotin-TEG-aaaaaaaaaaaaaaaaaaaa-5’) were added at a concentration of 100 nM to the pattern and left to incubate for 15 min. The pattern was washed 2 times with 300 µL PBS and 1x with the same buffer used as the outside buffer for the GUVs, without letting air touch the surface. For the control experiments, 10 nM Cy5 tagged 20-T DNA oligomers (3’-Cy5-tttttttttttttttttttt-5’) were added to the micropatterned surface and left to incubate for 15 min. The Well was washed with PBS and imaged using confocal microscopy.

The GUVs (Using GUV composition 0 and 2) were incubated with cholesterol tagged 20-T DNA oligomers (3’-Cholesterol-tttttttttttttttttttt-5’) at a concentration of 100 nM for 15 min. To check for the insertion, 100 nM 20-A Cy5-tagged DNA oligomers (3’-Cy5-aaaaaaaaaaaaaaaaaaaa-5’) were added to the GUV solution and imaged using confocal microscopy. To adhere GUVs to the micropatterned surfaces, 100 µL GUVs was added without washing to the poly-A functionalized wells and imaged immediately.

2.5.3 Analysis

The analysis of of GUV deformation was performed as described in Fink. et. al.[29]. GUV deformation was measured on 15 µm long line pattern. Z-stacks of GUVs were acquired with a a slice thickness of 0.5 µm. The slice with the highest brightness of the Af405-Streptavidin pattern was assumed to be the bottom part, and thus the slice of the adhesion side. The deformation was then analyzed 2 µm above this slice by taking the ratio of major and minor axis, measured manually in Fiji.

As described in Fink. et. al.[29], actin filament orientation was analyzed by tracing the filaments using SOAX, fitting a line and calculating the angle. To this end GUVs with actin bundles on the inside were prepared using the emulsion transfer protocol with mineral oil as described before. To stain actin filaments 0.25 µL SIR-actin dissolved in DMSo was added to the outside buffer of the GUVs after formation, and vortexed.

To reconstruct the GUV surface, a z-stack of an adherent GUV, obtained using 40x, f1.2 water-immersion objective was used to minimize geometric distortions was used as a basis. First, the z-stack was cropped to cut out surrounding GUVs. Then, the z-stack was imported into GeoV, which was used to reconstruct the GUVs[118]. Reconstructed GUVs were exported as wavefront *obj.* files, and rendered using Blender. For the usage in simulations, the reconstructed surface was smoothed before export using Blenders minimize laplacian function.

2.5.4 RTDC

RTDC measurements were done in collaboration with Tobias Abele. An AcCellerator (Zellmechanik Dresden) was used for RTDC measurements, equipped with a high-speed CMOS camera (MC1362, Microtron) on an inverted AxioObserver with an 40x/0.65 objective. Vesicles were formed using CellCarrier B (Zellmechanik Dresden), as their outside phase, using the emulsion transfer protocol. The GUVs were loaded into 1 mL glass syringes and injected into the device using syringe pump. For all measurements, 20 µm wide channels (Flic20, Cellmechanik Dresden) PDMS chips were used. Measurements were conducted at a flow rate of 0.06 µL/s. Shape-In2 was used for the anaysis of the data. Scatter-plots were created using python3 with the matplotlib package.

2.5.5 Simulation of phase separation on arbitrary triangulated surfaces

For the simulation of phase separated vesicles, triangulated surfaces, were used, that can describe almost any shape of interest. The line energy was calculated on these surfaces, by assigning a phase to each triangle and calculating the energy penalty, when two neighbouring triangles have different phases. To calculate the energy difference between two states p and q, where the phase of two triangles i and j was exchanged is computed with the following equation, implemented in python:

$$
\begin{aligned}
\left[\epsilon_p^{i,j:i\neq j}\right] - \left[\epsilon_q^{i,j:i\neq j}\right] &= \sigma\left[\sum_s^3 1-\delta_{(\phi(i)=a)\phi(s)}l_{is} + \sum_s^3 1-\delta_{(\phi(j)=b)\phi(s)}l_{js}\right] \\
&- \sigma\left[\sum_s^3 1-\delta_{(\phi(i)=b)\phi(s)}l_{is} + \sum_s^3 1-\delta_{(\phi(j)=a)\phi(s)}l_{js}\right]
\end{aligned}
\tag{2.1}
$$

This can now be plugged into equation 3.6, to give the probability ratio between the two states.

In the python implementation we now use the rand() function of numpy to generate a uniform random number w between 0...1, used to decidewhether to accept the new proposed state in a Monte-Carlo based approach, using:

$$
\mathrm{w} < e^{-\frac{1}{kT}(\epsilon_q-\epsilon_p)}. \tag{2.2}
$$

For the computations, an input file, specifying the triangulated surface as .obj file, the line-tension value (σ), the radius (10 000 nm = 10 µm), and the part of one phase (75%, in all cases shown in this work) needed to be specified. From there, the simulation was run for $5x10^1$0 proposed states, starting from a randomly distributed state, using Python 3.12 and numpy 1.26.4 on an Apple M1 MacBook Pro with 16 GB memory on OsX 13.6.1., s a snapshot every $5x10^7$ iterations[119,120]. Each simulation was run at least 3 times from a random starting configuration, when no other starting configuration was specified. The results were analyzed and plotted using python with the matplotlib package. Images were generated using blender to render the phase separated vesicles.

For the phase separation simulations, this is an example input file:

```
infile: GUV_sim/PS/guv_line.obj
r_soll: 10000.0
sigma: 0.05
outdir: 75_perc_guv_line/sigma_0.05_1/
phase_part: 0.75
```

Where *infile* is the triangulated surface, *r_soll* is the radius in nm, *sigma*, the line tension is given in pN and *phase_part* is the partition of one phase. The partition of the other is calculated as 1-*phase_part*.

3 Results

Living cells are highly complex in their composition as well as their convoluted regulatory networks and factors that determine their behaviour. Part of this observed complexity stems from their ability to react to outside cues from their environment, with each individual cell showing slight differences in their displayed behaviors. To help standardize this environment, micropatterns are used, where cells are given well-defined micro-environments, with control over the ligands adhered to the surface as well as their shape and size. I set out to introduce this method to bottom-up synthetic biology, to improve reliability and control of molecular organization in synthetic cells. Deformation and adhesion could thus be used as a tool to break the high symmetry spherical GUVs tend to have, and allow for the controlled organization of molecular assemblies. Actin organization is a key characteristic in polarized, motile cells, and it was therefore chosen as a goal to achieve such an organization in synthetic cells. While micropatterns are a well established tool for the control of natural cells, it was necessary to validate the binding of Streptavidin, which we chose as a simple option to bind to a biotin functionalized GUV membrane and thus allow for the deformation of GUVs. Further, the functionalization the GUV membrane with biotinylated lipids was validated, as the insertion efficiency of various lipids is strongly method dependent. The Emulsion transfer method allowed for the incorporation of Biotin-Peg2k-DSPE while being very tolerant to various salts and proteins. It was thus used to create the GUVs for most of the experiments presented in this thesis, as it additionally allowed for the encapsulation of proteins, such as actin. In the later sections we explore a more engineering based approach to the introduction of polarity into synthetic cells, utilizing membrane phase separated vesicles. These phases exhibit distinct physical and chemical properties, allowing for the functionalization of each phase independently. I show that it is possible to organize phases using the geometrical cues provided by micropatterns, which could in the future be used as a scaffold to organize proteins and thus provide a fully synthetic way to approach polarity in GUVs. Last, I show that this organization can be explained by line-tension contributions only, using Monte-Carlo simulations.

3.1 Development of the experimental setups

3.1.1 GUV characterization and functionalization with biotinylated lipids

For bottom-up synthetic cell studies, cell-sized GUVs are often used as a starting point, as they provide a simple mimic of the cell membrane, compartmentalizing space into an intra- and extracellular part, divided by the synthetic cell membrane. This membrane can be built up of various lipids with selected functionality, depending on the needs and goals of the experiments. Further, various macromolecules like proteins can be encapsulated on the inside and thus provide additional functionality to the vesicle. GUVs are, when not disturbed, spherical in shape, similar to cells that have not yet adhered to a substrate, shown exemplarily in Figure 3.1. A bright field image of a free floating GUV is shown in Figure 3.1**b**. Although the general shape of the cells is roughly spherical, many thin protrusions and imhomogenities inside the cell can be observed, that are not found in the spherical GUV. A z-stack showing the fluorescently labeled membrane of a free floating GUV as comparison is depicted in Figure 3.2, emphasizing the spherical nature of the GUV.

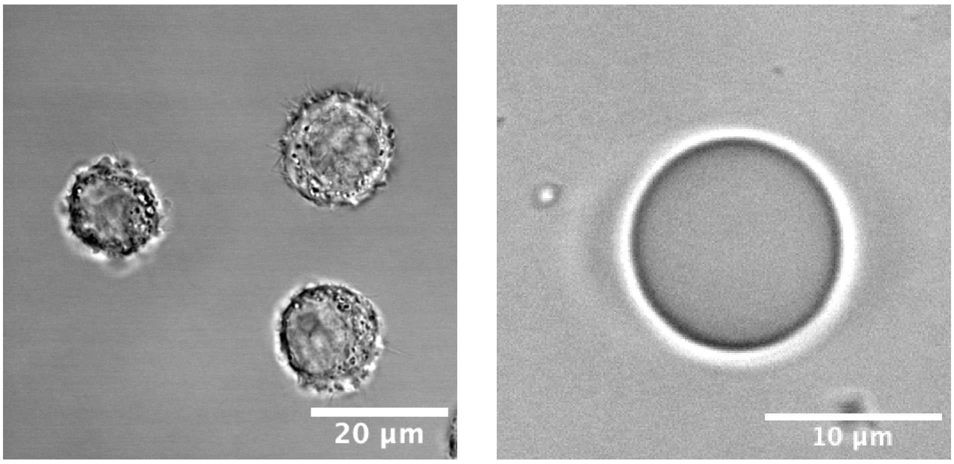

(**a**) MDCK cell (**b**) GUV

Figure 3.1: (a) Image of a MDCK cell on glass substrate. The unpolarized round shape before it adheres and becomes motile. Cells were provided by Michelle Kemper. Scale bar is 20 µm **(b)** GUV in a brightfield microscopy image. Scale bar is 10 µm

GUVs were functionalized with Biotin-PEG2k-DSPE lipids using the emulsion transfer protocol (See Table 2.4 for the precise GUV composition). Biotin binds streptavidin with a dissociation constant of $2.5x10^{-13}$ to 10^{-15} M and is known as one of the strongest non-covalent interactions of natural proteins and ligands[121–123]. This strong interaction can thus be used to adhere GUVs to a surface, and is here to be combined with micropatterns[124].

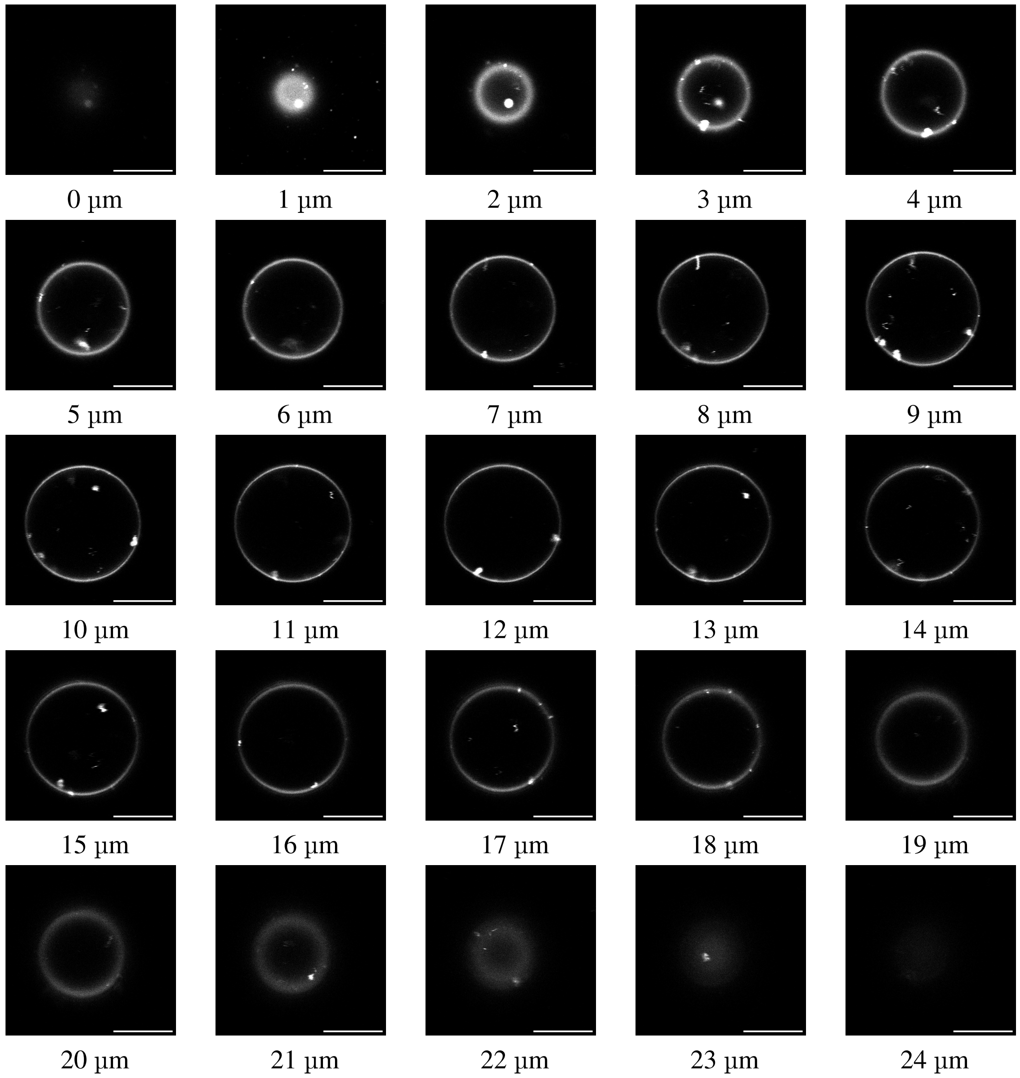

Figure 3.2: A z-stack of a non-adherent GUV, with the z height indicated by the numbers below the individual images. The Liss-Rhod labeled membrane is shown. Scale bar is 10 µm.

To verify the successful inclusion of the Biotinylated lipids into the GUV membrane, fluorescently labeled streptavidin was added to the outside buffer. There it only binds to the GUV membrane, if the functionalization with biotin was successful and thus give an increased fluorescence signal at the GUV periphery. The experiment, together with a control that lacks biotinylated lipids is shown in figure 3.3. It can be seen, that streptavidin only binds to the GUVs in the presence of biotinylated lipids, indicating the successful incorporation of such functionalized lipids using emulsion transfer. In the absence, the fluorescent signal of the free floating streptavidin is seen, without exhibiting any interactions with the GUV membrane (Figure 3.3**b**).

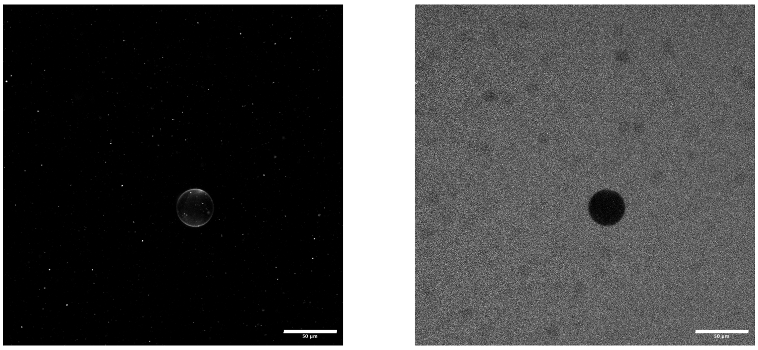

(a) GUV membrane without biotinylated lipids.

(b) Fluorescent Streptavidin-Af405 in the bulk.

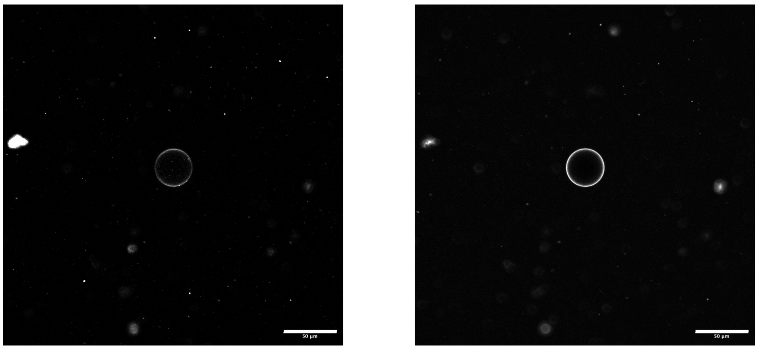

(c) GUV membrane with biotinylated lipids.

(d) Fluorescent Streptavidin-Af405 in the bulk interacting with the GUV.

Figure 3.3: Validation of the interaction of streptavidin with biotinylated lipids in the GUV membrane using confocal microscopy. In **a**, the LissRhod channel, visualizing the membrane of a GUV that does not have biotinylated lipids in the membrane is shown. In **b**, the fluorescent Streptavidin-Af405 is shown. One can see the free floating streptavidin in the bulk solution. The missing fluorescence where the GUV is located is visible, indicating that streptavidin is not interacting with GUVs, when their membrane composition does not include Biotin. In **c**, the GUV membrane of a GUV with biotin-PEG2k-DSPE is shown. In **d**, the fluorescent streptavidin in the bulk solution can be seen interacting with the GUV membrane. In **a** and **b**, a GUV using lipid composition 1, a lipid composition without biotinylated lipids and in **c** and **d** a GUV using composition 3, a lipid composition with biotinylated lipids is shown. The scale bars are 50 µm

3.1.2 Functionalization of micropatterned surfaces with streptavidin

Micropatterned surfaces with various shapes have been functionalized with many proteins, such as antibodies or ECM proteins to present these ligands in a controlled way to living cells[125–127]. Further micropatterns provide a valuable tool to control cell shape and subsequently, polarity by leading to deformation in adherent cells[27,28,128]. Thus it was apparent that micropatterning could be used as a tool to deform and subsequently polarize synthetic cells in a similar fashion. ECM proteins, which are often used to adhere living cells were assumed impractical, as they tend to rely on membrane-proteins, that are difficult to incorporate into GUVs for their interaction and subsequent adhesion[129]. To showcase the applicability of the general concept of utilizing micropatterning for synthetic cell research, I use the strong interaction between streptavidin and biotin to mediate the adhesion of GUVs to the micropatterned surface. Streptavidin is a tetrameric protein which is expected to decorate a micropatterned surface utilizing the same non-specific interactions, used to functionalize the surfaces with ECM proteins. With this, GUVs could be adhered and deformed on micropattern with similar sizes and comparably to the way, micropatterns are used for natural cells. This has the potential to catalyze advancements in the field, enabling comparison of the effects of deformation on natural and synthetic cells.

Therefore, I had to test whether streptavidin would decorate micropatterned surfaces and still be able to interact with biotin. To this end, Alexa-fluor405 labeled streptavidin was used to functionalize the micropatterned surfaces, as it can be seen in Figure 3.4**a**. One can clearly see the streptavidin signal in the shape of the stripe pattern. Thus it can be assumed, that the functionalization of the pattern with streptavidin worked as intended.

In the next step, I verified the functionality of the streptavidin bound to the surface. Therefore an Atto647n-Dye linked to biotin was added, shown in figure 3.4**b**. From there one can observe the binding of the biotinylated dye to the micropatterned surface in the same shape as the streptavidin. It was thus demonstrated, that micropatterns can be functionalized with streptavidin.

In further experiments I thus utilized micropatterns that were functionalized with streptavidin to adhere and deform GUVs.

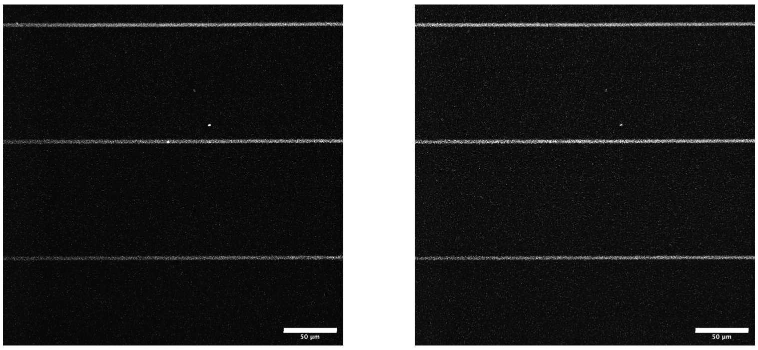

(a) Af405-Streptavidin functionalized line pattern.

(b) Atto647n functionalized biotin bindsto the streptavidin functionalized micropattern.

Figure 3.4: Validation of functionalized micropatterned surfaces. Shown is a confocal image of streptavidin binding to the micropatterned surface **(a)**. The streptavidin can then bind a biotin functionalized dye for visualization **(b)**. Scale bar 50 µm.

3.2 GUV deformation on micropatterned surfaces

3.2.1 Adhesion of GUVs to micropatterned surfaces leads to GUV deformation

With the foundations laid, I set out to adhere GUVs onto micropatterned surfaces. To this end, GUVs were made using the emulsion transfer method with compositions 3 and 4 (Table 2.4 and 2.5). The opti-prep in the inner buffer ensures a higher density of the GUVs in comparison to the outside medium, facilitating the GUV formation with the emulsion transfer method, as well as the settling onto the micropatterned surface. In Figure 3.5 a z-stack of an adherent GUV on a stripe micropattern is depicted. The micropatterned surface is shown in cyan, and the GUV membrane in magenta. The z-slice, where the streptavidin intensity was highest was defined as 0 µm height. The deformation of the GUV on the pattern can be seen, as its shape directly above the micropattern at 0 µm is elongated and oval, when compared to the free floating vesicle shown in figure 3.2. The most pronounced elongation of the Giant Unilamellar Vesicle (GUV) is observed in close proximity to the surface and diminishes gradually with an increased distance from the pattern. Another, welcomed side-effect of using micropatterns for imaging is the immobilization of the adherent GUV, which simplifies the acquisition of z-stacks or time-series.

Adhesion was not observed in the absence of biotinylated lipids in the GUV membrane, pointing to the adhesion being mainly mediated by the interaction with streptavidin. A vesicle that is not adhered to the micropattern does not show deformation, as observed in Figure 3.5 as does not interact with the streptavidin functionalized surface and keeps its spherical shape as observed for a free floating GUV (see Figure 3.2). Further, since it is not adherent, a GUV without biotin is not immobilized.

A z-STED image of a GUV adhering to a line is shown in Figure 3.6. Shown is an orthogonal cut of the membrane, stained with Atto-647n-DOPE, where the GUV adheres to the line pattern at the bottom of the image. In Figure 3.6a, an overview of the complete adherent GUV is shown. In 3.6b, the detailed view of the thin membrane protrusion can be seen. The adherent, bottom side of the protrusion is flat. The thin protrusion bears some similarities to the flat membrane in filopodia. Such a behavior has been theoretically predicted for vesicles on, strongly adhesive stripes by Lipowsky et al.[130]. These protrusions with their high curvature also point to the strong deformability of GUVs.

To further demonstrate the adaptability of micropatterns for synthetic cell research, GUVs were adhered to crossbow and cross shaped micropatterns of various sizes, shown in Fig-

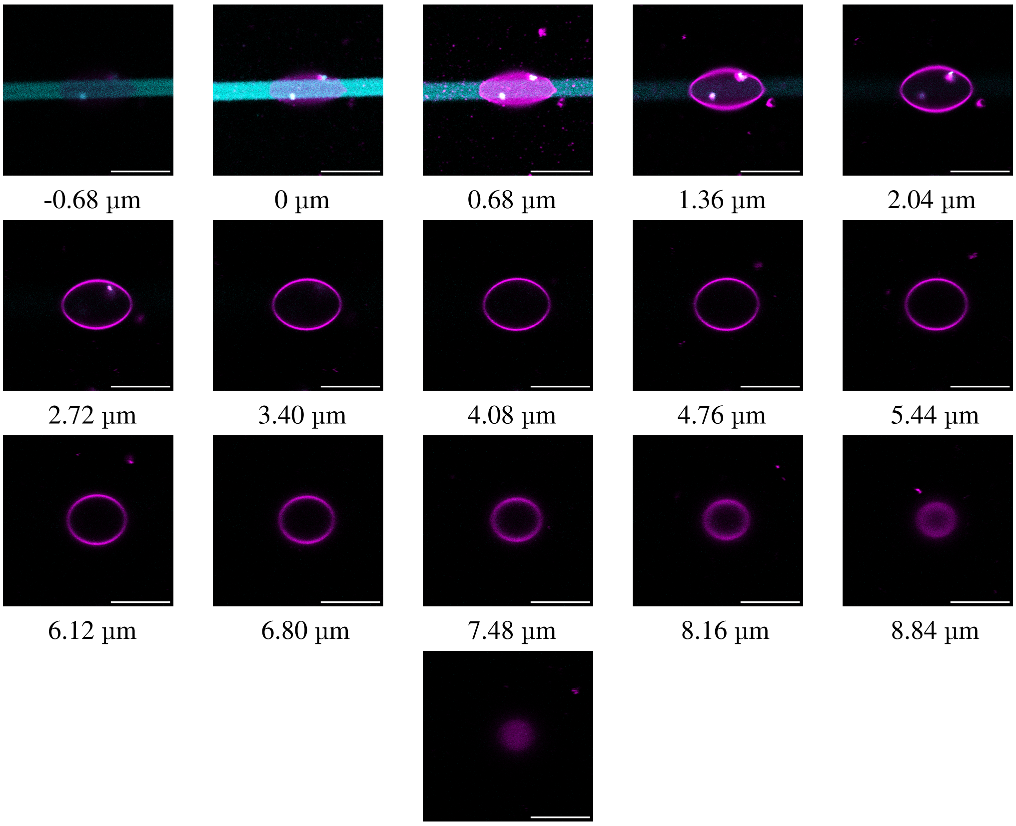

-0.68 µm
0 µm
0.68 µm
1.36 µm
2.04 µm
2.72 µm
3.40 µm
4.08 µm
4.76 µm
5.44 µm
6.12 µm
6.80 µm
7.48 µm
8.16 µm
8.84 µm
9.52 µm

Figure 3.5: A z-stack of a representative GUV (membrane labeled in magenta) adhering to a line pattern (Streptavidin-Af405 in cyan) is shown, with the z height indicated by the numbers below the individual images. One can see the strong deformation of the GUV close to the pattern. The slice, where the pattern shows the highest intensity was chosen as 0 µm slice. Scale bar is 10 µm.

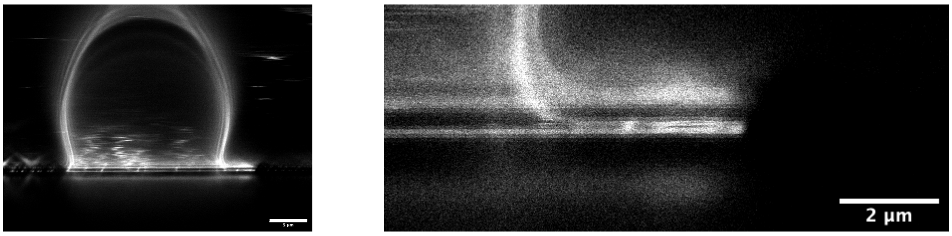

(a) Cut through a GUV adherent to a line. Scale bar is 5 µm

(b) Detail view of the right side of the GUV. Scale bar is 2 µm.

Figure 3.6: STED image of an adherent GUV. The membrane is shown. In a, one can see the inward curvature at the left side of the GUV, and the thin protrusion at the right. In (b) a detail view of the protrusion is shown.

ure 3.7 and published in Fink. et al.[29]. The streptavidin is labeled with AlexaFluor405, and is shown in cyan at the surface slice, where its intensity was highest. The membrane is shown 2 µm above the streptavidin pattern, to allow for the visualization of both parts simultaneously, the pattern and the deformed membrane in the same image. GUVs on crossbow shaped micropatterns were chosen to create a synthetic equivalent that comparable to natural cells adhered on such patterns. A GUV adherent to a crossbow pattern has only one mirror symmetry axis, cutting it vertically. The pattern could thus give a geometric cue to induce a front-back polarization that is observed in living cells on micropattern with this shape. Cross pattern on the other hand were chosen as a pattern with a similar structure that lacks such difference between front and back. Additionally, various sizes of patterns and GUVs were adhered to demonstrate the capabilities of micropattern to accommodate a wide range of GUV sizes and shapes in a similar fashion as used for the controlled polarization of living cells.

A straightforward method to adhere and deform vesicles was established, that allows for the controlled adhesion and deformation of GUVs on arbitrary pattern in subsequent experiments.

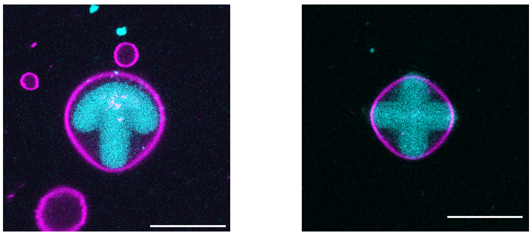

(a) 10 µm crossbow **(b)** 10 µm cross

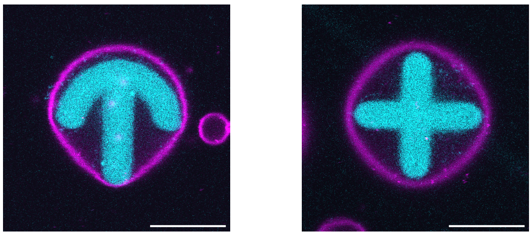

(c) 15 µm crossbow **(d)** 15 µm cross

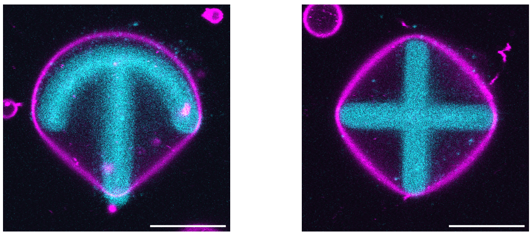

(e) 20 µm crossbow **(f)** 20 µm cross

Figure 3.7: GUVs can be adhered and deformed on various pattern shapes and sizes. The pattern (cyan) is shown at the plane of highest intensity. The GUV membrane (magenta) is shown 2 µm above the streptavidin pattern. Micropatterning provides a valuable tool in synthetic cell research for the deformation of GUVs. Scale bar is 10 µm. The Data in this Figure was obtained in collaboration with Charlotte R. Doll and is adapted from Fink et al.[29].

3.2.2 Quantification of GUV deformation on line micropatterns

Following the establishment of adhesion and deformation of GUVs on micropatterned surfaces, I set out to employ the setup to introduce polarity into GUVs using these geometrical cues. The next step was to quantify the deformation of adherent GUVs to gain deeper insights into the capabilities in this system, as well as the critical parameters. To this end the patterns were restricted to line shapes with dimensions of 15 µm in length and 2 µm width, employed during the patterning procedure (see Figure 2.2). This simplification to one pattern size should facilitate the quantitative description of the deformation, as it is published in Fink. et. al.[29]. It further allowed to mitigate problems in the analysis regarding the quantification of protrusions, as shown in Figure 3.6. The work presented in this chapter has been made in collaboration with Charlotte R. Doll, who conducted her bachelor thesis in physics at Heidelberg University under my supervision.

To evaluate the patterns, the fluorescence intensity of the immobilized streptavidin is plotted along and across the line pattern, shown in Figure 3.8. The average length of the lines was measured to be 17.8 ± 1.6 µm, and the line width 4.6 ± 1.5 µm (Values calculated from 6 lines from 2 independent experiments, given as mean ± SD). When interpreting the results, it should thus be kept in mind that the pattern are slightly wider and longer than the 15x2 µm large template used for the pattern creation. This can happen due to non perfect focussing or liquid remainings at the surface of the coverslip, as well as stray light from high laser intensities.

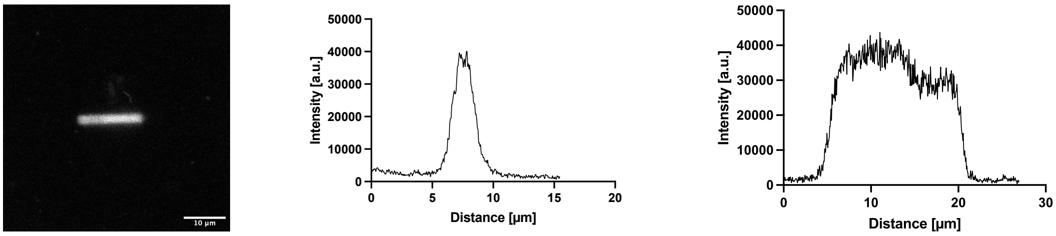

(a) 15x2 µm line pattern **(b)** Crossection through the line **(c)** Crossection along the line

Figure 3.8: Representative intensity plots of a line micropattern, patterned with a size of 15x2 µm, as shown in the tamplete in figure 2.2. a confocal image of a line functionalized with streptavidin is shown in **a**. The resulting line-width is wider that 2 µm, as it can be seen in b, with a width of around 5 µm. The line length, shown in c is also slightly longer than the patterned length of 15 µm. The scale bar is 10 µm

As it can be seen in figure 3.5, GUV deformation is strongly dependent on the distance to the surface. To account for that, the aspect ratio of the GUV membrane was measured consistently 2 µm above the surface slice, which in return was defined as the z-slice, where the streptavidin signal from the pattern had the highest intensity.

By measuring the length l of the major and minor axis, the aspect ratio of GUVs can be calculated in 2 dimensions as

$$\text{Aspect Ratio} = \frac{l_{\text{major axis}}}{l_{\text{minor axis}}}. \tag{3.1}$$

The major axis is the long axis of a deformed GUV, the minor axis the axis orthogonal to the major axis, as defined in figure 3.9**a**. The results are plotted in figure 3.9**b** against the guv major axis size. An aspect ratio of one would be the shape of a circle, where the length of the major axis is identical to the length of the minor axis. Larger aspect ratios on the other hand indicate stronger deformations. The major axis of the GUV generally aligns with the micropatterned line and is measured along the line in all cases. Values above one indicate a vesicle elongated along the line Thus, values below one would indicate a deformation, where the long axis of the GUV would not align with the micropatterned surface. Such a case was not observed in the here presented experiments. A strong dependence of the deformation on the GUV size can be observed in Figure 3.9**b**, with GUVs with sizes from 10 - 20 µm showing the largest aspect ratios. GUV size and the length of the major axis are used interchangeably. GUVs with major axis sizes from 10-15 µm and 15-20 µm show mean aspect ratios of 1.49 ± 0.21 and 1.51 ± 0.17 respectively. GUVs with a size of 5-10 µm show a significantly lower deformation, with a mean aspect ratio of 1.13 ± 0.10. The lower deformation in comparison to larger GUVs is attributed to the fact that small GUVs might not sense the asymmetry between the patterned and unpatterned parts of the surface, as their contact area width is limited by the GUV size, and not the line width. Thus, for a small GUV that has a similar sized adhesion patch as the pattern width with a size of 4.6 ± 1.5 µm, there there is no restriction in adhesion in any direction, and it is consequently not being deformed upon adhesion (see pattern shown in Figure 3.8). For GUVs larger than 20 µm, the deformation is reduced, when compared to the group in the range of 10-15 µm. GUVs with sizes in the range of 20-25 µm show an average aspect ratio of 1.33 ± 0.10. For GUVs that are much larger than the pattern, the aspect ratio gets even closer to one, indicating more circular shape, with an average aspect ratio of 1.02 ± 0.04 for GUVs in the size range from 25-30 µm. The deforming effect of micropatterned adhesive lines is reduced, when the GUV size is much larger than the pattern size. This can be explained since the pattern size becomes small, when compared to the GUV size, and with this the pattern shape does not have a deforming effect on large vesicles. In the most extreme case, it would behave as a point-like adhesion patch on a very large GUV. For comparison, free floating GUVs had a mean aspect ratio of 1.045 ± 0.02, yielding almost the same deformation as large GUVs in the size range from 25-30 µm.

It was shown, that the deformation of GUVs on micropatterns is size-dependent, where GUVs much smaller and larger than the micropattern do adhere, but are not deformed. It can therefore be summarized, that the GUV has to be similar in size as the micropattern to be deformed efficiently.

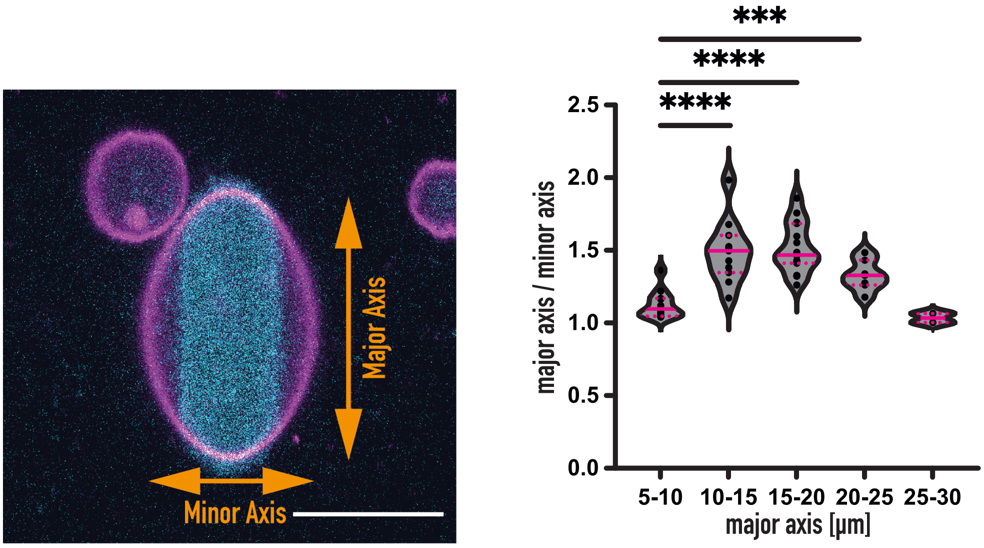

(**a**) Definition of major and minor axis.

(**b**) Quantification of GUV deformation on line shaped micropatterns

Figure 3.9: In (**a**), the definition of major and minor axis is shown. The pattern is shown in cyan at the surface. the membrane in magenta is shown 2 µm above the pattern. Scale bar is 10 µm. In (**b**), GUV deformation was measured by calculating the ratio of major to minor axis and is shown in dependence of the major axis size. It is evident that the GUV size is an important variable in GUV deformation, with the strongest deformation observed for GUVs with a major axis size ranging from 15 - 20µm and 10-15 µm. 47 GUVs from 4 independent experiments were analyzed. The median value is indicated by a solid line, the dotted lines indicate the SD. All significant p-values compared to the 5-10 µm group are denoted by **** $p < 0.0001$ and *** $p < 0.001$. The Figure was adapted from Fink. et. al.[29].

3.3 Actin bundle organization can be driven by geometrical cues

Actin is a major cytoskeletal protein in eukaryotic cells. Polarity in natural cells is often associated with changes in actin cytoskeleton organization and can be influenced in conjunction by adhesion to micropatterned surfaces[128]. One striking feature in mesenchymal cell migration are actin stress fibers, which are large bundles of actin filaments that orientate along the axis of migration[45]. Determining the direct effect of compartment deformation on bundled actin filaments in GUVs might indicate, whether this is sufficient to recreate structures with a similar orientation as found in migrating cells. I thus reconstituted actin bundles in deformed GUVs and examined their orientation. For actin bundling, fascin was used, a bundling protein that generates parallel actin bundles[131].

3.3.1 Actin labelling and bundling in GUVs with fascin

In oder to visualize actin filaments in a fluorescence microscope, it has to be labeled with a dye. In *in-vitro* studies with actin, a mixture of labeled, and non-labeled actin monomers is often used, as it allows efficient labelling of all actin structures with minimal effects on dynamics[80]. One side-effect though is the high background signal originating from the labeled monomers in solution. Changes in actin dynamics that stem from alternative labeling methods are negligible in the experiments presented in this work, since I am mainly interested in actin bundle organization, where actin bundles are treated as static structures. An often used dye for labeling actin structures in living cells is SIR-Actin[132]. In Figure 3.10 one can see a GUV prepared with a mixture of unlabeled and 10 % Atto488 labeled actin monomers with the filaments additionally stained using SIR-Actin to compare the two methods. One can see the high background of the actin monomers in Figure 3.10**b**. SIR-Actin only labels filamentous actin and not the monomers and shows thus polymerized actin structures significantly clearer (Figure 3.10**c**).

One alternative to SIR-Actin is the staining with labeled phalloidin. The main drawback is that phalloidin is not membrane permeable and would thus have to be applied directly to the inside buffer. SIR-Actin on the other side was simply added to the outside solution after the GUV formation. Phalloidin too stabilises F-actin, and might thus lead to increased actin polymerization during the mixing of the inside buffer, even when the components were kept and mixed on ice. Therefore, SIR-Actin was chosen in the subsequent experiments to label actin filaments, as has the advantage that it can be added after GUV formation from the outside, and thus only affects actin polymerization after GUV formation

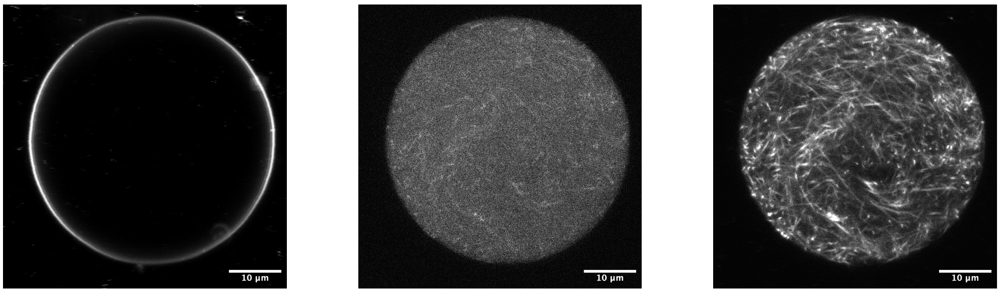

(a) GUV membrane **(b)** Labeled actin monomers **(c)** SIR-Actin stained filaments

Figure 3.10: Comparison of actin filaments in a GUV (membrane labeled with LissRhod **(a)**). Actin monomers labeled with Atto488 are depicted in **(b)**. As a comparison, actin was additionally labeled with SIR-Actin, shown in **c**. Since SIR-Actin labels filaments, but not the monomeric actin, the polymerized structures are visualized much clearer. Scale bar is 10 µm, $C_{\text{Actin}} = 10$ µM

For bundling actin filaments the actin bundler fascin was used., that creates long, straight actin bundles *in vitro*. In Figure 3.11, a comparison of an actin filled GUV with and without fascin is shown. While in Figure 3.11**a**, it can be seen that the fluorescence signal of actin is not homogenous, it is difficult to make out single actin filaments. In Figure 3.11**b** the bundles obtained by the interaction of actin filaments with fascin can be clearly seen. One should also note, that the persistence length of the bundles is higher than of single filaments, which should make them more susceptible to organisation by changes in the confinement geometry[133].

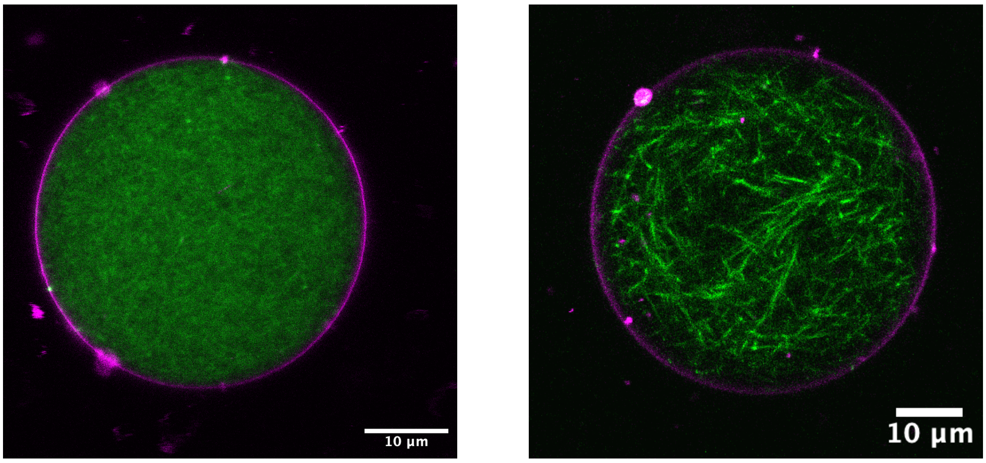

(a) GUV without Fascin **(b)** GUV with Fascin

Figure 3.11: Comparison of actin filaments (green) in GUVs with **(b)** and without **(a)** fascin. The membrane is shown in magenta. $C_{\text{Actin}} = 10$ µM, $C_{\text{Fascin}} = 1$ µM

3.3.2 Actin orientation in deformed GUVs

Following the establishment of GUV deformation actin bundling and labeling, the modules were integrated to investigate the effects of deformation on actin network organization. The work shown in this chapter was made in collaboration with Charlotte R. Doll, who conducted her bachelor thesis in physics at Heidelberg University under my supervision. GUVs in this section were prepared using the emulsion transfer method with the GUV composition found in Table 2.5 and the inner buffer composition shown in Table 2.13 with 5 µM actin, yielding GUVs with actin that is bundled by fascin.

To study actin network organization, line patterns as well as crossbow and, as a more symmetrical alternative, cross patterns were employed to include shapes more prevalent in cell-studies than lines. I kept the pattern size restricted in all cases to 15 µm, with a line width of 2 µm, to ensure comparability between the different micropatterned shapes.

In Figure 3.12 actin and fascin filled GUVs are shown on 15 µm wide patterns of various shapes. A circular pattern was additionally included to the aforementioned patterns . As done before, the GUV membrane, as well as the actin bundles are shown 2 µm above the micropatterned surface. The micropattern has been omitted for clarity in the images. The outline of the actin bundle filled, deformed GUVs does not appear different, compared to empty, deformed GUVs in Figure 3.7 and 3.9**a**.

To examine actin bundle orientation, images were analyzed using SOAX to trace the actin bundles, and thus allows to extract directionality of the bundles[134]. The workflow is exemplarily shown in figure 3.14 and 3.13. The GUVs were analyzed 2 µm above the surface to stay consistent with the analysis of the deformation described before. First, a gaussian blur was applied to the actin channel of the image, to improve filament detection, as shown in figure 3.13. If the image is not blurred beforehand, the filament detection algorithm mistakes a lot of noise wrongly as filament. This can be seen in Figure 3.13**b**. When a gaussian blur is applied, the traced filaments (see Figure 3.13**c**) mirror the bundles observed by eye in figure 3.13**a** well. Next, I wanted to determine the filament angle. To this end, we fitted a line to each of the detected actin bundles, since we expect straight filament bundles formed by the interaction of actin with fascin. The filament angle is then given by:

$$\theta = \cos^{-1}\left(\frac{\vec{u}\cdot\vec{v}}{||\vec{u}||\cdot||\vec{v}||}\right) \tag{3.2}$$

using the y axis as the reference vector.

I further only consider the absolute value of θ, as all patterns used are mirror symmetric with regards to the images y axis. The symmetry of the patterned surface together with

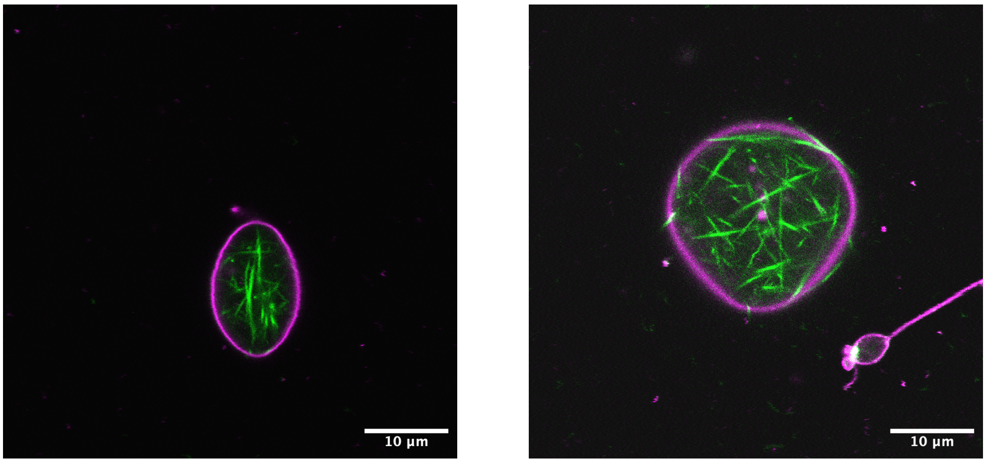

(a) GUV on line pattern **(b)** GUV on crossbow pattern

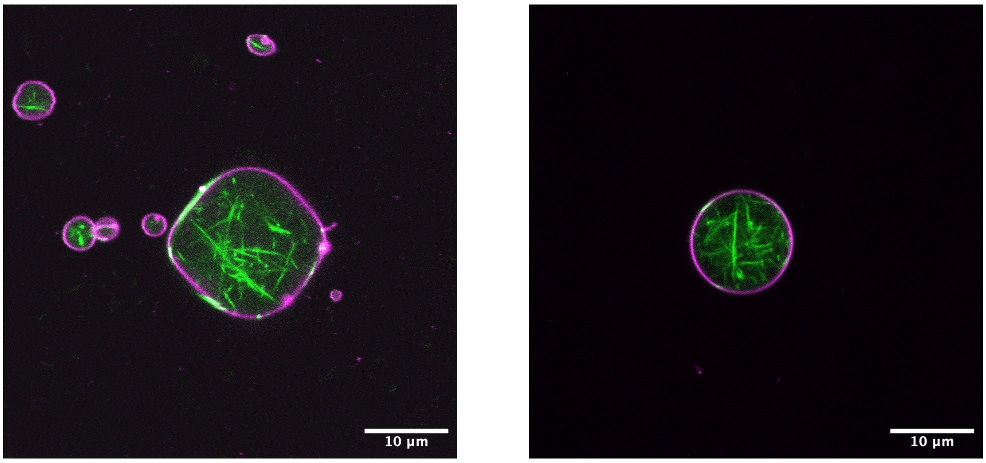

(c) GUV on cross pattern **(d)** GUV on circular pattern

Figure 3.12: Comparison of actin bundles with fascin in adherent and deformed GUVs. Actin labeled with SIR-Actin is shown in green, the GUV membrane, labeled with Atto488 is shown in magenta. Both actin and the membrane are shown 2 µm above the micropatterned surface. In the GUV adhering on the line shaped pattern, the actin can be seen aligning along the major axis. The patterns have a size of 15 µm, the scale bar is 10 µm, $C_{\text{Actin}} = 5$ µM, $C_{\text{Fascin}} = 0.5$ µM

the adherent GUV is considered. The symmetry groups are then a $C_{\infty v}$ symmetry for GUVs adhering to circular pattern, C_{2v} symmetry for GUVs adhering to line pattern, C_{4v} symmetry for GUVs adhering to cross pattern and D_1 for crossbows with a single mirror axis, that is shared by all pattern utilized in the experiments in this work.

When filament angels are plotted, the angel of the filament is compared to the y-axis. Although actin filaments do have a directionality due to their + and −ends, and fascin bundles actin in a parallel manner, the filament-polarity cannot be determined from the confocal images. This reduces the range of filament angles from 360 to 180°. Further, all pattern employed in the experiments are orientated to share at least one mirror axis along the y-axis, stemming from the D_1 symmetry for crossbows. This further reduces

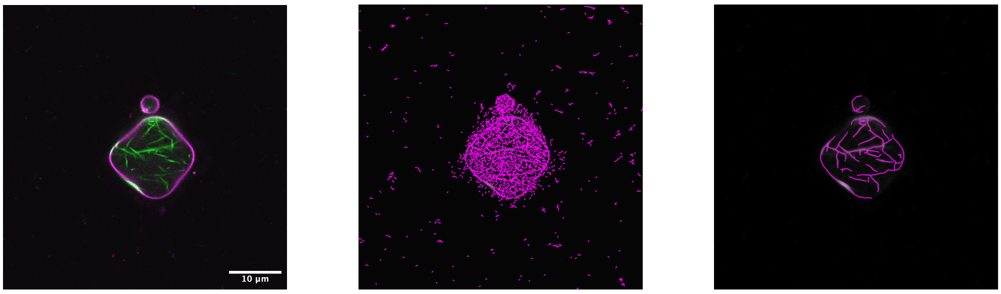

(a) Sample GUV used for analysis.

(b) Actin filament detection using SOAX without gaussian blur

(c) Actin filament detection using SOAX after applying a gaussian blur

Figure 3.13: Using SOAX to detect actin bundles. In **(a)**, a confocal image of a GUV is shown. The membrane is shown in magenta, actin bundles in green. For the analysis of bundles, first a gaussian blur is applied onto the confocal image of the actin filaments **(c)**. Otherwise actin bundles were not detected reliably **(b)**. Scale bar is 10 µm

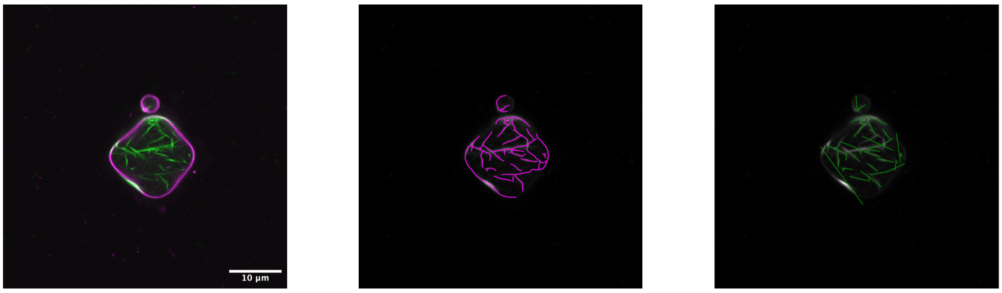

(a) GUV used in Figure 3.13.

(b) Actin bundle detection using SOAX

(c) SOAX output after applying principal component analysis

Figure 3.14: Exemplary SOAX workflow. In **a**, the same GUV as in Figure 3.13 is shown. The membrane is shown in magenta, the actin bundles in green. For the analysis of actin bundles, first a gaussian blur is applied onto the confocal channel of the actin bundles. Then, the SOAX algorithm is applied to trace the actin bundles. Principal component analysis it then used, to fit a line onto the bundles, and with that calculate the bundle angle. Images were analyzed using the same parameters as described in Fink et al.[29]. Scale bar is 10 µm

the relevant range of angles from 180° to 90°. The results from this analysis on circle, line, cross and crossbow patttern are shown in Figure 3.15.

The circular pattern was used as a highly symmetric reference, as actin bundles are not expected show any preference in their angular orientation. The GUV adhered to the pattern has C_∞ symmetry and bundle distribution is expected to assume the same symmetry as the underlying pattern. GUVs on line-shaped pattern show an asymmetry in their angular distributions. One can see, that the filaments tend to align with the major axis of the deformed vesicle, indicated by the increase of actin bundles with 90° filament angles, where over 50 % of all detected bundles have a filament angle of $>$ 75°(Figure 3.15) . This proves, that actin bundle orientation can be guided by deformation in synthetic cells. The bundles inside of GUVs adhering to cross and crossbow shaped micropatterns do not show any discernible preference in angular orientation, contrary to bundles on line shaped micropatterns. A possible explanation for this is, that the deformation in GUVs on line-shaped patterns is more pronounced, than on cross and crossbow patterns. When looking at the GUVs shown in Figure 3.12, the oval shape of the GUV adhering on the line pattern is very prominent, compared to the GUV adhering on the crossbow or on the cross pattern, whose outline resembles a circular shape more. This might lead to stronger effects of the deformation onto the actin angular orientation.

To understand the actin bundle organization in the various shaped GUVs better, we implemented a simulation in python. For this, we assume the actin bundles behave as straight rods. Further, we propose, that the membrane is not affected by actin bundles and bundles are not allowed to pass through the membrane. The assumption, that the GUV membrane is unaffected by the actin bundles, is backed up by comparison of the membrane shape of the deformed vesicles with (Figure 3.12), and without actin bundles, as presented earlier in Figure 3.7 and 3.9a. When actin bundles are encapsulated in a spherical GUV and the actin bundles are shorter than the GUV size, the orientation is expected to be random with every orientation being equally likely. For bundles larger than the GUV size, there is no optimal orientation where the bundles don't touch the membrane and this case is thus ignored within our simple framework. This gives raise to a straightforward model that describes actin bundle organization inside of a non-deformable confinement.

When a GUV is deformed, for example from a spherical to an oval shape by adhesion to a stripe, it is anticipated that the actin bundles will align along the major axis. This alignment occurs because the bundles avoid the membrane, which prohibits filament crossing. A Python script was employed to simulate this phenomenon using an arbitrary GUV outline and filaments of specified lengths, facilitating investigation into the influence of filament length and GUV morphology. The resulting simulated filament distributions for a bundle

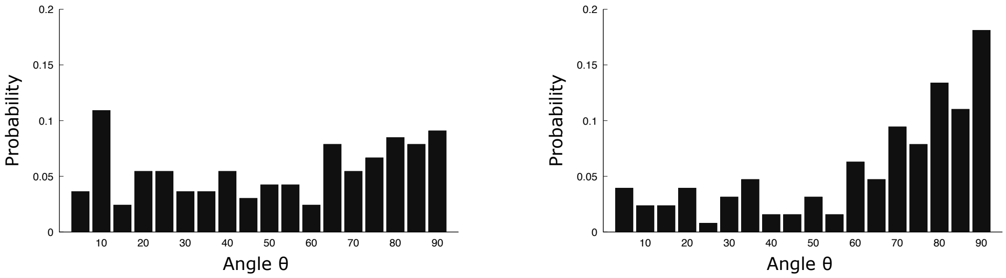

(a) GUV adhering to a circle

(b) GUV adhering to a line

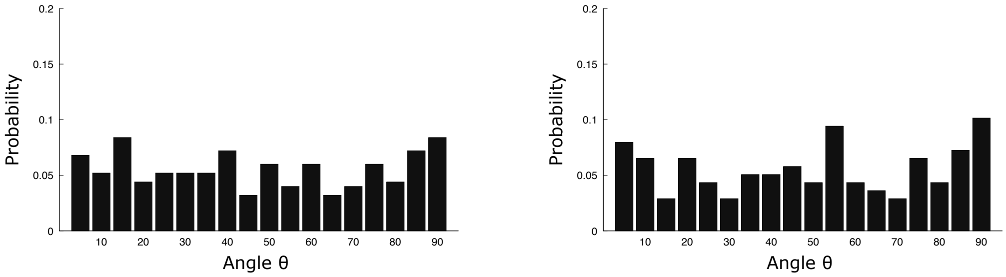

(c) GUV adhering to a crossbow

(d) GUV adhering to a cross

Figure 3.15: Measured filament angles (θ, in degree) in various GUV shapes. One can see the asymmetry of the filament angles in the GUVs adherent onto line shaped pattern. Other patterns do not show any evident asymmetry in their filament distributions. For the circular pattterns 6, line 17, cross 12, and crossow actin filament angles from 13 GUVs were analyzed. The data has been published in Fink et al.[29].

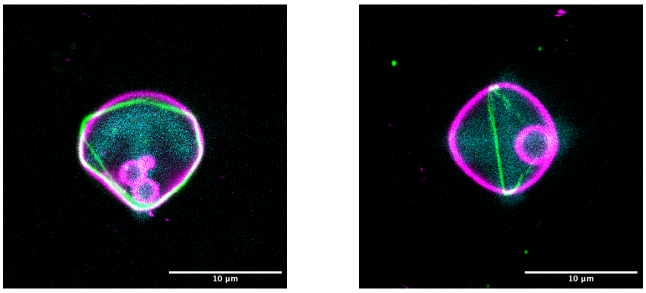

(a) GUV adhering to a 10 µm crossbow

(b) GUV adhering to a 10 µm cross

Figure 3.16: Two representative images of actin bundles in GUVs adhering to 10 µm long micropattern, that are smaller than the 15 µm patterns used for the quantifications. A maximum-z projection of the actin bundles is shown (green). The membrane (magenta) is shown 2 µm above the surface, the micropattern is shown at the surface slice in cyan. In **a**, one can see the actin bundles localizing along the membrane since their length is larger than the confinement. Due to this buckling of the bundles is seen in the image, indicating the assumption that actin bundles are straight rods is not valid for actin bundles in small GUVs. In **b**, an actin filament is oriented along the cross pattern, but also here the filament buckles at the ends, making the assumption of straight filaments invalid. The data has been published in Fink et al.[29]. Scale bar 10 µm.

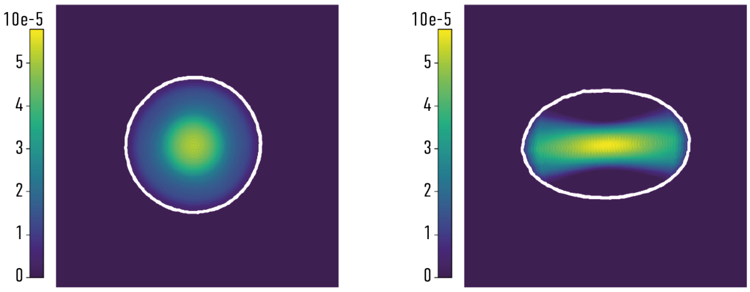

(a) GUV adhering to a circle **(b)** GUV adhering to a line

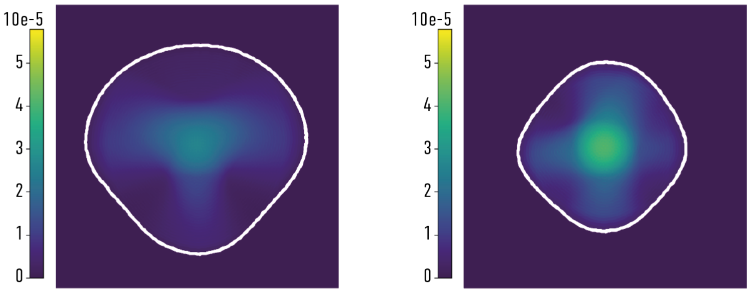

(c) GUV adhering to a crossbow **(d)** GUV adhering to a cross

Figure 3.17: Simulated filament probability densities in various GUV shapes, with a filament length of 0.9x major axis length. The GUV shape used is shown in magenta. Figure adapted with permission from Fink et al[29].

length of 0.9x major axis length inside of the here employed GUV shapes can then seen in figure 3.17. For the shape, experimental GUV outlines were used and are plotted in white.

The angular filament distributions were calculated from the theoretical results for these confinements and are shown in Figure 3.18. Actin bundle lengths are given in multiples of the major axis length, to simplify comparison between the different conditions and to accomodate slight variations in GUV size. For the circular GUV outline, no preference in the angular orientation is observed in the simulations, as expected. On the line pattern, all shown filament sizes display a strong asymmetry in their angular distributions (Figure 3.18b). In the case of the crossbow pattern, a strong asymmetry in the angular distribution is observed only when the bundle length is exceeding 0.85x major axis length (Figure 3.18c)). On the cross pattern the same behaviour can be seen, although the probability density is even lower at the maximum. (Figure 3.18d))

I additionally adhered GUVs on small cross and crossbow pattern with a size of 10 µm (Figure 3.16). A max-z projection of the actin bundles inside GUVs on crossbow (Figure 3.16a) and cross (Figure 3.16b) micropattern is shown. The actin bundles can be observed to buckle when touching the membrane, making the assumption made earlier, that actin bundles can be treated as straight rods invalid. Nevertheless, in the image of the GUV adhering to the crossbow pattern (Figure 3.16**a**), the actin network appears to be mirror

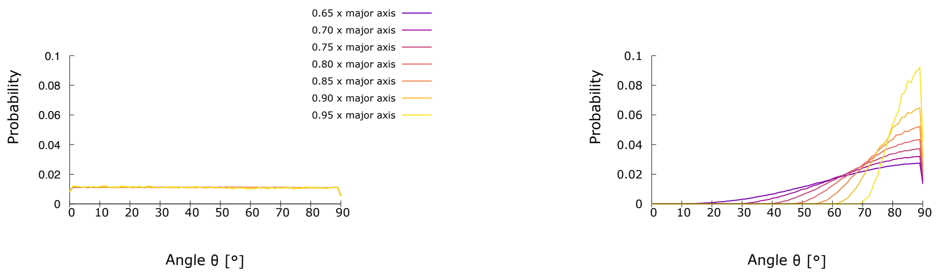

(a) GUV adhering to a circle **(b)** GUV adhering to a line

(c) GUV adhering to a crossbow **(d)** GUV adhering to a cross

Figure 3.18: Simulated filament angles in various GUV shapes, in dependence of bundle length in units of the length of the major axis of the GUV. Figure adapted with permission from Fink et al[29]

symmetric, reflecting the symmetry of the deformed GUV.

The similarities of the results obtained in the simulations, shown in figure 3.18 and the ones obtained experimentally on GUVs adhered to micropattern, as seen in figure 3.15 hint to a good description of the underlying mechanism. Although GUVs adhering to micropattern are three, and not two dimensional systems, as assumed in the simulations, the results in two dimensions still describe the observed data well, and could be extended to three dimensions. For GUVs on line-shaped micropattern the asymmetry in the angular distribution was visible, even for shorter actin bundle lengths. This was also the only shape, on which an asymmetry was detected experimentally. For the other patterns, the cross and the crossbow no asymmetry in the distributions was found. This is explained by the simulations, as an asymmetry in the angular distributions was only found for actin bundles of 0.90x major axis length and longer. In the experiments, we expect actin filaments of various sizes and thus potentially hide the asymmetry that long filaments display.

3.3.3 Actin organization in deformed GUVs in the presence of dextran as a crowding agent

Cells are highly crowded environments that are packed densely with proteins, RNA, and various macromolecules. Therefore, employing predominantly empty vesicles can be anticipated to inadequately mimic a biological system. Together with Sunnatullo Fazliev, who did his master thesis under my supervision, I tried to extend the system of actin bundles within deformed compartments to densely crowded environments, where actin bundles self-organize along the membrane resembling an actin-cortex like arrangement. The presence of crowders bundles actin filaments, which increases their persistence length due to depletion effects. This causes the bundles to localize at the GUV membrane, as their persistence-length becomes far greater than the size of the vesicle[135,136]. GUVs in this section were prepared using the emulsion transfer method with GUV composition found in Table 2.5 with the inner buffer composition shown in Table 2.14. The organization of actin bundles along the membrane in the presence of dextran can be seen in the image 3.19. This effect gives us easy access to cortex-like actin structures, from here on called synthetic actin cortices, without the need to directly bind actin to the GUV membrane. It was shown before, that in natural cells modulating the binding distance of the cortex using synthetic linkers to the cell membrane profoundly affects the mechanical properties of the cell[137]. One should note though, that cells do not only have actin filaments localized at their membrane, as expected from the experiments with actin under crowded conditions in GUVs, but also many actin structures spanning the cell, like stress fibers. This is due to the high level of regulation by various proteins, as the structures are all actin based, but incredibly diverse in their shape and function. This functionality, that originates from actin modulating proteins is not captured in this in-equilibrium system, but might be a starting point to add further complexity. I want to utilize the deformation imposed by the pattern in a more efficient manner, as the effects of deformation are expected to be strongest at the membrane, that is directly affected by the adhesive micropattern.

I adhered GUVs with such synthetic actin cortices to micropatterned surfaces, using the interaction of biotin and streptavidin as described earlier. When adhered to micropatterns, actin bundles seem to organize at the adhesion site of the vesicle, creating spiral structures. We assume, that they avoid transitioning from the non-adhered to the adhered region of the GUV (see magenta arrows in Figure 3.20**b**). The line pattern outline is indicated by a magenta rectangle in Figure 3.20**a**. This leads to a spiraling actin-pattern forming close to the adhesion site, parallel to the surface. A comparison between GUVs with synthetic actin cortices adhering to various patterns is shown in Figure 3.21. All adherent vesicles demonstrate the actin bundles parallel to the pattern around the adhesion site. The images

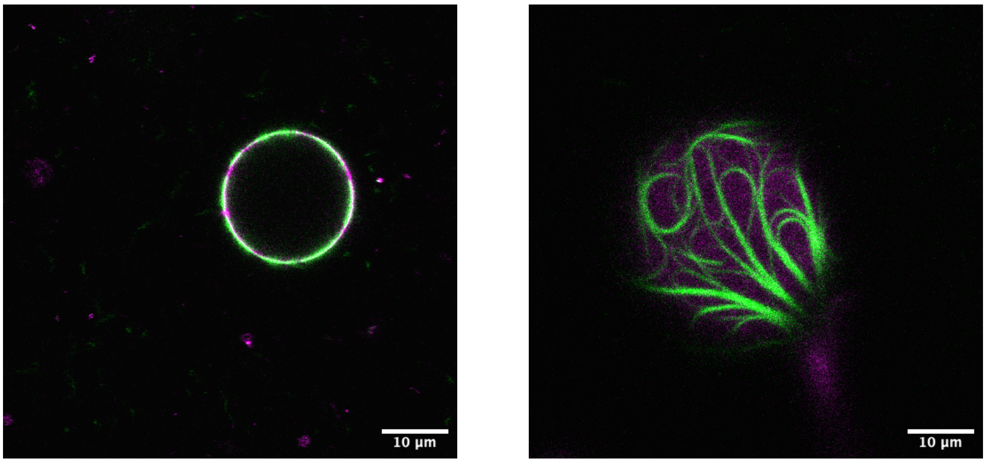

(a) Confocal image through the center

(b) Confocal image at the top

Figure 3.19: Image of free floating GUVs with actin bundles (green) inside a free floating GUV and dextran with a MW=100 kDa. One can see actin bundles accumulating at the membrane (magenta), while the lumen of the vesicles is void of bundles. The actin bundles are long and create complex patterns at the membrane of the GUV. Scale bar is 10 µm

were created using a python script to plot each slice of the z-stack in a different color depending on the height, yielding a height coded maximum z-projection. Additionally, a free floating GUV, that shows vortices in the actin bundles which are not localized to any particular region of the spherical GUV is depicted. In the GUV adhering on the line pattern, one can see actin bundles avoiding transitioning from the adherent to the free part of the GUV, leading to the swirling pattern that gets created around the adhesion site. Similar observations can be made for the other patterned shapes, as the bundles close to the adhesion site depicted in red seem to exhibit a circumferential orientation around the pattern, which emerges as a actin-poor region in the GUV. It is also evident, that the general behavior appears to be independent of the pattern shape, with the common part being the adhesion to the surface. In the scope of my goal to induce polarity, this is not desired, as the objective is to create asymmetry in the actin distribution, induced by the pattern the GUV is adhering to.

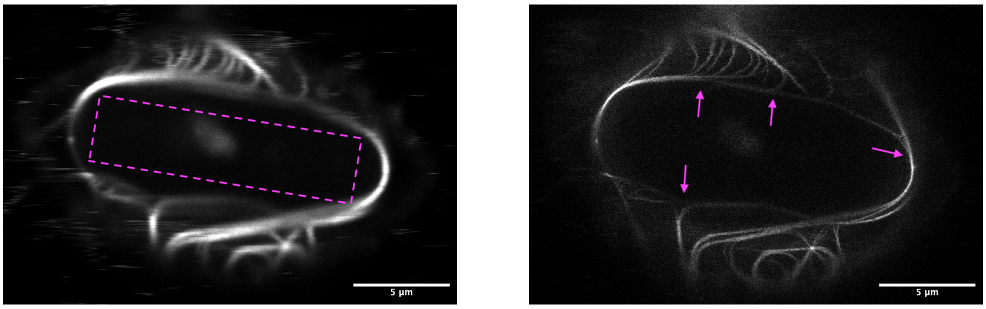

(a) Confocal image of the synthetic actin cortex

(b) STED image of the synthetic actin cortex

Figure 3.20: Confocal and STED image of the synthetic actin cortex inside a GUV adhering to a line shaped micropattern. On the confocal image **(a)**, the pattern outline is indicated by a magenta rectangle. In the STED image **(b)**, one can see actin filaments avoiding the sharp transition area at the adhesion site and instead bend along the surface, as indicated by the magenta arrows. Scale bar is 5 µm.

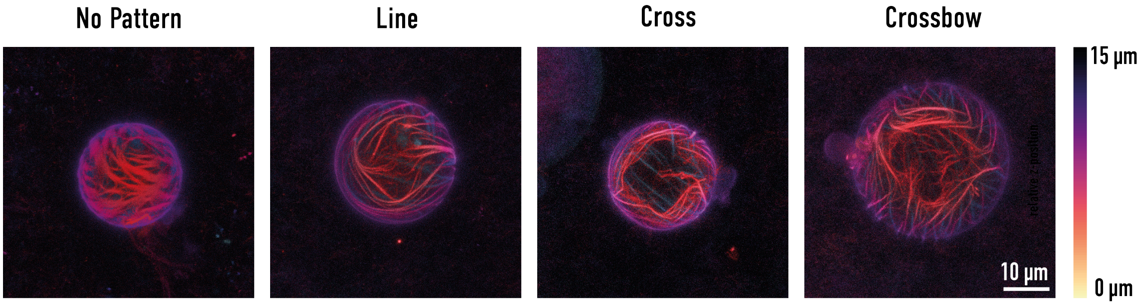

Figure 3.21: Height coded z-projection of synthetic actin cortices in GUVs adhering to various pattern. The adherent part of the GUVs shows a low actin density, as most filaments seem to avoid the adhered region of the GUV. Scale bar is 10 µm.

3.3.4 GUV deformation is inhibited by cortex-like actin structures

While observing that synthetic actin cortices in adherent GUVs were affected by the underlying micropattern, the deformation appeared to be inhibited in these vesicles. The data of GUVs on micropatterns in this section has been acquired and analyzed together with Sunnatullo Fazliev during his Master thesis under my supervision. GUVs in this section were prepared using the emulsion transfer method with the GUV composition found in Table 2.5 and the inner buffer composition shown in Table 2.14. To better understand the effect of synthetic actin cortices on the deformability of GUVs, we used the same assay to quantify deformation as described in section 3.2.2, where GUVs were adhered to 15 µm long line shaped micropatterns. The deformation was quantified again, using the aspect ratio 2 µm above the patterned surface of GUVs in the size range of 15-20 µm. The results are presented in figure 3.22. On one hand the dextran concentration was kept constant at 11.2%, which was the highest concentration that could be efficiently encapsulated into

GUVs in our experiments. When no actin is present, the mean deformation is 1.41 ± 0.04, which is comparable to the deformation of empty GUVs in the same size-range with a mean of 1.51 ± 0.17 (compare to Figure 3.9). This suggests dextran alone does not have any effect on the GUV deformation. GUVs encapsulating only 2.5 µM actin without crowder exhibit an aspect ratio of 1.45 ± 0.08 and thus no significant change from the conditions when only crowders are added, or GUVs were empty (Figure 3.22). In summary, each component alone does not affect deformability of GUVs. We then set out to quantify the deformation when both components were encapsulated together, as the crowder causes the actin to allocate at the GUV membrane. Thus, we assume the amount of dextran to influence the amount of actin localized at the membrane. Additionally, the concentration of actin was varied, as it is expected that GUVs get less deformable when more actin is encapsulated, stabilizing the membrane against deformation. Both effects are visible in figure 3.22. When the dextran concentration is kept constant at 11.2 % and the actin concentration is increased, the deformability decreases until it reaches a minimum at an actin concentration of 2.5 µM. I assume, that this is the direct effect of increasing the amount of actin associated to the membrane, and thus stabilizing the GUV and hindering deformation. From there a small increase in the deformability is noted when the actin concentration is further raised to 5 µM. I hypothesize that this phenomenon may arise from a sorting effect, where the increased GUV stiffness decreases the likelihood of a GUV to adhere to a pattern, and thus GUVs that are more deformable within a sample tend to adhere more. For experiments where the dextran concentration was changed, the actin concentration was fixed to 2.5 µM, as the deformability in GUVs with this actin concentration was lowest, with an aspect ratio of 1.19 ± 0.04. Similar to Figure 3.22a, where the actin concentration was varied, in Figure 3.22b, where the dextran concentration is changed, the deformation is highest, when no dextran is present. When the dextran concentration is increased the deformability decreases. We interpret the findings as indicating that crowding agents such as dextran exert a force that drives actin filaments toward the membrane and stabilizes it there against deformation. Since the effect is due to passive volume exclusion effects, we expect it to become more pronounced with higher crowder concentrations, as seen in figure 3.22b.

To further validate the results obtained by measuring the deformation on micropatterned line surfaces, we applied Real-Time Deformability Cytometry (RTDC) to the GUV samples encapsulating 11.2 % dextran with and without 2.5 µM actin. The RTDC measurements were performed in collaboration with Tobias Abele. RTDC allows for the analysis of a large part of the GUV population, in comparison to the microscopy based assays used before, that relied on less than 100 analyzed vesicles. The principle is to flow cells, or in my case GUVs through a narrow microfluidic channel with a diameter slightly larger

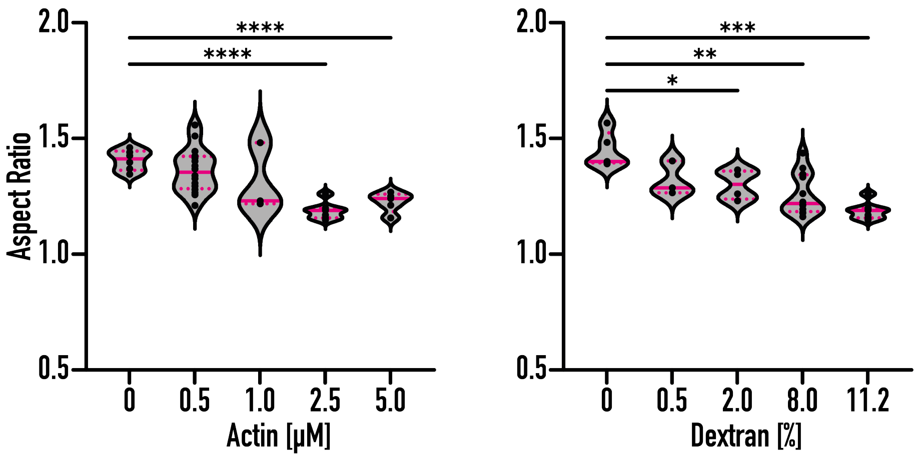

(a) GUV deformation with various actin concentrations at a constant dextran concentration of 11.2 %

(b) GUV deformation with various dextran concentrations at a constant actin concentration of 2.5 µM

Figure 3.22: Aspect ratios of GUVs in the size-range of 15 - 20 µm with synthetic actin cortices with various dextran and actin concentrations. In **a**, one can see the decrease in deformation of adherent GUVs with increasing actin concentration, indicating an increasing stiffness when more actin is present inside of the GUV. Similarily, when the actin concentration is kept constant and the Dextran concentration is increased, the deformation is lowered (**b**). A t-test with Welchs correction was used, p-values are *=0.016, **=0.0018, ***=0.0007 and ****=0.0001. 61 GUVs were analyzed.

than the GUVs measured. After entering the channel, the GUVs are deformed and a microscopy image is taken, as seen in Figure 3.23. One can see the GUVs assuming a bullet shape inside of the microfluidic channel. Then, the deformation was measured, defined as 1-circularity and plotted in dependence of the projected GUV area, using the software ShapeOut2[138].

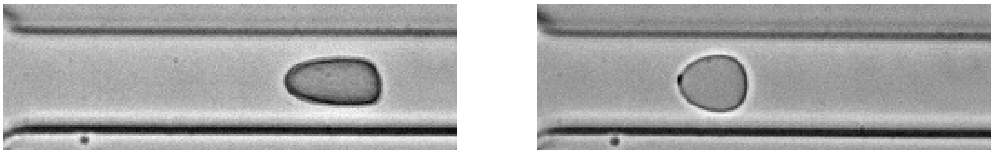

(a) GUV deformation without Actin.

(b) GUV deformation with 2.5 µM Actin.

Figure 3.23: Representative images of deformed GUVs during the RTDC measurement. GUVs in both samples had a Dextran concentration of 11.2 % .GUVs inside of the microfluidic channel assume a bullet shape. GUVs without actin are more deformed (a), than GUVs with actin (b).

The results obtained for vesicles with 11.2 % dextran with and without 2.5 µM actin are plotted in figure 3.24, as it were the conditions that showed the strongest differences in deformability in Figure 3.22. The aspect-ratio, here defined as in Otto et. al., as 1-circularity is plotted against the projected area of the GUV[139]. The aspect ratio for the samples without actin is 0.069 ± 0.041, the aspect ratio for the samples with actin was on average 0.066 ± 0.043. Although the difference in aspect ratio is small, it is significant with a p-value of 0.0097, due to the very high number of individual GUVs measured. Further, in the scatter plots (Figure 3.24), a strong shift in the point density toward less deformed GUVs, quantified by their aspect ratio is observed when the samples lacking actin are compared to the samples with actin. These results also prove, that the reduced deformability is not solely a result of the increased viscosity due to the presence of crowders. One should keep in mind, that encapsulation of actin and crowders into GUVs follows a probability distribution and the final concentration is not the same in each individual GUV[70]. Thus, a subset of GUVs is expected to not have both components encapsulated in sufficient concentrations together to exhibit a reduction in deformability, since it was established before, that GUV deformation is inhibited only when both, actin and crowders are present at sufficient concentrations.

Both assays together show the reduction of the deformability of GUVs when synthetic actin cortices are assembled at the GUV membrane. Further, it was shown, that both, crowders and actin need to be present together to result in an inhibition of the deformation. Actin therefore needs to be localized at the GUV membrane to affect deformability, as it allows for the stabilization of the membrane against deformation directly. In the future this could allow for synthetic cells that mimic the mechanical properties of natural cells more closely. This can further aid in interactions between natural and synthetic cells, as the mechanical properties play an important role in the signaling cascade of natural cells[140].

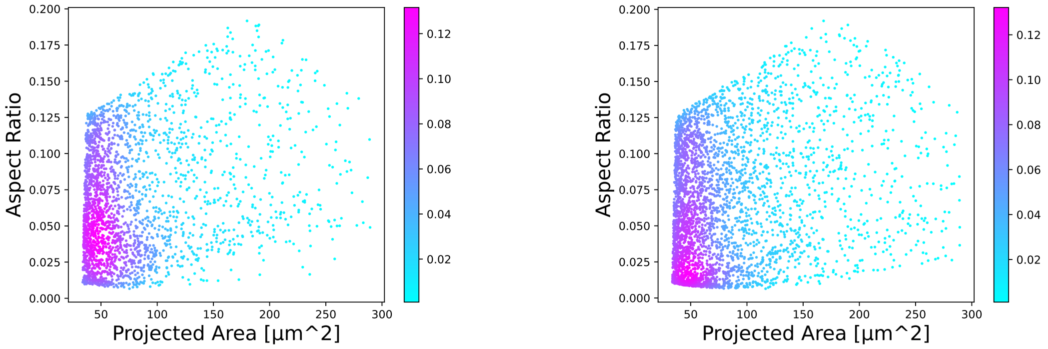

(a) GUV deformation without Actin

(b) GUV deformation with 2.5 µM Actin

Figure 3.24: Scatter plots for the RTDC measurements. The aspect ratio (1-circularity) is plotted against the projected area in µm^2 of the measured GUVs[139]. A higher event (GUV) density is indicated by a magenta colour3471, and 2457 GUVs from 4 independent experiments were analyzed with and without actin respectively.

3.4 Membrane phase separation in GUVs as model for cell polarity

GUVs are used as models for living cells and as a starting point in synthetic biology that provides a platform to engineer cell-like functionality from the bottom up. Furthermore, they enable the reverse engineering of cellular functions through methods distinct from those employed by natural cells to achieve similar behaviours.

Therefore, although macroscopic lipid phase separation into Ld and Lo phases is usually not found in living cells, it can provide a tool to organize molecules at the synthetic cell membrane in a spatially inhomogeneous way. Natural cells exhubut asymmetry in their lipid compositions, ranging from nm sized raft structures to heterogeneities found in the apical and basal membrane of epithelial cells[141]. It can be used as a scaffold for protein organization, by functionalizing one phase selectively with a protein, for example by utilizing the interaction between a Ni^{2+}-NTA lipid that localizes in one phase and binds a poly-histidine tagged protein[71]. In this section, I set out to control and understand domain localization as a response to geometrical cues provided by adhesive micropatterned surfaces, to in the future enable the controlled distribution of proteins at the synthetic cell membrane.

3.4.1 Optimizing the emulsion transfer method to generate phase separated GUVs

To obtain phase separated vesicles, electroformation or swelling based methods are often employed as they are known to create GUVs with a well-controlled lipid composition, that can incorporate various phospholipids and cholesterol[62,96,142]. Emulsion based method, like emulsion transfer, or cDICE need to be modified to allow for an efficient incorporation of cholesterol to achieve phase separation in GUVs[71,72]. Emulsion-based techniques, in contrast to methods such as electroformation, exhibit a high degree of versatility concerning the composition of buffers, as well as the incorporation of proteins.[143]. Hence, they can serve as a valuable tool, particularly to generate phase separated GUVs with various proteins encapsulated on the inside.

Dürre and Bausch presented an adapted protocol of cDICE, that allowed for the incorporation of cholesterol in sufficient amounts to obtain phase-separated vesicles[71].They further mapped the amounts of cholesterol dissolved in the oil phase to the amount of cholesterol expected to be in the GUV membrane, by comparing the GUV morphology with GUVs produced using the electroformation technique. Based on these findings, I adapted the

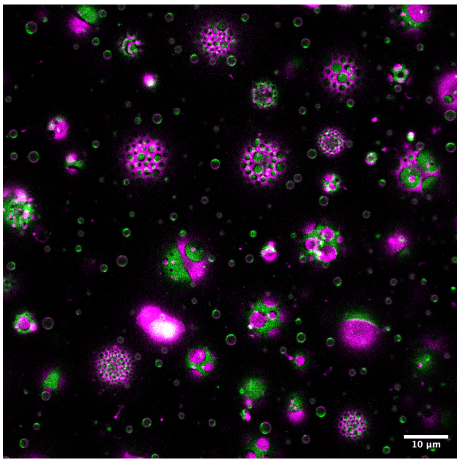

Figure 3.25: Representative confocal image of phase separated vesicles, using the optimized emulsion transfer method. Tf-chol, an Lo marker, is shown in green, Liss-Rhod, which partitions into the Ld-phase in magenta. The typical morphology of phase separated GUVs with lipid domains of various sizes can be seen. The Scale bar is 10 µm.

emulsion transfer protocol to allow for the generation of phase separated GUVs. The main changes in comparison to the standard protocol I utilized was the use of only silicone oil, instead of mineral oil, as well as the supply of high amounts of cholesterol[70].

Vesicles containing a mixture of equal amounts of DPPC and DOPC together with over 10 Mol% cholesterol are known to exhibit phase separation behaviour, with liquid domains at room temperature[144]. Thus, the incorporation of at least 10 Mol% cholesterol in the GUV membrane is needed to obtain liquid phase separated GUVs successfully. To visualize the two phases, LissRhodPE was used to stain the liquid disordered (Ld) phase, while top-fluor labeled cholesterol (Tf-chol) was used to show the liquid ordered (Lo) phase throughout the experimental images in this chapter.

The oil-phase, made up from mineral oil in the sections before, was exchanged fully to silicone oil for the emulsion transfer protocol employed in this section. It is anticipated that cholesterol will exhibit lower solubility in silicone oil compared to mineral oil, which should facilitate the partitioning of cholesterol from the oil phase into the GUV membrane during the GUV formation process. A partial exchange of mineral oil to silicone oil, or a mixture of both, as derived from experiments published with cDICE did not yield phase separated vesicles in the experiments I performed[71]. As a starting point, 60 Mol% cholesterol was dissolved into the oil phase, as used by Dürre and Bausch for the cDICE protocol[71]. A representative image of phase separated vesicles obtained with the modified emulsion transfer method is provided in Figure 3.25. The phase separation can be seen in the inhomogeneous color distribution throughout the GUV membrane, stemming from the different lipid domains within one GUV. The here described changes allowed to generate phase separated vesicles using the emulsion transfer method. In the next step, I set out to optimize the amount of cholesterol dissolved in the oil phase. The results are depicted in Figure 3.26. One can see, that with 40 Mol% cholesterol dissolved in the oil phase no phase separated vesicles are observed. Based on comparisons with phase diagrams of GUVs with DOPC, DPPC and cholesterol, GUVs with this membrane composition are expected be phase separated, reflecting the observation, that the lipid composition inside of the oil is not identical to the composition of the final GUV membrane. When the cholesterol amount is increased to 60 Mol%, a large part of GUVs starts to exhibit phase separation behavior, together with a high GUV yield. When the cholesterol concentration is further increased to 80 Mol%, almost all GUVs are phase separated, although yield is reduced compared to 60 Mol%. From there, I decided to use 80 Mol% cholesterol in the oil phase, to maximize the fraction of phase separated GUVs in the sample, as a decreased yield is not a concern when GUVs are adhered to micropatterns.

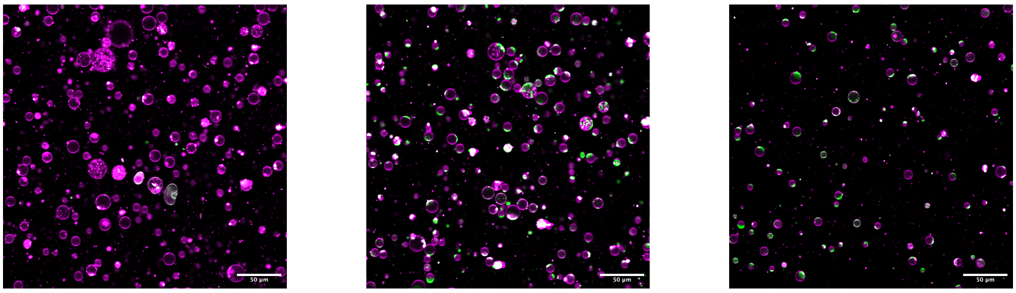

(a) 40 Mol% cholesterol **(b)** 60 Mol% cholesterol **(c)** 80 Mol% cholesterol

Figure 3.26: Phase separated vesicle production using the emulsion transfer protocol with silicone oil, and different amounts of cholesterol. The amount of cholesterol in the oil phase during the emulsion transfer method is indicated. The Lo phase is labeled with Tf-chol (green), while the Ld phase is stained using LissRhodPE (magenta). With 40 Mol% **(a)**, no phase separation is observed. When the cholesterol concentration is raised to 60 Mol% **(b)**, a large amount of phase separated vesicles is observed. With 80 Mol% almost all vesicles appear phase separated, although the total amount of vesicles seems to be lower. Scale bar is 5 µm.

In the next step, the phase separated GUVs needed to be functionalized with biotinylated lipids to allow for the adhesion to streptavidin coated micropatterns. This is achieved by adding the biotinylated lipid to the oil-phase, as presented before. In order to verify that the biotinylated lipid partitions into a single phase, it is visualized using fluorescently labeled streptavidin, that binds to the biotin in the membrane (Figure 3.27**c**). As it can be seen in Figure 3.27, the Biotin-PEG2K-DSPE localizes in the same phase as the Tf-chol, an Lo marker. This is to be expected, as Biotin-PEG2K-DSPE has a fully saturated hydrocarbon tail group (See Figure 1.4). The LissRhod-PE localized in the Ld phase, and the signal is thus low in the areas where the Tf-chol signal is high.

Based on protocols established for the cDICE method of GUV production, I have optimized the emulsion transfer to allow for the formation of phase separated vesicles, to later on utilize its advantages, like the ability to reconstitute proteins in various buffer conditions. I have further shown, that the incorporation of functional lipids into a specific phase, here Biotin-PEG2K-DSPE, is not affected by the adapted emulsion transfer protocol, and should be compatible with the usage of micropatterns to adhere the GUVs.

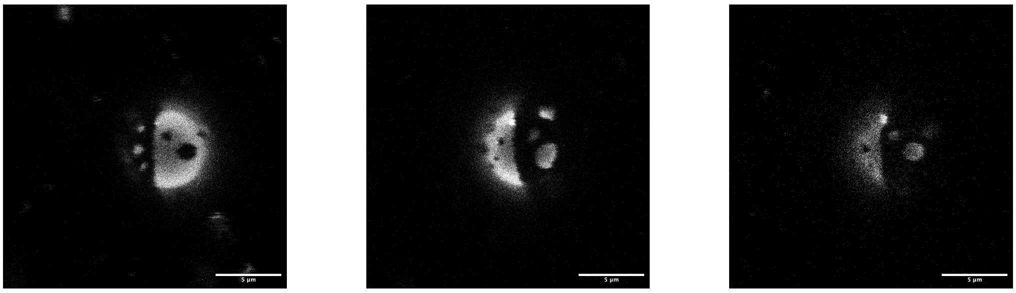

(a) LissRhodPE

(b) TF-Chol

(c) Biotin-PEG2K-DSPE, labeled with streptavidin-Af405

Figure 3.27: A GUV functionalized with Biotin-PEG2k-DSPE, labeled with LissRhodPE (**a**, Ld phase), and Tf-Chol (**b**, Lo phase). The biotin in the membrane **c** is visualized by adding fluorescently labeled streptavidin and localizes in the Lo phase. Scale bar is 5 µm.

3.4.2 Guiding phase separation by interaction with micropatterns

In the next step, i set out to investigate wether domain localization in phase separated GUVs could be influenced by deformation induced by adhesion to micropatterned surfaces. When phase separated GUVs are deflated, they deform to an elongated shape of two partial spheres connected with a kink along the phase boundary [96]. This led to the hypothesis that phases could, in return, be organized when GUVs are deformed on line shaped patterns, leading to a front localized with one, and a back with the other phase. It was shown before, that domains in phase separated vesicles could be guided to the adhesion site when GUVs with biotinylated lipids, that accumulate in one phase, were adhered to streptavidin functionalized surfaces. The interaction of the biotin with the streptavidin at the surface increase the local concentration of biotinylated lipids at the adhesion site. This increase in concentration of, in this case saturated lipid, draws the Lo phase, wich is prefered by the biotinylated lipids to the adhesion site[101]. Additionally, if the surfaces were microstructured with ridges, the domains organized the shape of the underlying microstructures[102]. A similar effect was observed, when actin filaments were anchored to phase separated supported lipid bilayers via biotinylated lipids. Here, the biotin-rich domains of the lipid bilayer follow the structure of the actin network. Again, the biotinylated lipids are locally concentrated due to the interaction with the actin filaments, driving the domain organization.

To adhere phase separated GUVs, they were produced with Biotin-PEG2k-DSPE containing lipid mixtures (Table 2.6 and 2.9) and seeded on micropatterned surfaces, that were functionalized with streptavidin. Although the goal seemed to be straightforward, it took considerable amounts of attempts, until the protocol worked reliably. GUVs in this section were prepared with the emulsion transfer method and with electroformation. Since I want to first study the lipid domain organization in the absence of proteins on the inside, any GUV production method that yields phase separated GUVs could be used. In the future, when additional cargo is to be incorporated into the phase separated GUVs, the emulsion transfer method optimized in section 3.4.1 can be utilized. This is important, if the domain organization is intended to be used as a scaffold to organize proteins in the future.

An example of an adherent, phase separated GUV is shown in Figure 3.28 at the adhesion side **(a)**, and as cut along **(b)** and through the micropatterned line **(c)**. The Tf-chol (green) partitions into the Lo phase together with the biotinylated lipid, as shown before, LissRhod PE (magenta) into the Ld phase. It can be seen, that a cholesterol rich domain localizes at the micropatterned adhesion site. This is explained by the interaction of the biotinylated lipids with the streptavidin, which causes the biotinylated lipids to enrich at the adhesion site. The high local concentration of unsaturated, biotinylated lipids pulls in return the cholesterol rich Lo-phase to the pattern as reported before[101]. WIth that, the results obtained from GUVs adhering to micropatterned surfaces in my work are in line with the results, where GUVs were adhered to microstructured surfaces with grooves[102]. There, the biotin-rich domains accumulated on the streptavidin functionalized parts of the surface, that were in direct contact with the GUV.

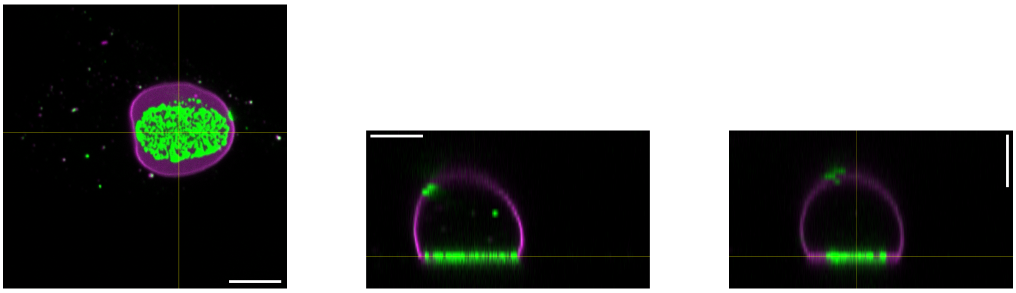

(a) xy cut at the adhesion site of the GUV

(b) Orthogonal xz cut through the GUV

(c) Orthogonal yz cut through the GUV

Figure 3.28: Shown is the membrane in magenta and the Tf-cholesterol in green. It can be seen, that the cholesterol localizes at the micropatterned adhesion site. Scale bar is 5 µm.

This finding was further confirmed when line micropatterns with irregular streptavidin coverage were employed to adhere GUVs (Figure 3.29). In some cases, when dirt or remnances of liquid were present during the patterning process on the coverslip, interference pattern could be seen in the micropatterns. These manifest on line shaped micropatterns as irregularities in the pattern intensity, which indicated irregularities in the local coverage of the patterns with streptavidin (Figure 3.29**d**). Here, we utilized these irregularities in the pattern to show that cholesterol, and thus the Lo phase only colocalizes with the pattern in areas where the streptavidin signal has a sufficient intensity (Compare Figure 3.29**c** and **d**). The Ld marker LissRhod PE is missing in cholesterol rich areas, but present in the parts where the streptavidin signal is low, indicating the presence of Ld phase in areas, where streptavidin is lacking (See Figure 3.29**a** or **b**).

I didn't further investigate the dependency of pattern strength and cholesterol localization further due to time constraints. Nevertheless, I demonstrated that it is possible to guide domains in phase separated vesicles using adhesion. In the here shown example in Figure 3.29, alternating patches of Lo and Ld were obtained in adherent GUVs presumably due to the alternating levels of biotinylated lipids. Such an approach to domain organisation might allow to induce controlled inhomogeneities on the adherent parts of the GUVs.

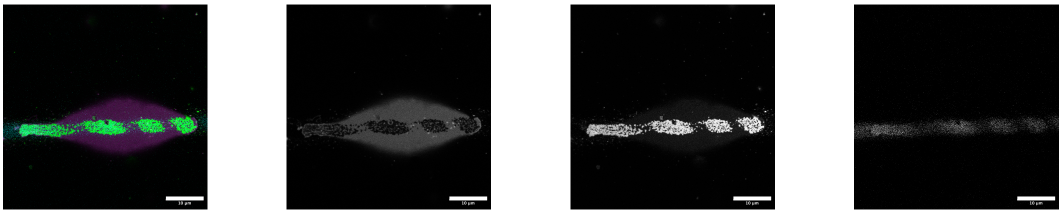

(a) Composite image **(b)** LissRhod **(c)** Tf-Chol **(d)** Streptavidin pattern

Figure 3.29: Shown is a GUV, produced using electroformation, adhering to a line pattern that displays a fluctuating streptavidin covering. In **a**, the LissRhod channel is visualized in magenta, Tf-Chol in green and the pattern in cyan. It can be seen, that the cholesterol colocalizes at the micropatterned adhesion site, where the micropattern has a high intensity, leading to the striped appearance along the line pattern. Each channel is shown individually in **b**, **c** and **d**, to visualize the colocalization between the Lo marker cholesterol and the pattern. Scale bar is 10 µm.

3.4.3 Cap formation induced by adhesion and deformation of GUVs

The experiments presented in this section were performed on stripe micropattern of 15x2 µm size, to keep the deformation consistent with findings shown in the sections before.

It was shown earlier that active deformation of GUVs can have an influence on the coalescence of domains in phase separated vesicles[145]. This was only observed while the geometry of the GUV was actively changed and driven out of equilibrium, which influenced additional parameters such as the membrane tension. GUVs adhering to micropattterns are assumed to be in thermodynamic equilibrium. For a free floating phase separated GUV at the energetic minimum two large domains are expected to co-exist, which minimizes the line-energy between the two domains. When the GUV is deflated, meaning the volume of the vesicle is reduced while the membrane area is kept constant, the GUV deforms into a pear-like shape, with the domain-boundary forming the neck between two spherical segments[146].

Since this deformation resembles the elongated shape that GUVs adhering to a stripe micropattern obtain, it could lead to a controlled phase organization with one phase at the front, and the other at the back upon desormation which is induced by adhesion to the micropatterns. On adhesive micro patterns, the front-back polarity, that I expected based on the shape of free floating, phase separated GUVs, was not found in any experiment I performed.

Instead the expected front-back polarity, a cap-formation where a domain is located on the top of the GUV, as shown in Figure 3.30 was observed. In Figure 3.30**a**, a confocal image of an adherent, phase separated GUV is shown at the z-slice close to the adhesion site. Here, the localization of the biotin-rich Lo phase (Tf-chol, green) at the adhesion site due to the high local concentration of biotinylated lipids can be seen, as described in section 3.4.2. In Figure 3.30**b** and **c**, an orthogonal cut along and through the adhesive line are shown respectively. At the bottom of the GUV, the accumulation of Lo phase can again be observed at the flat adhesion site. In the upper region a Lo domain (green) forms a cap on top of the GUUV (Figure 3.30**b**, and **c**).

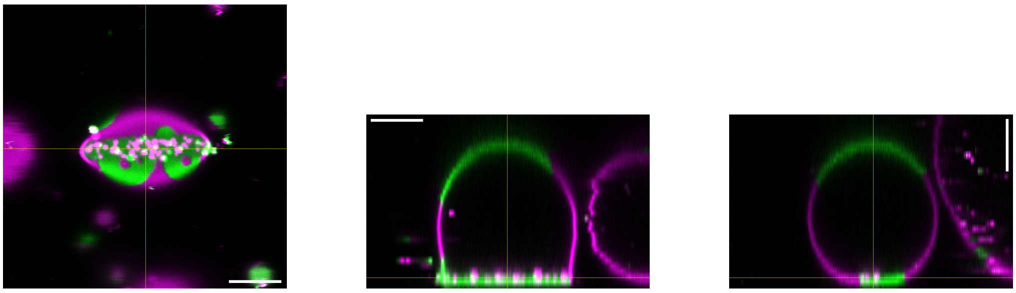

(a) xy plane at the adhesion site of the GUV

(b) xz cut through the GUV

(c) yz cut through the GUV

Figure 3.30: Shown is the Ld marker, LissRhod PE in magenta and the Tf-chol (Lo phase) in green. Cholesterol localizes at the micropatterned adhesion site, seen in **a**. Further, a green Lo cap is seen at the top of the GUV in the orthogonal cuts depicted in **b** and **c**. Scale bar is 5 µm.

Such a cap formed by a domain localized at the top was observed in many GUVs (Figure 3.31). It should be noted, that the caps are not exclusively comprised of the Lo phase (green), but can also be made up by the Ld phase (magenta). Examples for both cases are found in Figure 3.31. Each subfigure is labeled with the phase that comprises the domain at the cap of the GUV. Such a stable localization of domains in deformed, adherent GUVs is remarkable. It resembles the apical/basal polarity found in epithelial cells, although the origin of the organization is likely very different.

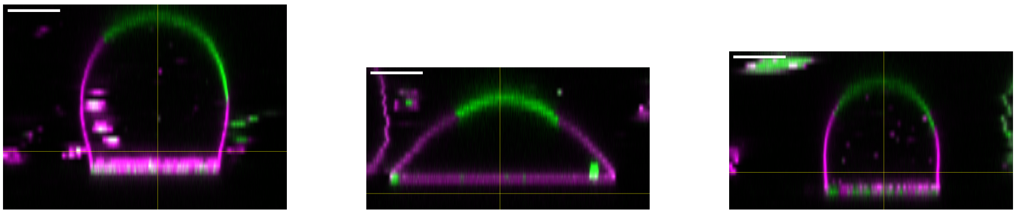

Lo cap Lo cap Lo cap

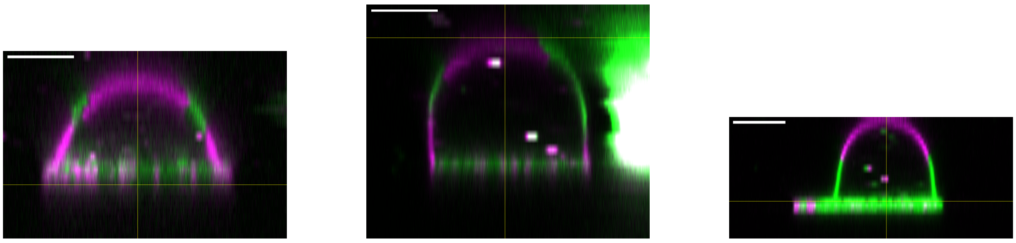

Ld cap Ld cap Ld cap

Figure 3.31: Examples of adherent phase separated GUVs shown in an xz cut, along the adhesive line. One can see the Lo cap (green) in the top row of images, or the Ld cap (magenta) in the bottom row. Data is taken from 3 independent experiments, with GUVs formed using the electroformation and emulsion transfer method. Scale bar is 5 µm.

As demonstrated in Figure 3.31, the occurrence of a cap was observed in a large number of GUVs. Thus, I was interested, whether the domain localization was stable over time. A representative time course of a GUV over 18 min with an Lo cap is shown in Figure 3.32. The green Lo cap can be seen localized over this time course at the top of the GUV. Together with the observation of such a cap formation in many cases, it indicates that this configuration might be a stable state.

Next, I wanted to observe the phase organization over even longer periods of time. To this end, I imaged a sample of adherent GUVs on stripes directly after formation and adhesion to micropatterned surfaces and 3 days later. A representative GUV is shown in Figure 3.33**a**, with the Lo phase shown in green, and the Ld phase in magenta. In Figure 3.33**b**, the Ld phase of the same GUV is shown. One can see the localization of the Ld phase in Figure 3.33**a** and **b** are very similar with two Ld domains located at both ends of the long axis of the GUV, indicating no change in organization over a timecourse 3 days. The Lo marker was omitted at the later time points, as the Tf-Chol dye bleached fully during the experiment. When the sample was imaged for an hour, the GUV started to peel from the surface, leading to a more spherical shape (Figure 3.33**c**). This effect is presumably due to

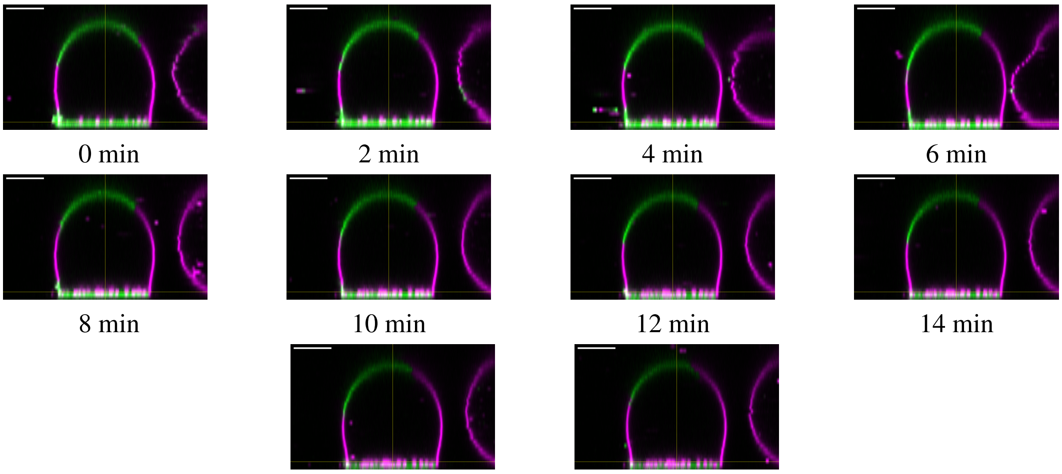

0 min 2 min 4 min 6 min

8 min 10 min 12 min 14 min

16 min 18 min

Figure 3.32: Adherent phase separated GUV shown in an xz cut over a time of 18 min. An image was taken every 2 minutes. One can see the green Lo cap localized at the top of the GUV over the time course. A slight bleaching of the green dye can be observed during the experiment. Scale bar is 5 µm.

photo damage of the streptavidin protein, that mediates the adhesion between the GUV and the micropattern. Finally the GUV detaches and assumes a spherical shape (See Figure 3.33**d**). Here, only the half-circle made by the Ld phase can be seen. The organization of the Ld phase, with both ends labelled that was stable for three days is lost and the domain organization with a single domain, typical for spherical GUVs, is recovered. This further indicates, that domain organization on micropattern is at an energetic minimum, that reorganizes when the attachment is lost.

I showed that domains in phase separated, adherent GUVs organize due to geometrical cues. On line shaped micropatterns this manifests in a formation of a cap of one domain at the top of the adherent GUVs. Further, this domain localization appears to be stable over minutes to several days. This is an advantage if deformation was used as a cue for the stable organization of phases, and via this proteins inside of GUVs. I further show, that the expected minimal energy configuration with only two domains coexisting is reestablished, when a GUV is detached from the surface.

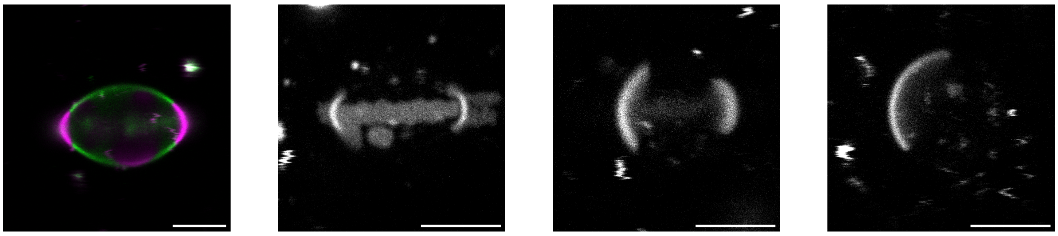

(a) Image of phase separated GUV **(b)** LissRhod channel of phase separated GUV 3 days later **(c)** Detaching GUV after 1 h laser exposure **(d)** Fully detached GUV after 1.5 h laser exosposure

Figure 3.33: Preliminary data of a GUV peeling off the micro pattern after extended laser-exposure during confocal imaging. In a the GUV is shown directly after formation and adhesion to the micropattern. The Ld phase is shown in magenta, Tf-cholesterol (Lo) phase in green. b) The Ld phase of the same GUV shown 3 days later. One can still see the bright, Ld rich ends of the GUV. c) After extended laser exposure of the GUV, it starts to peel off the micropattern and become more circular. d) After 1.5 h, the GUV has peeled fully from the micropattern and assumes a spherical geometry. The domain organization is lost, and the single domain typical for phase separated spherical GUVs is recovered. Scale bar is 5 µm.

3.5 Monte Carlo simulation of phase separation on triangulated surfaces based on line tension

The experimental results shown above indicate that circular domains of one phase localize at the GUV top and form a cap due to geometrical cues. Similar observations where domains localized in dependence of geometrical cues were made for phase separated GUVs confined in microfluidic channels[100]. To better understand the mechanism of the organization of domains in phase separated vesicles du to deformation, I simulated phase separated GUVs on triangulated, closed, surfaces. Using triangulated surfaces gives us access to any shape a GUV can assume, without any constrains such as symmetry. Further, triangulated meshes are easily generated using open-source software, such as Blender. In order to model GUVs, the energy contributions, that can influence the domain distribution in phase separated GUV are mainly line-tension from the domain boundaries, and curvature preferences of each phase[113]. As we have seen above, curvature did not seem to influence the domain localization on top of the GUVs, as both phases were found in the cap. Also the experiment where a GUV was detached (Figure 3.33) pointed, with the single spherical domain after detachment, to a line-tension driven organization. Similar observations were made for vesicles confined in microfluidic channels, where the minority phase, wether it was the Lo or Ld phase, accumulated in the free standing region of the confined vesicle, which was proposed to be line-tension driven[100].

Therefore we assume only the line-tension contribution to the total energy of a phase separated GUV to be relevant:

$$E_{LT} = l\sigma \tag{3.3}$$

where l denotes the length of the domain boundary between two phases separated vesicle, and σ the line tension, which is a result from the thickness mismatch of the lipid membrane of the two adjacent phases. In the simulations presented here, the line-energy, E_{LT}, is defined on a triangulated mesh. To this end, each triangle is thus assigned a phase, here called a or b. We assume, that both phases have the same properties and that a line-tension exists at the boundary of the two phases. Further, the geometry of the vesicle is kept fixed and therefore not influenced or changed by the phase distribution, as done in earlier calculations by Amazon et al.[113]. From there, the only energy contribution comes from the line-tension as described in equation 3.3.

We define a triangle k and with the adjacent triangles s, with the phase a or b respectively, as shown in the diagram in Figure 3.34. The energy is dependent on the length of the phase boundary and the phases of the triangles, as described in equation 3.3.

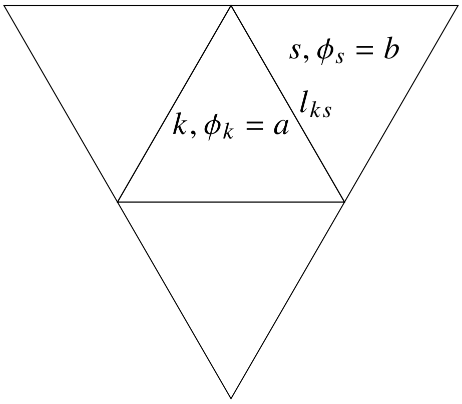

Figure 3.34: Neighboring triangles k and s, with the phase ϕ of a and b respectively and the shared side l_{ks}.

The energy of a single triangle k, surrounded by the three triangles s is defined as

$$\epsilon_k = \sum_{s}^{3}(1 - \delta_{\phi(k)\phi(s)})l_{ks}\sigma \tag{3.4}$$

with $\phi(k)$ and $\phi(s)$denoting the phase of a triangle k and s respectively, l_{ks} the length of the shared side of triangle k and s and σ the energy corresponding to the line tension. The $1 - \delta_{\phi(k)\phi(s)}$ term is zero, when both phases of the triangles k and s are equal and one if k and s have different phases to account for a line-tension energy only when the phases of the adjacent triangles are not equal.

The total energy can then be calculated by summing over all triangles:

$$\epsilon = \frac{1}{2} \sum_{k}^{triangles} \sum_{s}^{3} (1 - \delta_{\phi(k)\phi(s)}) l_{ks} \sigma \tag{3.5}$$

The pre-factor of $\frac{1}{2}$ is introduced to account for double counting when the sum runs over all triangles, since l_{ks} will be counted twice, when the energy of triangle k, and when the energy of triangle s is added.

Given the energy we can calculate the probability of a state using the Boltzmann distribution. From there, the probability ratio $\frac{p_p}{p_q}$ of the state p and q, with the corresponding energies of ϵ_p and ϵ_q is easily obtained:

$$\frac{p_p}{p_q} = e^{-\frac{1}{kT}(\epsilon_p - \epsilon_q)} \tag{3.6}$$

This gives us a framework to compare the probabilities of 2 states at a given temperature and thus allows us to compute the phase distribution in a Monte Carlo based approach. In order to compute the energy difference $\epsilon_p - \epsilon_q$ in equation 3.6, calculation the total energy by evaluating sum over all triangles as given in equation 3.5 is computationally expensive and slow. I thus simplified the computations necessary to obtain the energy difference $\epsilon_p - \epsilon_q$.

In the first step, the sum to compute the total energy from equation 3.5 can be segmented, focussing on the two arbitrary triangles i and j, where $i \neq j$:

$$\epsilon^{i,j:i\neq j} = \frac{1}{2} \sum_{k\neq i,j}^{triangles} \sum_{s}^{3} 1 - \delta_{\phi(k)\phi(s)} l_{ks} \sigma + \sum_{s}^{3} 1 - \delta_{\phi(i)\phi(s)} l_{is} \sigma + \sum_{s}^{3} 1 - \delta_{\phi(j)\phi(s)} l_{js} \sigma \tag{3.7}$$

We now define a state p with the phase of triangle i $\phi(i) = a$, phase of triangle b as $\phi(j) = b$, and a state q with both phases exchanged. Then, the equation for $\epsilon_p - \epsilon_q$, as used in equation 3.6 can be written as:

$$
\begin{aligned}
\left[\epsilon_p^{i,j:i\neq j}\right] - \left[\epsilon_q^{i,j:i\neq j}\right] = \frac{1}{2}&\left[\sum_{k\neq i,j}^{triangles}\sum_{s}^{3}(1-\delta_{\phi(k)\phi(s)})l_{ks}\sigma\right.\\
&\left.+\sum_{s}^{3}(1-\delta_{\phi(i)=a,\phi(s)})l_{is}\sigma+\sum_{s}^{3}(1-\delta_{\phi(j)=b,\phi(s)})l_{js}\sigma\right]\\
-\frac{1}{2}&\left[\sum_{k\neq i,j}^{triangles}\sum_{s}^{3}(1-\delta_{\phi(k)\phi(s)})l_{ks}\sigma\right.\\
&\left.+\sum_{s}^{3}(1-\delta_{\phi(i)=b,\phi(s)})l_{is}\sigma+\sum_{s}^{3}1-\delta_{\phi(j)=a,\phi(s)}l_{js}\sigma\right]
\end{aligned}
\tag{3.8}
$$

It should be noted, that, when $\phi(i)$ and $\phi(j)$ both correspond to the same phase, their exchange will create the starting state, and can thus be ignored. From there we see the first sum cancels out, leaving us with:

$$
\begin{aligned}
\left[\epsilon_p^{i,j:i\neq j}\right] - \left[\epsilon_q^{i,j:i\neq j}\right] = \sigma&\left[\sum_{s}^{3}(1-\delta_{\phi(i)=a,\phi(s)})l_{is}+\sum_{s}^{3}(1-\delta_{\phi(j)=b,\phi(s)})l_{js}\right]\\
-\sigma&\left[\sum_{s}^{3}(1-\delta_{\phi(i)=b,\phi(s)})l_{is}+\sum_{s}^{3}1-\delta_{\phi(j)=a,\phi(s)}l_{js}\right]
\end{aligned}
\tag{3.9}
$$

This can now be incorporated into equation 3.6, to give the probability ratio between the two states. It is evident that the prefactor of $\frac{1}{2}$ originating from equation 3.8 is absent in equation 3.9. This absence arises due to the exclusion of the energy contribution of triangle s, thus avoiding the issue of double counting.

In praxis this now gives us a probability for the transition from state p to state q, depending on the energy difference. We can then use this to decide whether to accept or reject the new proposed state in a Monte-Carlo based approach, using:

$$
\mathrm{w} < e^{-\frac{1}{kT}(\epsilon_q-\epsilon_p)}. \tag{3.10}
$$

with a uniform random number w between zero and one, which allows to accept or reject a proposed state proportional to the probability of occurrence. If the energy of the proposed state with the energy ϵ_q is smaller than the energy corresponding to the current state ϵ_p, the newly proposed will always be accepted. If the energy is higher, the probability of accepting the suggested state is dependent on the energy difference, as well as on the temperature, with the probability decreasing with an increasing energy difference and decreasing temperature. This should thus give us the option to simulate phase separation behavior on arbitrary triangulated surfaces, assuming line tension is the only energy contribution to take into account. To generate the trial state q, two triangles i and j are chosen at random and the energy difference $\epsilon_q - \epsilon_p$ is computed when the phase of the two triangles is switched.

For the implementation, to make the results obtained for different GUV shapes more comparable, the GUV size was normalized to the surface area of a sphere with a diameter of 10 µm. This is important, since the line energy is dependent on the length of the phase boundary and therefore, on the GUV size when all other parameters are kept constant. Here, I want to explore the phase distribution in a geometry, but not size-dependent manner. Since the energy scales linearly with the length of the phase boundary, an increase in GUV surface area has similar effects as an increase in line tension. Furthermore, I made the assumption that all triangles are equal in size. With this assumption, the surface area covered by each phase remains constant throughout the simulation, provided that the number of triangles per phase remains consistent. For most simulations I started with a random distribution of both phases on the triangles. I use magenta and green colors to indicate similar phase behavior as in the experimental observations. It should be kept in mind though, that both phases in the simulations have the same properties and are thus arbitrarily colored. All calculations were made using 75% surface coverage of one phase (depicted in magenta, the majority phase), and 25% surface coverage of the other phase (Depicted in green, the minority phase) at a temperature of 300 K and various line-tension values σ given in pN throughout this section. An increase in temperature and a decrease of the line-tension σ are equivalent in the here presented simulations, as the probabilities depend on the ratio of energy difference and temperature (See equation 3.6). Temperature and line-tension are connected by the relation:

$$\frac{\sigma}{T_c} = \frac{\sigma_c}{T} \tag{3.11}$$

where in the here presented simulations the line tension, σ was changed at a constant temperature T_c of 300 K and can be translated to a constant line-tension value at different temperatures.

The line-tension values used in the here presented simulations ranged from 0.01 - 0.1 pN, about two orders of magnitude lower than reported values of about 2 pN for vesicles composed of DOPC, DPPC and cholesterol[147]. The values were selected based on the observation that lower line-tension values resulted in a uniform distribution of phases,

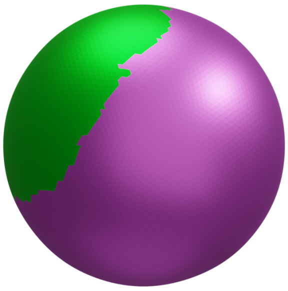

Figure 3.35: Simulated phase distribution on a spherical GUV surface, with σ=0.05 pN. The expected organization in one circular cap of the minority phase (green) surrounded by the majority phasRe: another papiere (magenta) is observed.

without discernible phase separation. Conversely, values exceeding 0.1 pN led to slow evolution, as proposed states with higher energy than the current state became progressively less probably accepted, resulting in high number of rejected states. The simulations implemented in this work, thus utilized similar values for the line tension as earlier reports of Monte Carlo simulations[113].

First, to provide a proof of concept, the domain distribution of a phase separated sphere was computed, with $\sigma = 0.05$ pN (Figure 3.35). One can see in the render of the sphere, depicting the resulting domains after $5x10^10$ iterations, the minority phase in green comprising one circular domain, surrounded by the majority phase in magenta. This resembles the experimental as well as the theoretical observations for phase separated vesicles, as the circular shape minimizes the line energy between the two phases[113].

In deformed, rod-shaped vesicles it was recently shown experimentally by K. Nakazawa et al. that in some cases the minority phase localized at the end sections in GUVs under confinement in microfluidic channels (Figure 3.36)[100]. They used two different lipid compositions, that result in the Ld and the Lo phase comprising the minority phase respectively, marked by Comp. 1 and Comp. 2 in Figure 3.36. There it was shown that the minority phase localized at both ends of the rod-shaped vesicle, leading to the formation of two caps (denoted in green in Figure 3.36a). Both the Lo and Ld phases are localized at the free-standing regions of the confined GUVs depending on which phase comprisd the minority phase, where they were unaffected by the microfluidic channel walls. Thus it was hypothesized that neither the interaction with the microfluidic chip, nor a curvature preference of the phases played a significant role in the domain localization. The domain organization was thus proposed to be line-tension driven.

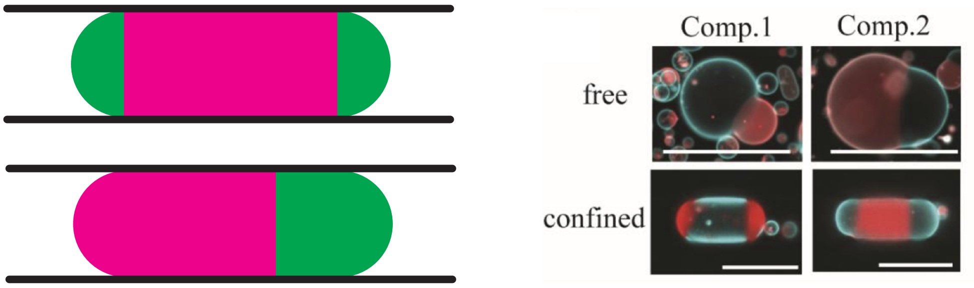

(a) Scheme of a confined GUV in a microfluidic channel, with two caps (top) and one cap (bottom).

(b) Experimentally observed GUVs free (top) and confined (bottom). Image adapted from K. Nakazawa et al.[100]

Figure 3.36: (a) Schematic view of the domains in a phase separated GUV under confinement in a microfluidic channel. At the bottom, the expected result, if the line energy along the cylindrical part is minimized. At the top, a scheme of the results obtained experimentally by K. Nakazawa et al. **(b)** Experimentally observed GUVs with different lipid composition (Comp.1 and Comp.2), yielding Ld, and Lo phase as the minor phase respectiveley, that localizes at the ends of the major axis respectively[100].

We established earlier, that the energy contribution stemming from the line tension is dependent on the length of the interface between two domains in a linear fashion (see equation 3.3). The shape of a GUV confined in a microfluidic channel can be approximated by a cylinder with a half-sphere cap at both ends, allowing for preditctions of the phase behavior using of the Monte Carlo simulations described before (compare Figure 3.36a and 3.36b). The deformed model GUV is made up by a phase separated membrane and its minority phase can occupy both spherical caps while still reach into the cylindrical part of the GUV, as indicated at the top in Figure 3.36a. The total line-energy of such an ideal system with a cap at each end would now be given by

$$E_{LT} = 2\sigma C, \tag{3.12}$$

where C is the circumference of the cylindrical part of the GUV and the pre-factor of two is stemming from the two caps. When only one cap is present, as visualized in Figure 3.36a at the bottom, the energy should be equal to σC, as there is only one phase boundary. With this simple assumptions, we would thus expect the upper case presented in figure 3.36a to have double the line energy, as the lower case. The observations by K. Nakazawa et al., presented in figure 3.36b, can thus not simply be explained by a minimization in line energy, that drives the lipid organization found in the experimental data. Therefore I set out to use the Monte Carlo simulation described before to elucidate the observations made by K. Nakazawa et al.

An idealized GUV shape representing a GUV confined in a microfluidic channel was build, comprised of a cylinder with two half-spherical caps using Fusion360, and turned into a triangulated mesh using Blender. Due to the simplicity of the shape, it was used as a test-case to see whether I could recreate the 2-capped vesicle found in the experimental results. Further, since only line-tension is taken into account in the simulations, the observations would be able to be linked to this effect alone, determining whether line-tension is sufficient to explain the experiments. We simulated the vesicle for $5x10^{10}$ proposed states, that were accepted with a probability based on the line energy and temperature (see equation 3.6). One should note, that the simulation is in the end a one-parameter model, as changes in temperature and line-tension values can be seen as equivalent.

When the line-tension is set to zero, the phase distribution is fully random, as the total energy of all states is zero. An increase of the line-tension to 0.02 pN (Figure 3.37), there is no change, that can be visually observed in the render shown in Figure 3.37**d**. When the average phase distribution of the final $1x10^9$states is plotted along the major axis, a slight preference of the minority phase localizing around the end-caps can be seen (Figure 3.37**c**). This is equivalent to an average over last two lines of the plots shown in Figure 3.37**a** and **b**. The plots were normalized to reflect the ratio of either phase along the major axis of the rod-shaped GUV. Although this points to the existence of a state with two minority caps, the results are not yet overwhelmingly clear.

When the line-tension is increased to 0.3 pN, the experimental results by K. Nakazawa et al., where they observed the minority phase localizing in the two caps at the end of rod-shaped GUVs are found in the simulations[100] (Figure 3.38). In the render of the deformed GUV, in Figure 3.38**d**, the green phase is clearly localized at the caps of the GUV throughout the simulation. This behavior is also reflected in the graph, in Figure 3.38**c**, where the phase portion is plotted in dependence of the position along the long axis of the GUV. In the plots depicting the trajectory of the simulation, in Figure 3.38**a** and **b**, one can see the domain distribution to manifest almost instantly into a two-capped state, and stay like this during the whole simulation, pointing towards a stable state. This result strongly supports the hypothesis, that such a two-capped state can be stably obtained, when phase behavior is governed by line tension only.

As the line tension is further increased to $\sigma = 0.04$, the two-capped state becomes absent, and instead a GUV with a single cap is observed, as illustrated schematically in Figure 3.36a. The simulation results in Figure 3.39**a** show a short-lived 2-capped state, that then evolves into a state with a single minority cap, as predicted, when line energy minimization is the driving factor. The resulting phase distribution can be seen in the plot in Figure 3.39**c**, as well as the rendered image in 3.39**d**. One can clearly see the emergence of a single capped state. If the line-tension is increased further, to 0.5 pN, the same behavior is

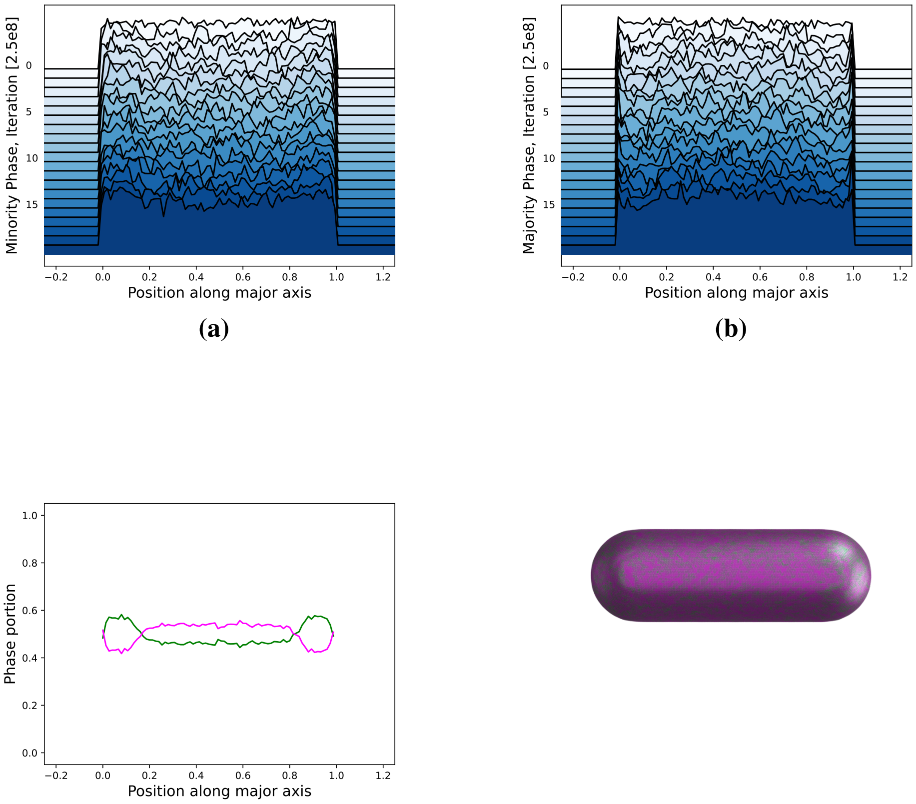

(a) **(b)**

(c) **(d)**

Figure 3.37: Simulation result for $\sigma = 0.02$ pN on a rod-shaped GUV over $5x10^{10}$ proposed states. In **(a)**, the phase portion of the minority phase is plotted over the selected iteration steps of the simulation, in (**b**) the majority phase is plotted. In **(c)**, the average of the phase portion, normalized to one, of the last $5x10^8$ iterations is plotted against the position along the major axis of the GUV, where 0 and 1 are both ends of the GUV. In the average, a preference of the minority phase (green) is observed for the end-parts of the GUV. In the image in **(d)**, the average phase distribution throughout the simulation is visualized on the GUV surface. Here, no preference in the phase distribution is apparent.

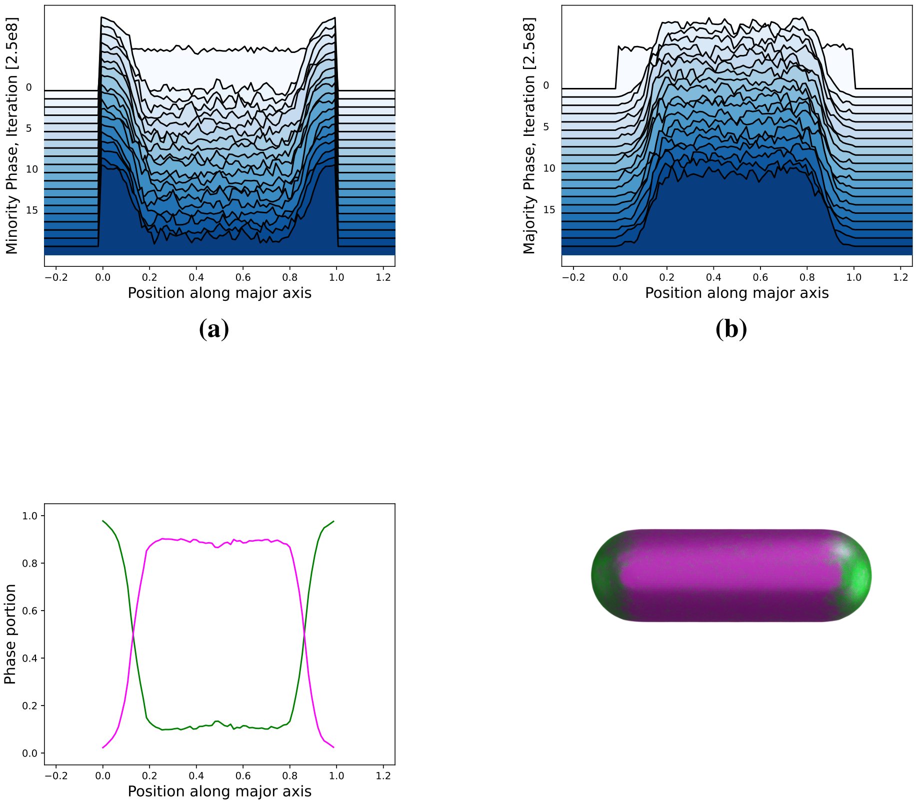

(a) **(b)**

(c) **(d)**

Figure 3.38: Simulation result for $\sigma = 0.03$ pN on a rod-shaped GUV over $5x10^{10}$ proposed states. In **(a)**, the phase portion of the minority phase is plotted over the selected iteration steps of the simulation, in **(b)** the majority phase is plotted. In **(c)**, the average of the phase portion, normalized to one, of the last $5x10^{8}$ iterations is plotted against the position along the major axis of the GUV, where 0 and 1 are both ends of the GUV. In all graphs, a strong preference of the minority phase (green) is observed for the end-parts of the GUV. In the image in **(d)**, the average phase distribution throughout the simulation is visualized on the GUV surface. Here, a clear preference in the phase distribution is apparent, reflecting the experimental results seen by K. Nakazawa et al.[100]

observed, although the trajectory into the single cap state is slower (Figure 3.40). This can be explained, as the amount of accepted states, that are higher in energy than the current state is much lower when the line-tension is increased, leading to a slower evolution, or even a frozen state, where no proposed state is accepted, as the probability is too low, and no lower energy state can be obtained by a single phase exchange between two triangles.

To verify, that the emergence of the two capped state for line-tension values below $\sigma = 0.04$ pN is a frequent occurance, I run a simulation with a line-tension value of $\sigma = 0.03$ pN, which gave a phase-separated state as result with two caps, one at each end of the GUV, although a single-capped state was used as a starting point, as found with $\sigma = 0.05$ pN (see Figure 3.40). In this simulation, I was able to rescue the two-capped state, pointing to a reliable and stable generation of a two-capped state, even if the starting configuration was a state that is expected to have a lower line energy (Figure 3.41). While the single-capped state is anticipated to represent the energetic minimum, simulations conducted with lower line-tension values below 0.04 pN, corresponding to higher temperatures, suggest the presence of a stable state with two caps. This implies that a greater number of configurations may lead to the formation of such a state, indicating that the existence of the two-capped state is likely an entropic effect. This explains the ability to observe such a state in experiments though, as it seems to be stably generated under the correct conditions, regardless of the starting state.

An additional observation worth noting is the increase of noise with decreasing line-tension values. This is expected, as lower line-tension values are equivalent to higher temperatures, due to more thermal fluctuations. Furthermore, I want to point out, that simulations with line-tension values of 0.04, and 0.05 pN start in their first iterations from a state with two caps (See Figure 3.39**a** and 3.40**a**) In the case of $\sigma = 0.04$ pN, this state is very short lived, as the one-capped state emerges after $5x10^8$ iterations. For $\sigma = 0.05$ pN, the two capped state exists for a higher number of iterations, and slowly decays into a single capped state after $3.75x10^9$ iterations. This further hints to a high likelihood to observe a two capped state.

Using Monte Carlo simulations of phase separation on confined model GUVs I could confirm, that domain organization and localization can indeed be solely explained by line-tension. Line-tension values below 0.04 pN gave rise to states, that were comparable to the experimental observations by K. Nakazawa et al.[100]. Here, a two-capped state emerged stably in the simulations,whether the starting point was a random distribution, or a single-phase state, that is expected to be the energetic minimum. On the other hand, higher line-tension values produced GUVs, that had only one cap, as expected for a rod-

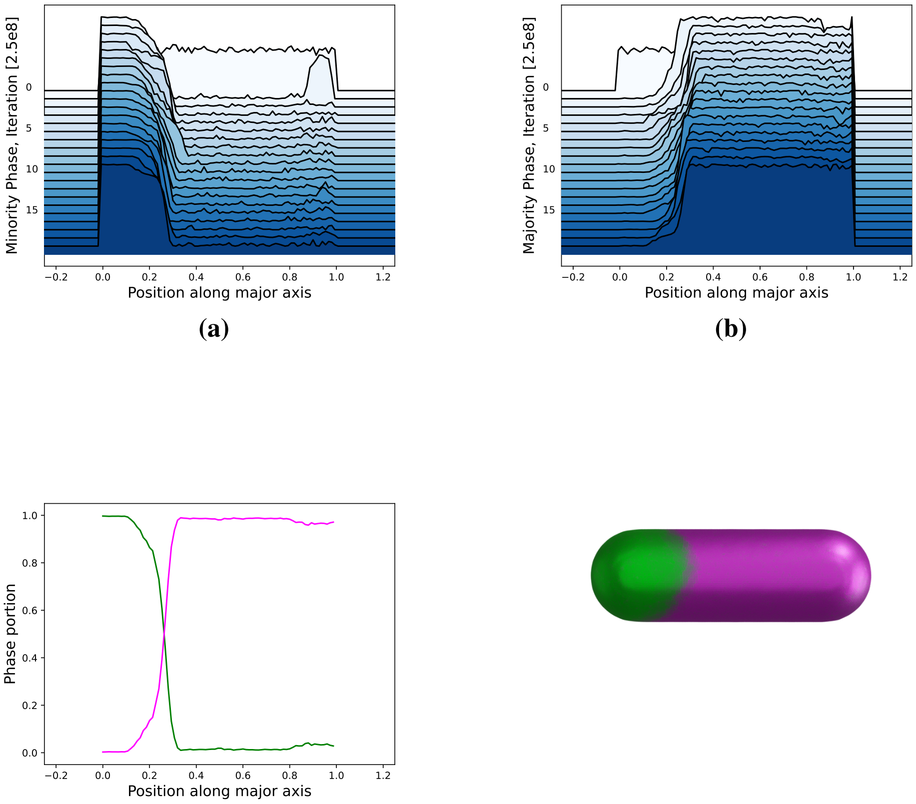

(a)

(b)

(c)

(d)

Figure 3.39: Simulation result for $\sigma = 0.04$ pN on a rod-shaped GUV over $5x10^{10}$ proposed states. In **(a)**, the phase portion of the minority phase is plotted over the selected iteration steps of the simulation, in **(b)** the majority phase is plotted. In **(c)**, the average of the phase portion, normalized to one, of the last $5x10^{8}$ iterations is plotted against the position along the major axis of the GUV, where 0 and 1 are both ends of the GUV. In all graphs, a strong preference of the minority phase (green) is observed for one of the end-parts of the GUV. In the image in **(d)**, the average phase distribution throughout the simulation is visualized on the GUV surface. Here, a clear preference in the phase distribution is apparent, reflecting the expectation, when the line-tension is minimized, as shown in the lower case of figure 3.36a.

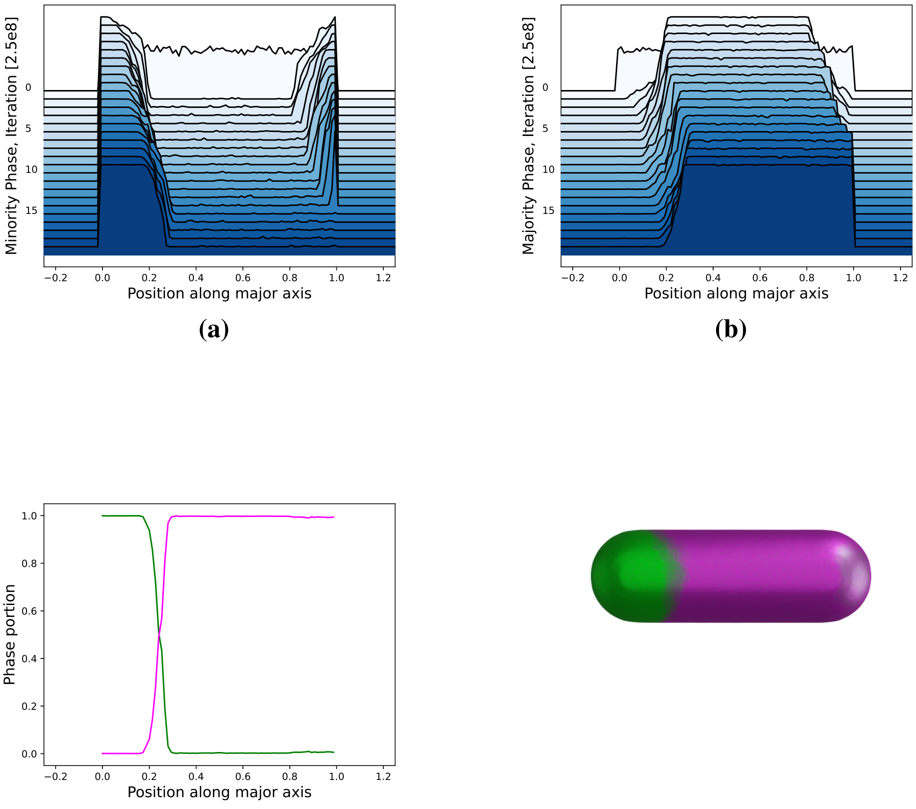

(a) (b)

(c) (d)

Figure 3.40: Simulation result for $\sigma = 0.05$ pN on a rod-shaped GUV over $5x10^{10}$ proposed states. In **(a)**, the phase portion of the minority phase is plotted over the selected iteration steps of the simulation, in **(b)** the majority phase is plotted. In **(c)**, the average of the phase portion, normalized to one, of the last $5x10^{8}$ iterations is plotted against the position along the major axis of the GUV, where 0 and 1 are both ends of the GUV. In all graphs, a strong preference of the minority phase (green) is observed for one of the end-parts of the GUV. In the image in **(d)**, the average phase distribution throughout the simulation is visualized on the GUV surface.

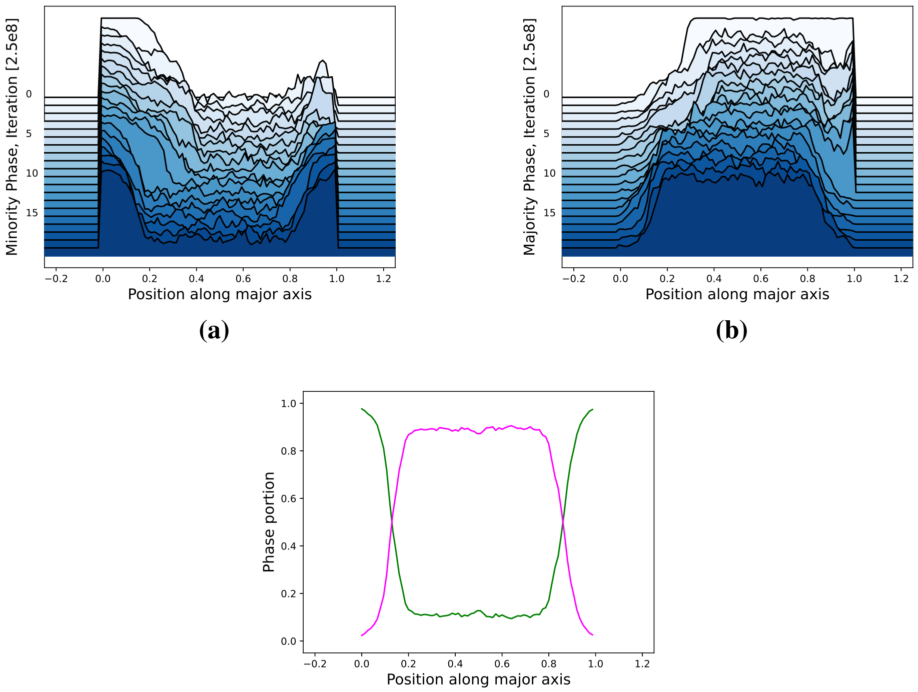

(a) **(b)**

(c)

Figure 3.41: Simulation result for $\sigma = 0.03$ pN on a rod-shaped GUV over $5x10^{10}$ proposed states, starting from a state with a single cap, as seen in figure 3.39. In **(a)**, the phase portion of the minority phase is plotted over the timecourse of the simulation, in **(b)** the majority phase is plotted. In **(c)**, the average of the phase portion, normalized to one, of the last $5x10^{8}$ iterations is plotted against the position along the major axis of the GUV, where 0 and 1 are both ends of the GUV. The change from a single-cap state towards a state with two caps can be seen. The final phase distribution is indistinguishable from the solution observed, when a random configuration was used as a starting point, as in Figure 3.38

shaped GUV, when the energy is minimized. This points to the explanation, that the two-capped state might be a local minimum, that is preferred, when line-tension is lower, or temperature is higher. This indicates that a two-capped state is entropy driven.

3.5.1 Simulating domain distribution on reconstructed vesicles on lines shows cap formation

In the next step I used the simulation developed before to compute the phase distribution on shapes of adherent, deformed vesicles, as presented in section 3.4.3. This should give indication,whether line-tension driven organization of domains on phase separated vesicles can explain the cap-formation found earlier. For this I reconstructed the GUV shape from a confocal z-stack to generate a triangulated surface representing the adherent GUV. The triangulated surface can the be used in the Monte Carlo simulations, to investigate line tension governed phase separation on adherent GUVs theoretically. In collaboration with Yannik A. Dreher, I reconstructed the shape of an adherent GUV using the open source software package GeoV to generate the triangulated surface (Figure 3.42)[118]. For the reconstruction, a GUV that was not phase separated was used, as the algorithm of GeoV did not yield good results, when two different dyes were present in the GUV membrane, due to differences in brightness, as well as artifacts from the z-stack acquisition. For the reconstruction only the membrane channel (Figure 3.42**a**) was used. The reconstructed and triangulated vesicle is shown in Figure 3.42**b**. The triangulated mesh obtained for the GUV was then used for the simulations of the domain distributions of the phase separated GUV.

As before, the majority phase, shown in magenta covered 75 % of the GUV surface, the minority phase (green) 25 %. The GUV size was scaled, that the surface area is equal

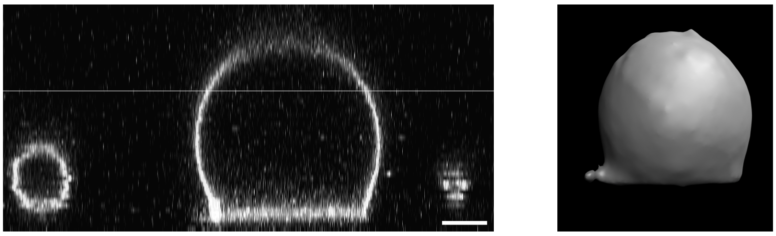

(**a**) Xz cut along the adhesive line through the adherent GUV

(**b**) Render of reconstructed GUV.

Figure 3.42: The shape of a GUV adherent on a 15 µm line was reconstructed using GeoV[118]. In a, the GUV membrane is labeled using Atto488. The scale bar is 5 µm. The software packag uses confocal z-stacks of the membrane stain of a GUV to reconstruct its shape into a triangulated surface to be used in the simulations. A render of the resulting triangulated mesh is shown in **b**.

to the area of a spherical GUV with a diameter of 10 µm (314.16 μm^2). Since up and downscaling affects the lengths over which the line energy is calculated, it is reasonable to keep the surface area consistent, to allow for better comparability of various geometries. The results of the simulations using values of σ from 0.1 - 0.5 pN are shown in Figure 3.43, where the average phase distribution throughout the $5x10^8$ iterations is shown. While for σ = 0.01 pN the distribution of the phases seems uniform on the GUV. When the line-tension is increased to 0.02 pN, the minority phase accumulates at the top of the GUV, comparable to the experimental results (Figure 3.43).

I want to remind at this point, that only geometric contributions to the phase organization are considered, and thus, organization effects of the interaction of biotin with the streptavidin pattern are not included in the simulation. The effect of the Biotin-rich phase accumulating in the micropatterned area, as shown in section 3.4.2, is therefore not expected to be found in our simulation results shown in section 3.4.3.

The minority phase is localized at the top of the GUV for all line tension values for σ from 0.02 - 0.05 pN. A change in the domain distribution depending on the line tension value, as observed in the simulations for the rod-shaped GUVs is not observed. The simulation results obtained for the deformed GUV adherent on a line show only a single, roughly circular domain on top of the GUV. A circular shape is the optimal domain shape found for a small domain of the minority phase, embedded in a large domain of the majority phase on spherical GUVs, as seen in Figure 3.35. This leads to the conclusion, that the single cap observed for adherent GUVs might be also the thermodynamic minimum. The observation, that the minority phase cap localizing on top of the GUV was found for such a wide range of line-tension values also explains why it was found so readily in the experiments presented before. It further explains, that both phases were found in the cap region, as the minority phase tends to accumulate there.

In this chapter, I have implemented a Monte Carlo simulation to investigate line tension based organization of domains in phase separated GUVs. I show, that the phase organization in rod-shaped GUVs confined in microfluidic channels found experimentally, can indeed be attributed to line-tension. Further, I can conclude, that line-tension is sufficient to explain the cap-formation in adherent GUVs. The large range of line tension values, from 0.01 to 0.05 pN, that produces these capped GUVs in simulations might explain, that this state is thermodynamically stable, and thus expected to appear often.

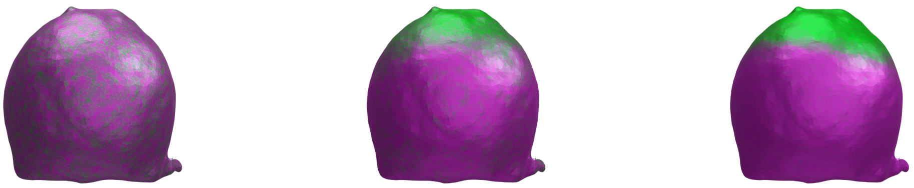

(a) σ = 0.01 pN **(b)** σ = 0.02 pN **(c)** σ = 0.03 pN

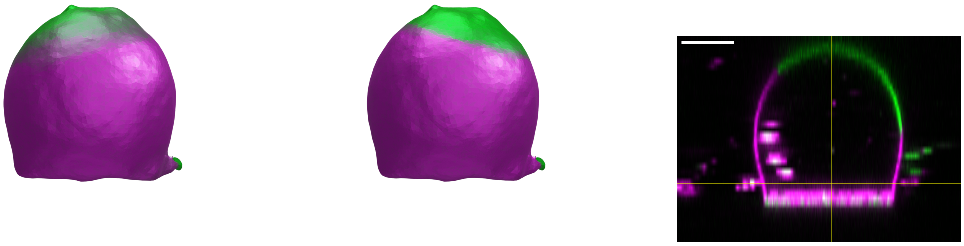

(d) σ = 0.04 pN **(e)** σ = 0.05 pN **(f)** xz cut through an adherent, phase separated GUV.

Figure 3.43: Monte Carlo simulations of domain distribution on the shape of an adherent GUV. Shown is the average phase distribution throughout the simulation of $5x10^8$ iterations **(a-e)**. In **f)** the phase distribution of an experimentally observed vesicle is shown. One can see the very similar distribution of the phase at the top region of the GUV. Scale bar is 5 µm

4 Discussion and Outlook

In the scope of this work, I set out to engineer polarity inside of bottom-up synthetic cells. I used GUVs as model systems for natural cells and adhered them to micropatterned surfaces where they deformed in dependence of the underlying pattern shape. This lead to the organization of bundled actin networks encapsulated into these synthetic cells. Further, by assembling minimal actin cortices at the GUV membrane, we showed that deformability of the GUVs was decreased, which resembles the elastic short-term behavior of actin cortices in living cells. Using phase separated membranes, I showed that lipid domains can be localized upon adhesion and deformation and, based on Monte Carlo simulations, explained this effect to be line-tension driven.

4.1 Summary of the experimental results

In this work, I presented the usage of micropatterning as a tool in bottom-up synthetic cell research to adhere and deform GUVs with the aim of inducing polarity. For this purpose, I used the established technique of micropatterning and applied it to adhere GUVs. To this end I functionalized micropatterned surfaces with streptavidin and added GUVs with biotinylated lipids. This lead to adherent, deformed GUVs that resemble the shape of adherent cells, with the geometry depending on the underlying pattern shape. In the next step, I quantified the deformation on line-shaped micropatterns with a size of 15x2 µm. GUVs with sizes comparable to the pattern size showed the strongest deformation and the highest aspect ratio, while GUVs that were smaller or larger than the pattern deformed less when adhered.

GUVs deform in dependence of the underlying micropattern into shapes that are comparable to living cells, which polarize due to these geometrical cues. One hallmark of cell polarization is the organization of the actin cytoskeleton. In GUVs, the deformation allowed for the organization of actin that was bundled by fascin inside of GUVs due to geometric constraints. I used SirActin to stain the actin filaments after GUV formation. The actin bundle orientation was analyzed in deformed GUVs, to show that they align along the major axis in GUVs that are adhered on stripe shaped pattern, while adhering GUVs on cross and crossbow patterns did induce any preference in the actin orientation. A simple simulation in 2D, assuming actin filaments to behave as straight rods that are confined in the outline of a deformed GUV predicted the experimentally observed preference in actin orientation. These results were published in Fink et al.[29].

Further, synthetic actin-cortex like structures induced through macromolecular crowding inhibited the deformation of GUVs adhering on micro patterns as well as in RTDC experiments. To this end, we exploited the volume-exclusion effects of crowders to organize actin filaments into bundles along the GUV membrane. When adhered to micropatterns, the actin bundles organized in spirals around the pattern, to avoid crossing the high curvature region at the adhesion site. Further, we showed that deformation was inhibited when both, crowders and actin was present inside of GUVs, indicating an increase of GUV stiffness due to the actin organization at the membrane. These results were confirmed in RTDC experiments, that showed an increase in stiffness of a large part in the GUV population. This is especially remarkable, as most GUV studies are done in a microscopy based low-throughput fashion, on a selected sample of GUVs.

In the last step, I employed phase separated vesicles as model systems for polarity. Phases can be functionalized independently and be used as a scaffold to induce asymmetry into the molecular distribution in the membrane of synthetic cells. I adapted the emulsion transfer protocol to allow for the incorporation of sufficient cholesterol to generate phase separated vesicles. I showed, that the phase distribution in adherent vesicles is influenced by the interaction with the adhesive pattern, as well as geometric constrains that induce a cap of the minority phase at the top of adherent GUVs. Using Monte-Carlo simulations, I show, that the cap formation can be explained by line-tension between the two phases and can thus explain domain organization in vesicle shapes obtained by deformation on adhesive micropatterns, as well due to confinement in microfluidic channels.

In the following section I will discuss the results in greater detail.

4.1.1 Adhering and deforming GUVs on micropatterned surfaces

In the first step I adhered GUVs to micropatterned surfaces. The micropatterns were produced using maskless photo lithography, which is a tool that allows for the rapid development of various patterns. The so generated patterns were functionalized with streptavidin by non-specific interactions. I verified the functionality by using fluorescently labeled streptavidin, visualizing the pattern, as well as biotin functionalized with a fluorophore to prove the capability of the patterned streptavidin to bind biotin. Biotin and streptavidin were chosen, as the binding is one of the strongest non-covalent protein-ligand interactions, and biotinylated lipids are commercially available, allowing for a simple functionalization of the GUV membrane[123].

To form GUVs, the emulsion transfer method was chosen, as it allowed the encapsulation of proteins like actin with high efficiencies, while using low amounts of proteins. The inclusion of most phospholipids is straight-forward, by mixing the desired lipid composition into the oil, and thus allowed for the inclusion of biotinylated lipids.

When GUVs were added on the micropatterned surfaces, they adhered and deformed according to the underlying pattern. Previously, mainly microfluidic based approaches to deform vesicles were employed[86]. The here presented usage of micropatterning allows for high throughput, as each surface contained several thousand micropatterns. Further, different micropatterns can be patterned on a single surface, thus allowing the usage of various patterns in a single sample. Together with the ease of creating various patterns using the maskless photolithography method, it allowed for a very fast development and testing of various patterns at the same time. The choice to use lines with the dimensions of 15x2 µm was made, because GUVs appeared to adhere and deform readily on this pattern size. When the deformation in relation to GUV size is observed (compare Figure 3.9), GUVs with sizes similar to the pattern size deform strongest. Experiments for the conceptually similar cDICE GUV formation method indicate an average size of 12 µm for GUVs, which would be in a similar size range as 15 µm long stripes[70].

The GUV deformation on adhesive micropattern is strongest at a distance close to the pattern. With larger distances, the GUV outline becomes almost circular again (compare the different z-slices in Figure 3.5). Thus, deformation was quantified by calculating the aspect ratio 2 µm above the surface. Using GeoV, a reconstruction of the 3D shape of an adherent GUV was possible[118]. These could be analyzed in the future in more detail, as information such as enclosed volume, as well as surface area and curvature is accessible from the reconstructed mesh. It would further allow for the comparison with simulated GUV shapes on adhesive surfaces, using gradient descent methods to minimize the vesicle energy, given by the Helfrich Hamiltonian[148].

All in all, I showed that GUVs are deformed by adhesion on various micropattern, which enables studies that use the same means and geometries to induce deformation in natural cells. I further quantified the deformation on line shaped micropattern, and demonstrated, that the pattern size needs to be similar to the GUV size to induce the strongest deformation.

4.1.2 Actin organization in deformed GUVs

In the next step, I investigated the organization of actin bundles in GUVs that were deformed by adhesion to micropatterned surfaces. To this end, actin was bundled using fascin, which yields straight actin bundles that resemble the shape of actin stress fibers[79]. Actin was stained using SIR-actin, an actin stain that is commonly used in live-cell imaging, but is not often used in GUV research. It is advantageous to labeled actin monomers, as it only interacts with filamentous actin. There is a risk of the dye changing actin dynamics due to its preferred binding to filaments, but this was not of great concern here, since I treated actin bundles as rigid rods and did not analyze actin dynamics.

The most notable change was the preference in angular orientation of actin bundles along the major axis in GUVs deformed on stripes (see Figure 3.12**a**). Since the deformation is strongest close to the adhesion site, the geometrical effects on actin organization are therefore expected to be highest close to the micropatterned surface. The filament orientation was analyzed by tracing stained bundles 2 µm above the surface using the software package SOAX, which is developed to quantify biopolymer networks[134]. In GUVs adhered to line shaped micropattern, a preference in the orientation of the actin bundles along the major axis was found. In GUVs adhering to cross, or crossbow pattern on the other hand, the actin orientation appeared uniform. Simulations using the outline of an adherent GUVs demonstrated, that for the cross and crossbow pattern only actin filaments with a length higher than 0.85x the major axis length are expected to show a preference in the angular orientation, while for the line-shaped micropattern, even actin filaments with 0.65x length of the major axis showed a non-uniform angular orientation (see Figure 3.18). This explains that in experimental results only for GUVs adhering to lines the angular orientation showed a strong preference, as actin bundles have various lengths.

From there I utilized crowders to localize and bundle actin filaments at the GUV membrane, yielding a cortex-like structure. It was shown, that actin bundles organize along the adhesion site, such that they avoid crossing the interface between the free membrane and the adherent part of the GUV. This leads to spiraling actin patterns, with the center localized at the adhesion site. While non-adherent GUVs show similar vortices, they are not localized to a particular point due to their spherical geometry. The actin organization found in the adherent GUVs resembles actin patterns found in natural cells[149]. It should be noted that the effects causing the actin organization in natural cells are much more complex than the pure geometric effects at play in the here presented GUVs. In natural cells, actin behavior is modulated by many additional proteins, that strongly influence the structures build with actin filaments, as well as their spatial organization. Thus, similarities should be looked at with care, keeping in mind, that the origin of the actin organization is likely very different. Generally, the micropattern shape did not seem to have an influence onto the actin bundle organization. It would be interesting though, if chiral micropatterns could be used to induce spiraling actin patterns that reflect the chirality of the micropatterned surface. This might lead to a deeper insight into the minimal set of requirements necessary to induce such patterns in synthetic cells.

The deformability of GUVs with a synthetic actin cortex, adhered to line-shaped micropattern is significantly reduced compared to empty GUVs. We show, that this results from to the interplay of actin and crowders, where only the encapsulation of both components together resulted in a decrease in deformability, compared to empty GUVs without crowders or actin. These findings were further confirmed by RTDC measurements, that showed a significant decrease in the GUV deformability when both, actin and dextran was encapsulated into the GUVs. I want to point out, that RTDC measurements show changes in the deformability in the whole GUV population, as the number of GUVs analyzed is much bigger, than in the microscopy based assays, increasing the robustness of the findings. As suggested for the analysis of deformation of empty GUVs, the analysis of the deformation of GUVs with a synthetic actin cortex could be improved from reconstructing the three dimensional vesicle shape using GeoV. This would allow to compare curvatures of the GUV membrane in 3D on various patterns, and could give deeper insights into the factors that play a role in the increase of stiffness, such as size or pattern shape.

The organization of actin filaments due to the deformation of the GUVs might open up simple ways to induce polarity, for example by functionalizing the ends of the actin bundles, to concentrate molecules at the poles of the major axis in GUVs adhered on lines. The increase in stiffness may also play an important role when interfacing synthetic and natural cells in hybrid systems in the future. While the GUV membrane can easily be functionalized with various proteins via the interaction of Ni^{2+}-NTA with poly-histidine tagged, recombinant proteins, the mechanical properties are often important for signalling in natural cells. Using such synthetic actin cortices might open the door to incorporate synthetic cells into clusters or even organoids of natural cells[150].

4.1.3 Adhesion and deformation guide domain organization

To observe adhesion-guided domain organization in phase separated vesicles, I first optimized the emulsion-transfer protocol to yield phase separated vesicles. While the generation of phase-separated vesicles using the emulsion-transfer method has been reported in the past, further optimizations were necessary to give phase separated GUVs in sufficient quantities[72]. Based on results published for the conceptionally similar cDICE method, the main changes were a drastic increase in the amounts of cholesterol dissolved into the oil, as well as the change from mineral oil to silicone oil. When mineral oil was used, no phase separated vesicles were observed, even when increased cholesterol portions of up to 80 Mol% were used. When the oil-layer was switched to silicone oil a major part of the GUVs formed were phase separated (See section 3.4.1). This is explained, because cholesterol dissolves better in mineral oil than in silicone oil and thus partitions in lower quantities into the vesicles when mineral oil is used[71]. While this drawback of mineral oil could potentially be compensated by increasing the cholesterol amount even further, I instead decided to change the oil phase to silicone oil. I did not observe problems that arose from the change of the oil when it came to encapsulation of cargo, although vesicles created with silicone oil showed a higher amount of defects, such as smaller vesicles or oil droplets encapsulated into the vesicle lumen, as well as lipid remnants sticking to the vesicle. On the other side, GUV formation with silicone oil seemed to increase GUV yield. Since the emulsion transfer method allows for the encapsulation of various cargo, it makes the method valuable for future work towards the generation of synthetic cells, which are going to depend on the incorporation of functional modules into the synthetic cells.

I showed that domains in phase separated GUVs can be organized by adhesion to micropatterned surfaces. Domain organization due to the interaction of lipids with various interfaces been reported before, as well as described theoretically for microstructured surfaces[151–154]. I showed qualitatively a dependence on streptavidin concentration via defects in the coating in line micropatterns (See section 3.4.2). This observation is in line with the hypothesis that the local concentration of biotinylated lipids increases due to the interaction with the micropattern and thus leads to a localization of the Lo phase, which is preferred by the biotin-PEG2k-DSPE lipid utilized here. I want to mention, that the concentration of this lipid in the membrane is 1 Mol%, and thus, even if enriched at the surface is expected to account for a small molar percentage of the total lipid concentration. This is remarkable, as such a small change in concentration can drive the Lo phase to localize at the adhesion site. Utilizing compositions with various amounts of biotinylated lipids might allow to utilize this effect stronger, as the difference in local concentration between the adhesion site and the free standing GUV membrane could be tuned more finely.

Noteworthy was the localization of a domain over time periods of several minutes to several days at the top of vesicles adhering on stripe-shaped micropattern, leading to a cap of the minority phase at the top of the GUV (Described in section 3.4.3). Further, the peeling of an adherent GUV after irradiation with a laser during confocal image acquisition showed the immediate change from an organized state, where the Ld domain localized at the ends of the line pattern to a single domain on a spherical GUV when the GUV was no longer adhered. Several factors were hypothesized for the puzzling observation of the domain organization into a cap in adherent GUVs, such as preference in membrane-curvature of one phase or line-tension. A preference in membrane-curvature of one phase seemed a plausible explanation at first, assuming the bending rigidity of Lo phase and Ld phase differs. I observed both phases in the cap of the GUVs, hinting towards a different explanation. If membrane curvature would be the driving force, the same phase would be expected to localize in the cap in all cases. The spontaneous curvature of the membrane of each phase is expected to be zero, as the GUV membrane is symmetric, when obtained with the emulsion transfer employing two identical oil solutions for the outside and inside leaflet. This excludes spontaneous curvature to be a factor in the here observed domain organization. Nakazawa et. al. pointed at line-tension being the driving factor for the organization of domains of phase separated GUVs in microfluidic confinements (See section 3.5). They also observed, that the organization did not seem to be dependent on curvature, as the minority phase in their GUVs seemed to localize at the caps of the GUVs, independent ob it being the Lo or Ld phase[100]. Therefore the hypothesis that the organization of the phases due to geometrical effects seemed plausible, although it could not simply be explained by a minimization of the line energy in the case of GUVs confined in microfluidic chanels[100].

To understand this phenomenon, I implemented a Monte-Carlo simulation to determine, whether line-tension would be sufficient to explain the domain organization found in the experiments pubished by Nakazawa et. al. in microfluidic confinements, as well as the cap-formation in the adherent GUVs observed in chapter 3.4.3[100].

I employed a Monte Carlo simulation to explore the configuration space of domain organization, as the total number of states possible is too high to reasonably compute completely. The reconstructed GUVs on lines are made up of over 17000 triangles. In the simulations, I assume, the minority phase has an occupancy of 25 %, so 4250 of the 17000 triangles. The total number of states can be obtained by computing $\binom{N}{k}$, where N is the total number of triangles and k the number of triangles occupied by one phase, yielding $\binom{17000}{4250} = 3.7x10^{4150}$ possible states and thus impractical to compute. At first, I tried to minimize the energy in a gradient descent based approach where the transition to a psoposed state was only allowed, if the energy of the newly generated trial state was lower than the current state. This lead to the case, where no single exchange of two triangle phases would yield a lower energy resulting in a frozen simulation that stopped evolving. This direct energy minimization was therefore changed to a Monte Carlo based approach, that allows for an increase in energy with a non-zero probability, dependent on the energy difference and temperature, which lead to the results presented in this work, that reproduced the experimental observations.

In the first step, I showed that for a phase separated, spherical vesicle the resulting state is a single minority phase domain surrounded by the majority domain, as expected from simulations and experimental results published before[113]. Then I used the rod-shaped GUVs in microfluidic confinements as their shape can be described by a cylinder that is capped by two half-spheres at both ends. This simplified the verification of the implemented equations. I was able to observe a cap-formation on both ends, as shown experimentally by Nakazawa et al. for the confined GUVs for line tension values of 0.03 pN and lower in the simulations, as well as the expected single cap for higher values[100]. This shows that line-tension is sufficient to explain the experimental results of domain organization in rod-shaped GUVs. In the next step, we used the reconstructed shape of an adherent vesicle on a line to simulate the domain organization of deformed GUVs. There I found that the cap formation can be explained by line-tension too, leading to the minority phase localizing at the GUV top for a wide range in line-tension values, from 0.02 pN to 0.05 pN (See Figure 3.43). Since only geometric effects were considered in the simulations, the localization of a phase at the adhesion site was not observed. In the future, this simulation could be also applied to other GUV shapes, such as GUVs adhered to cross and crossbow pattern, potentially to investigate the effect of the shape on domain localization. Further, mixtures with more than two phases could easily be added in the simulations, expanding the effects that could be explored. The line tension values employed in the simulations were around two orders of magnitude smaller than reported experimental values. When the energy differences between two states becomes too high due to increased line-tension values, the probability of accepting a new trial state decreases very fast. Further, the two-capped configurations were only observed in a narrow window of values for the line-tension around 0.03 pN. This might indicate, that, in experimental setups other factors play an important role as well, that counter the line-energy driven effects. The line tension values utilized in the here presented simulations are in the same range as used in Monte Carlo simulations published before[113].

I showed in the simulations of GUVs adhering to line shaped micropatterns that the minority phase localized at the top of the GUV. As the Lo phase is drawn to the micropattern the concentration of the remaining Lo phase in the free part of the GUV would be reduced. Therefore, if the phases are equally distributed in the free floating GUV, a preference of the Lo cap should be seen due to the reduction of the phase in the free part of the GUV from the interaction with the micropattern. Controlling the parts of each phase by changing the lipid composition might open another way to control the phase localizing at the adhesion site, independently of the cap formed at the top. Since the simulation is based on computing the phase behavior on triangulated shapes, additional energy contributions, such as bending energy, as well as spontaneous curvature could be added, as the local curvature can easily be calculated on triangulated meshes[113,155,156]. This could aid in the understanding of other factors that play a role in domain organization and their response to geometrical cues, as well as simulate more complex lipid mixtures.

4.2 Outlook

All in all, the results presented in this work were based on using geometrical cues to affect the distribution and organization of molecules such as actin, as well as domains in phase separated membranes. In the following section, I want to give an outlook on alternative ways to functionalize the, throughout this work extensively used micropattern, such as DNA nanotechnology. I further want to shed light on other potential approaches to induce polarity in synthetic cells. While spontaneous emergence of polarity and organization, as observed for reaction diffusion systems like the minCDE system may be desired to polarize synthetic cells, using external signals and direct manipulation of molecular organization might provide more robust ways to implement and debug systems that depend on a polar molecular organization. I will shortly present the potential use of magnetic nanoparticles to manipulate molecules bound to the particles. Last, I will discuss the potential use of phase separated vesicles as scaffolds to organize transmembrane and membrane bound proteins. I expect the usage of micropatterns to direct the phases will provide additional value, as it gives access to a controlled and reproducible environment, that allows for a defined and long lasting molecular organization over long periods of time.

4.2.1 DNA-mediated GUV adhesion

To further show the versatility of the micropatterning approach, DNA mediated adhesion was implemented to be used in potential further developments and applications. The in this section shown data was obtained together with Duc Thien Bui, during an internship under my supervision. DNA has been used in the past to mediate cell-cell interactions, as well as adhere DNA origami to GUVs, as it allows for a fine control of the interaction strength[157,158]. To bind DNA oligomers to membranes, cholesterol tagged DNA is often employed, as it self-inserts into the lipid membrane,and thus provides a simple way to functionalize GUVs with DNA strands[159,160]. A common way to verify the successful functionalization with DNA oligomers is to bind a fluorescently tagged counter-strand to see, whether the fluorescence signal localizes in the expected areas.

In Figure 4.1 I show the successful incorporation of cholesterol tagged DNA oligomers into the GUV membrane. GUVs were incubated with fluorescent Cy5-polyA DNA with (Figure 4.1**b**) and without poly-T cholesterol (Figure 4.1**a**). The GUVs were not fluorescently labeled to ensure no crosstalk between fluorophores was observed. It can be seen, that the Cy5-poly-A DNA can only bind, when the GUV is functionalized with a cholesterol tagged poly-T DNA strand.

Next, the functionalization of streptavidin coated micropattern with biotinylated 20-A-

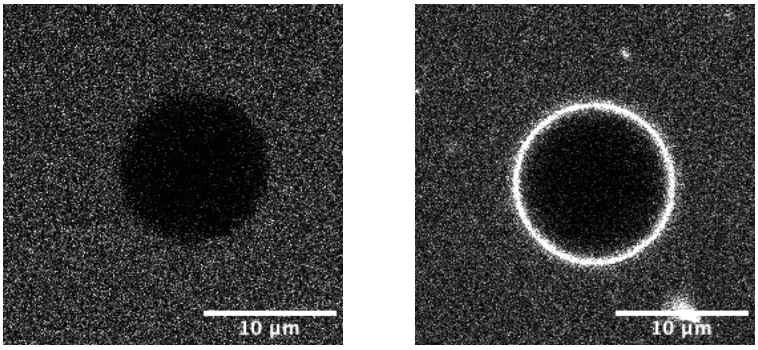

(a) GUV in the absence of 20T-cholesterol.

(b) GUV functionalized 20-T-cholesterol.

Figure 4.1: Cy5 functionalized 20-A DNA does not interact with GUVs in the absence of a cholesterol tag **(a)**. The signal outside of the GUV stems from unbound Atto647n-polyT DNA. When cholesterol tagged poly-T DNA is provided, the Cy5-poly-A DNA strand can bind **(b)**.

DNA oligomers was confirmed. The successful functionalization of the surface was demonstrated by letting the biotinylated DNA interact with a fluorescently labeled counter strand. In the control experiment, when no biotinylated DNA strand is added, no interaction of the fluorescent counterstrand is observed (See Figure 4.2**a**). In the presence of the biotinylated 20-A oligomer, the fluorescent 20-T counter-strand binds to the pattern, showing the successful DNA functionalization of the micropattern (Figure 4.2**b**).

With this, the adhesion of GUVs was straightforward. An example is shown in Figure 4.3. The GUV membrane (magenta), functionalized with 20-T-cholesterol is shown 2 µm above the streptavidin micropattern (cyan), coated with 20-A biotin. There, it is visible that GUVs adhere and deform when adhered to micropatterned surfaces using DNA nanotechnology. We can thus conclude, that the DNA mediated adhesion of GUVs is possible. Quantitative analysis could provide data in the future of the impact linker-strength, as this is tuneable by changing the sequence and length of the DNA oligomers. It might further provide ways to study the interaction of natural cells and GUVs using DNA nanotechnology as GUVs can be functionalized with DNA in the similar ways, that natural cells can[161,162]. As these systems can be tuned to be orthogonal to existing signaling cascades, the behavior of adhered cells and GUVs can be observed and compared in a more direct manner.

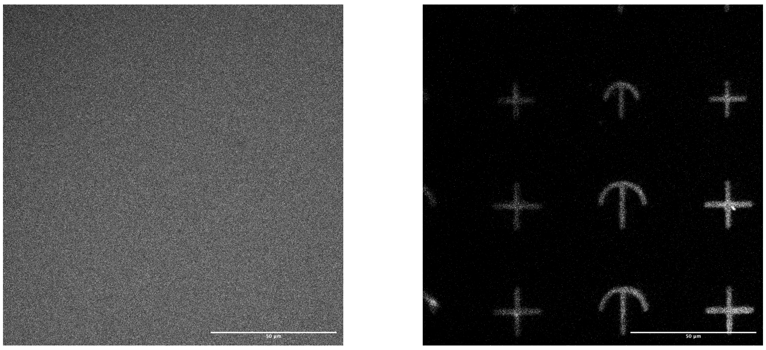

(a) Cy5 functionalized 20-T DNA does not bind to the micropatterns in the absence of 20-A-biotin.

(b) Cy5 functionalized 20-T DNA binds the streptavidin coated surface in the presence of 20-A-biotin.

Figure 4.2: Validation of DNA functionalized micropatterned surfaces. In **a**, no binding of DNA oligos is observed in the absence of a biotinylated strand interacting with the streptavidin. Shown is a confocal image of DNA binding to the micropatterned surface, where fluorescently labeled Cy5-polyT DNA can only bind in the presence of a biotinylated counter strand **(b)**.

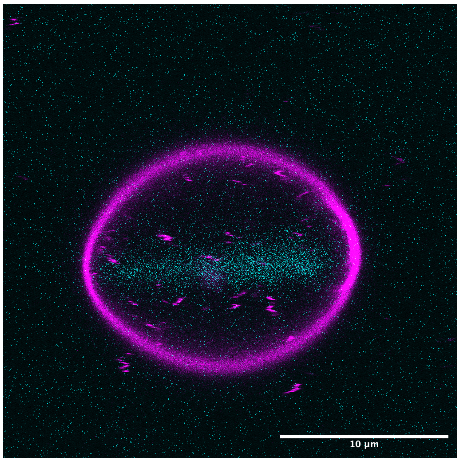

Figure 4.3: Example of a GUV adhering to a 15 µm long stripe pattern. The pattern was functionalized with fluorescent streptavidin (cyan) to which a 20-A biotinylated DNA oligomere was added and is shown at the z-slice of the highest intensity. The GUV is functionalized using 20-T cholesterol tagged counter strand and is shown in magenta 2 µm above the pattern. One can see the GUV deforming due to the underlying pattern.

4.2.2 Inducing asymmetry using magnetic nanoparticles

A different approach to introduce asymmetric protein concentrations inside a GUV could be the direct linkage of magnetic nanoparticles to the proteins. With that, functional molecules inside the synthetic cell could be manipulated spatially localized, where the local concentration is be dependent on the magnetic force. Similar approaches have been used in natural cells, where magnetic nanoparticles can lead to novel functionalities[163]. The successful encapsulation of magnetic nanoparticles into GUVs using the emulsion transfer method is shown in Figure 4.4**a**, where the magnetic nanoparticles are homogeneously distributed inside the GUV. Through the force induced by the magnet from below, the GUV moves towards the magnet. Further, the localization of nanoparticles at the bottom of the GUV can be observed, when a magnet is added (See Figure 4.4**b**). If the localzation of proteins using magnetic forces is desired, the GUVs should thus be immobilized. This could potentially be done by adhesion to micropatterned surfaces, as presented throughout this work.

Additionally, to further harness the capabilities of phase separated vesicles one could bind magnetic nanoparticles to one phase, for example via the DNA-linkage presented before or the interaction of biotin and streptavidin, and modulate the phase organization by direct stimuli with magnetic fields from the outside. Magnet based systems have the opportunity of changing the magnetic field applied in a time-dependent manner, and thus control and change the organization independently, or in combination with additional cues, such as ahesion and geometry.

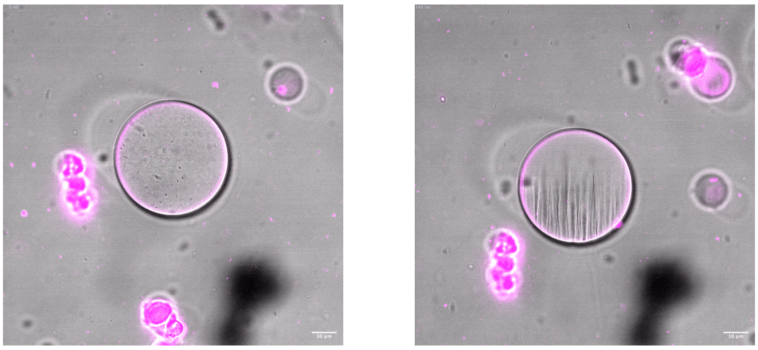

(a) No magnet **(b)** Magnet from below

Figure 4.4: Emulsion transfer allows for the encapsulation of magnetic nanoparticles. The confocal image of the membrane is shown in magenta. Additionally, to visualize the nanoparticles, the brightfield image is shown. In **(a)**, the homogenous distribution of the nanoparticles can be seen in the absence of a magnet. The nanoparticles are localized at the bottom of the GUV, when a magnet is added close to the well from the bottom **(b)** Scale bar is 10 µm

4.2.3 Phase separated membranes as scaffolds for synthetic cell polarity

I have shown that adhering and deforming vesicles on micropatterned surfaces can be done reliably in large scales. The adhesion drives domain organization of phase separated vesicles directly, through interaction with the micropattern, as well as through geometrical cues. In the future, this domain organization might be harnessed to drive protein organization. It has been shown before that functionalized lipids, such as Ni^{2+}-NTA tagged phospholipids that phase separate into one phase, can be used to localize poly-His tagged proteins at the single phase at the membrane. The phase a protein is linked to could be further tuned by using various phospholipids[71]. Thus, phase separated vesicles where the domain organization is guided by deformation, might be used as scaffolds in the future to drive protein organization in controlled ways. This might give easy strategies to induce polarity in GUVs and synthetic cells. One issue can be the low energy barrier to disturb domains in comparison to the energy to, for example, move actin filaments. It has been shown for supported lipid bilayers, that actin can move and organize the lipid domains, and did not appear to be moved by the underlying phase separation[103]. I have observed similar effects, where demixing and macroscopic domain formation in phase separated vesicles seemed inhibited by actin filaments polymerized at the inside of GUVs. This might be mitigated by utilizing lipid mixtures that have high line tension values. Further, acoustic manipulation and demixing of phase separating SLBs has been reported before, and could be used together with GUVs adhered to adhesive micropatterns[164]. Additionally, phase separated vesicles allow for protein organization also in equilibrium, and might thus allow to circumvent more complex reaction-diffusion systems to obtain polarized systems, that are sensitive to the vesicle geometry. Although it should be noted that macroscopic phase separation is not utilized for building polarity in natural cells, it does not hinder us to use such systems to engineer polarity into synthetic cells. Further, the here presented work helps in understanding the influence of geometric cues on domain organization, and in return might aid in the rational design of synthetic cells in the future.

4.3 Conclusion

In this work, I set out to establish polarity inside bottom-up synthetic cells using external cues, here micropatterned surfaces, that induce GUV deformation upon adhesion.

In the scope of this work, I showed that GUVs can be adhered to micropatterned surfaces in a manner comparable to living cells. While I did not use ECM proteins to induce synthetic cell adhesion to the micropatterns, as they would require additional specialized proteins that mediate the interaction, such as integrins, I presented an approach optimized for synthetic cells that is based on the interaction of biotin and streptavidin. I demonstrated, that GUVs can efficiently be deformed when adhering to various micropatterned shapes and quantified the deformation for GUVs on line-shaped pattern. Here, it was apparent that the pattern size has to be comparable to the GUV size to induce strong deformation.The usage of micropatterning can be extended from streptavidin and biotin mediating the adhesion, to alternative technologies that offer more ways of customization, such as DNA nanotechnology. The deformation of GUVs induces alteration in the organization of actin bundles inside of GUVs. This was observed for straight actin fibers that were bundled with fascin, that mimic actin stress fibers in natural cells, as well as for bundles induced by molecular crowding that accumulated in a cortex-like fashion at the GUV periphery. These synthetic cortices further inhibited deformation of GUVs, imitating the elastic short-term behavior of natural cells. The increased stiffness is a feature that could be exploited further in future applications, for example GUVs interacting with cells, as cells can sense and react to mechanical cues. Last, I showed that domains in phase separated GUVs can be guided by adhesion and deformation in a correlated fashion. While the organization induced by adhesion can be explained by an increase in the local concentration of biotinylated lipids that favor the Lo phase at the micropattern interface, the domain localization induced by deformation appears to be driven by line-tension. Using Monte Carlo simulations, i demonstrated that line-energy contributions are sufficient to explain organization of domains in phase separated vesicles, adhering to line micropatterns. These simulations can contribute to the rational design of bottom-up synthetic systems, guiding future experimental investigations. In the future lipid mixtures characterized by elevated line tensions between the Lo and Ld domains could be used, as well as investigating the impact of different vesicle geometries.

Altogether, I have shown various ways to organize molecules and proteins in GUVs in a controlled fashion by adhesion to micropatterned surfaces, which is a first step towards cell polarity. While it is still a long way to implement functional parts of living systems from the bottom-up, this work lays the foundation to induce polarity into GUVs. In the future deforming vesicles on micropatterns to guide molecular organization could aid in building controlled, polar systems, that mimic parts, or even complete functional living cells, from the bottom up.

5 Appendix

5.1 List of abbrevations

PLL	poly-L-lysine
DOPC	1,2-Dioleoyl-sn-glycero-3-phosphocholine
DPPC	1,2-dipalmitoyl-sn-glycero-3-phosphocholine
DOPG	1,2-dioleoyl-sn-glycero-3-phospho-(1’-rac-glycerol) (sodium salt)
Chol	cholesterol
Tf-Chol	top-fluor cholesterol
GUV	Giant unilamellar vesicle
PEG	Polyethylenglycol
PEG-SVA	PEG-bis-Succinimidyl Valerate
PLPP-gel	4-benzoylbenzyl-trimethylammonium chloride
BSA	Bovine serum albumin
DNA	Deoxyribonucleic acid
RNA	Ribonucleic acid
NTA	Nitrilotriacetic
Oligo	Oligomer
Ld	Liquid disordered
Lo	Liquid ordered
Af405	Alex Fluor 405
LissRhodPE	1,2-dioleoyl-sn-glycero-3-phosphoethanolamine-N-(lissamine rhodamine B sulfonyl)
ECM	Extracellular matrix
SD	Standard deviation

5.2 List of publications

These publications were authored and co-authored by me during my PhD work:

Fink, A. *et al.* Extracellular Cues Govern Shape and Cytoskeletal Organization in Giant Unilamellar Lipid Vesicles. *ACS Synthetic Biology* **12,** 369–374 (2023)

Dreher, Y. *et al.* GeoV: An Open-Source Software Package for Quantitative Image Analysis of 3D Vesicle Morphologies. *Advanced Intelligent Systems* **5,** 2300170 (2023)

Yagüe Relimpio, A. *et al.* Bottom-up Assembled Synthetic SARS-CoV-2 Miniviruses Reveal Lipid Membrane Affinity of Omicron Variant Spike Glycoprotein. *ACS Nano* **17,** 23913–23923 (2023)

Levario-Diaz, V. *et al.* 1D micro-nanopatterned integrin ligand surfaces for directed cell movement. *Frontiers in Cell and Developmental Biology* **10,** 972624 (2022)

6 References

1. NASA. *About Life Detection* `https://astrobiology.nasa.gov/research/life-detection/about/` (2024).
2. Benner, S. A. Defining life. *Astrobiology* **10,** 1021–1030 (2010).
3. Çengel, Y. A. Eighteen distinctive characteristics of life. *Heliyon* **9** (2023).
4. Schrödinger, E. *What is life? The physical aspect of the living cell and mind* (Cambridge university press Cambridge, 1944).
5. Schneider, E. D. & Kay, J. J. Life as a manifestation of the second law of thermodynamics. *Mathematical and computer modelling* **19,** 25–48 (1994).
6. Michaelian, K. Thermodynamic dissipation theory for the origin of life. *Earth System Dynamics* **2,** 37–51 (2011).
7. Khan, Y. S. & Farhana, A. Histology, cell (2020).
8. Harold, F. M. Molecules into cells: specifying spatial architecture. *Microbiology and molecular biology reviews* **69,** 544–564 (2005).
9. Haller, B. *et al.* Autonomous Directional Motion of Actin-Containing Cell-Sized Droplets. *Advanced Intelligent Systems* **3,** 2000190 (2021).
10. Patino-Ramirez, F., Arson, C. & Dussutour, A. Substrate and cell fusion influence on slime mold network dynamics. *Scientific reports* **11,** 1498 (2021).
11. Tsang, A. C., Lam, A. T. & Riedel-Kruse, I. H. Polygonal motion and adaptable phototaxis via flagellar beat switching in the microswimmer Euglena gracilis. *Nature Physics* **14,** 1216–1222 (2018).
12. Palma, V., Gutiérrez, M. S., Vargas, O., Parthasarathy, R. & Navarrete, P. Methods to evaluate bacterial motility and its role in bacterial–host interactions. *Microorganisms* **10,** 563 (2022).
13. Harris, A. K. Cell motility and the problem of anatomical homeostasis. *Journal of Cell Science* **1987,** 121–140 (1987).

14. Vishwakarma, M., Spatz, J. P. & Das, T. Mechanobiology of leader–follower dynamics in epithelial cell migration. *Current opinion in cell biology* **66,** 97–103 (2020).
15. Vishwakarma, M., Thurakkal, B., Spatz, J. P. & Das, T. Dynamic heterogeneity influences the leader–follower dynamics during epithelial wound closure. *Philosophical Transactions of the Royal Society B* **375,** 20190391 (2020).
16. Froese, T., Virgo, N. & Ikegami, T. Motility at the origin of life: Its characterization and a model. *Artificial life* **20,** 55–76 (2014).
17. Miyata, M. *et al.* Tree of motility–A proposed history of motility systems in the tree of life. *Genes to Cells* **25,** 6–21 (2020).
18. Verkhovsky, A. B., Svitkina, T. M. & Borisy, G. G. Self-polarization and directional motility of cytoplasm. *Current Biology* **9,** 11–20 (1999).
19. Kozlov, M. M. & Mogilner, A. Model of polarization and bistability of cell fragments. *Biophysical journal* **93,** 3811–3819 (2007).
20. Piroli, M. E., Blanchette, J. O. & Jabbarzadeh, E. Polarity as a physiological modulator of cell function. *Frontiers in bioscience (Landmark edition)* **24,** 451 (2019).
21. Vicente-Manzanares, M., Sánchez-Madrid, F., *et al.* Cell polarization: a comparative cell biology and immunological view. *Journal of Immunology Research* **7,** 51–65 (2000).
22. Leterrier, C. The axon initial segment: an updated viewpoint. *Journal of Neuroscience* **38,** 2135–2145 (2018).
23. Stanganello, E. *et al.* Wnt signaling directs neuronal polarity and axonal growth. *Iscience* **13,** 318–327 (2019).
24. Altschuler, S. J., Angenent, S. B., Wang, Y. & Wu, L. F. On the spontaneous emergence of cell polarity. *Nature* **454,** 886–889 (2008).
25. Ramm, B., Heermann, T. & Schwille, P. The E. coli MinCDE system in the regulation of protein patterns and gradients. *Cellular and Molecular Life Sciences* **76,** 4245–4273 (2019).
26. Bonny, M., Fischer-Friedrich, E., Loose, M., Schwille, P. & Kruse, K. Membrane binding of MinE allows for a comprehensive description of Min-protein pattern formation. *PLoS computational biology* **9,** e1003347 (2013).
27. Albert, P. J. & Schwarz, U. S. Modeling cell shape and dynamics on micropatterns. *Cell adhesion & migration* **10,** 516–528 (2016).
28. Théry, M. Micropatterning as a tool to decipher cell morphogenesis and functions. *Journal of cell science* **123,** 4201–4213 (2010).

29. Fink, A. *et al.* Extracellular Cues Govern Shape and Cytoskeletal Organization in Giant Unilamellar Lipid Vesicles. *ACS Synthetic Biology* **12,** 369–374 (2023).
30. Bienvenie, A. & Sainte Marie, J. by Lipids. *Cell Lipids* **40,** 319 (1994).
31. Torben-Nielsen, B., Tuyls, K. & Postma, E. O. *On the neuronal morphology-function relationship: A synthetic approach* in *International Workshop on Knowledge Discovery and Emergent Complexity in Bioinformatics* (2006), 131–144.
32. Baskurt, O. K. & Meiselman, H. J. Red blood cell mechanical stability test. *Clinical hemorheology and microcirculation* **55,** 55–62 (2013).
33. Kuchel, P. W., Cox, C. D., Daners, D., Shishmarev, D. & Galvosas, P. Surface model of the human red blood cell simulating changes in membrane curvature under strain. *Scientific Reports* **11,** 13712 (2021).
34. Adams, K. A theory for the shape of the red blood cell. *Biophysical journal* **13,** 1049–1053 (1973).
35. Mesarec, L. *et al.* Normal red blood cells' shape stabilized by membrane's in-plane ordering. *Scientific reports* **9,** 19742 (2019).
36. Nelson, W. J. Remodeling epithelial cell organization: transitions between front–rear and apical–basal polarity. *Cold Spring Harbor perspectives in biology* **1,** a000513 (2009).
37. Zhu, T., Zhu, T., Tran, K., Sivamani, R. & Shi, V. Epithelial barrier dysfunctions in atopic dermatitis: a skin–gut–lung model linking microbiome alteration and immune dysregulation. *British Journal of Dermatology* **179,** 570–581 (2018).
38. Marshall, W. F. Pattern formation and complexity in single cells. *Current Biology* **30,** R544–R552 (2020).
39. Gov, N. S., Kralj-Iglič, V., Sadhu, R. K., Mesarec, L. & Iglič, A. in *Plasma Membrane Shaping* 393–413 (Elsevier, 2023).
40. Lappalainen, P., Kotila, T., Jégou, A. & Romet-Lemonne, G. Biochemical and mechanical regulation of actin dynamics. *Nature Reviews Molecular Cell Biology* **23,** 836–852 (2022).
41. Cooper, G. M. Structure and organization of actin filaments. *The cell: a molecular approach* **2** (2000).
42. Singh, G. & Sharma, R. in *Advances in Animal Experimentation and Modeling* 195–203 (Elsevier, 2022).
43. Edwards, M. *et al.* Capping protein regulators fine-tune actin assembly dynamics. *Nature reviews Molecular cell biology* **15,** 677–689 (2014).
44. Ivanova, J. R. *et al.* Designed Ankyrin Repeat Proteins as Actin Labels of Distinct Cytoskeletal Structures in Living Cells. *ACS nano* (2024).

45. Maninova, M., Caslavsky, J. & Vomastek, T. The assembly and function of perinuclear actin cap in migrating cells. *Protoplasma* **254,** 1207–1218 (2017).
46. Tojkander, S., Gateva, G. & Lappalainen, P. Actin stress fibers–assembly, dynamics and biological roles. *Journal of cell science* **125,** 1855–1864 (2012).
47. Krause, M. & Gautreau, A. Steering cell migration: lamellipodium dynamics and the regulation of directional persistence. *Nature reviews Molecular cell biology* **15,** 577–590 (2014).
48. Barnhart, E. L., Lee, K.-C., Keren, K., Mogilner, A. & Theriot, J. A. An adhesion-dependent switch between mechanisms that determine motile cell shape. *PLoS biology* **9,** e1001059 (2011).
49. Laplaud, V. *et al.* Pinching the cortex of live cells reveals thickness instabilities caused by myosin II motors. *Science Advances* **7,** eabe3640 (2021).
50. Chugh, P. & Paluch, E. K. The actin cortex at a glance. *Journal of cell science* **131,** jcs186254 (2018).
51. Benner, S. A. & Sismour, A. M. Synthetic biology. *Nature reviews genetics* **6,** 533–543 (2005).
52. Hutchison III, C. A. *et al.* Design and synthesis of a minimal bacterial genome. *Science* **351,** aad6253 (2016).
53. Breuer, M. *et al.* Essential metabolism for a minimal cell. *Elife* **8,** e36842 (2019).
54. Rothschild, L. J. & Mancinelli, R. L. Life in extreme environments. *Nature* **409,** 1092–1101 (2001).
55. Costantini, D. & Costantini, D. Historical and contemporary issues of oxidative stress, hormesis and life-history evolution. *Oxidative Stress and Hormesis in Evolutionary Ecology and Physiology: A Marriage Between Mechanistic and Evolutionary Approaches,* 1–38 (2014).
56. Fletcher, D. A. Bottom-up biology: harnessing engineering to understand nature. *Developmental cell* **38,** 587–589 (2016).
57. Hanson, A. D. & Lorenzo, V. d. Synthetic Biology - High Time to Deliver? *ACS synthetic biology* **12,** 1579–1582 (2023).
58. Garner, K. L. Principles of synthetic biology. *Essays in biochemistry* **65,** 791–811 (2021).
59. Knappe, G. A., Wamhoff, E.-C. & Bathe, M. Functionalizing DNA origami to investigate and interact with biological systems. *Nature Reviews Materials* **8,** 123–138 (2023).
60. Thomas, I., Gaminda, K., Jayasinghe, C., Abeysinghe, D., Senthilnithy, R, *et al.* DNAzymes, novel therapeutic agents in cancer therapy: a review of concepts to applications. *Journal of Nucleic Acids* **2021** (2021).

61. Jumper, J. *et al.* Highly accurate protein structure prediction with AlphaFold. *Nature* **596,** 583–589 (2021).

62. Dimova, R. & Marques, C. *The giant vesicle book* (CRC Press, 2019).

63. Gerstle, Z., Desai, R. & Veatch, S. L. in *Methods in enzymology* 129–150 (Elsevier, 2018).

64. Snijder, B. & Pelkmans, L. Origins of regulated cell-to-cell variability. *Nature reviews Molecular cell biology* **12,** 119–125 (2011).

65. Hissa, B. *et al.* Membrane cholesterol removal changes mechanical properties of cells and induces secretion of a specific pool of lysosomes. *PloS one* **8,** e82988 (2013).

66. Walde, P., Cosentino, K., Engel, H. & Stano, P. Giant vesicles: preparations and applications. *ChemBioChem* **11,** 848–865 (2010).

67. Litschel, T. *et al.* Reconstitution of contractile actomyosin rings in vesicles. *Nature communications* **12,** 2254 (2021).

68. Kohyama, S., Merino-Salomón, A. & Schwille, P. In vitro assembly, positioning and contraction of a division ring in minimal cells. *Nature Communications* **13,** 6098 (2022).

69. Bashirzadeh, Y. *et al.* Actin crosslinker competition and sorting drive emergent GUV size-dependent actin network architecture. *Communications Biology* **4,** 1136 (2021).

70. Van de Cauter, L. *et al.* Optimized cDICE for efficient reconstitution of biological systems in giant unilamellar vesicles. *ACS Synthetic Biology* **10,** 1690–1702 (2021).

71. Dürre, K. & Bausch, A. R. Formation of phase separated vesicles by double layer cDICE. *Soft Matter* **15,** 9676–9681 (2019).

72. Karamdad, K. *et al.* Engineering thermoresponsive phase separated vesicles formed via emulsion phase transfer as a content-release platform. *Chemical Science* **9,** 4851–4858 (2018).

73. Weiss, M. *et al.* Sequential bottom-up assembly of mechanically stabilized synthetic cells by microfluidics. *Nature materials* **17,** 89–96 (2018).

74. Haller, B. *et al.* Charge-controlled microfluidic formation of lipid-based single-and multicompartment systems. *Lab on a Chip* **18,** 2665–2674 (2018).

75. Göpfrich, K. *et al.* One-pot assembly of complex giant unilamellar vesicle-based synthetic cells. *ACS synthetic biology* **8,** 937–947 (2019).

76. Hohmann, T & Dehghani, F. *The cytoskeleton-a complex interacting meshwork. Cells 8, 362* 2019.

77. Belluati, A. *et al.* Multicompartment polymer vesicles with artificial organelles for signal-triggered cascade reactions including cytoskeleton formation. *Advanced Functional Materials* **30,** 2002949 (2020).
78. Gavriljuk, K. *et al.* A self-organized synthetic morphogenic liposome responds with shape changes to local light cues. *Nature Communications* **12,** 1548 (2021).
79. Bashirzadeh, Y., Wubshet, N. H. & Liu, A. P. Confinement geometry tunes fascin-actin bundle structures and consequently the shape of a lipid bilayer vesicle. *Frontiers in molecular biosciences* **7,** 610277 (2020).
80. Dürre, K. *et al.* Capping protein-controlled actin polymerization shapes lipid membranes. *Nature communications* **9,** 1630 (2018).
81. Buddingh', B. C. & van Hest, J. C. Artificial cells: synthetic compartments with life-like functionality and adaptivity. *Accounts of chemical research* **50,** 769–777 (2017).
82. Abu Shah, E. & Keren, K. Symmetry breaking in reconstituted actin cortices. *Elife* **3,** e01433 (2014).
83. Sakamoto, R. *et al.* Tug-of-war between actomyosin-driven antagonistic forces determines the positioning symmetry in cell-sized confinement. *Nature communications* **11,** 3063 (2020).
84. Hsu, C.-P., Sciortino, A., de la Trobe, Y. A. & Bausch, A. R. Activity-induced polar patterns of filaments gliding on a sphere. *Nature communications* **13,** 2579 (2022).
85. Thalmeier, D., Halatek, J. & Frey, E. Geometry-induced protein pattern formation. *Proceedings of the National Academy of Sciences* **113,** 548–553 (2016).
86. Ganzinger, K. A. *et al.* FtsZ reorganization facilitates deformation of giant vesicles in microfluidic traps. *Angewandte Chemie International Edition* **59,** 21372–21376 (2020).
87. Wubshet, N. H. & Liu, A. P. Methods to mechanically perturb and characterize GUV-based minimal cell models. *Computational and Structural Biotechnology Journal* **21,** 550–562 (2023).
88. Jia, H. *et al.* Shaping giant membrane vesicles in 3D-printed protein hydrogel cages. *Small* **16,** 1906259 (2020).
89. Mishra, A. *et al.* Translocation of HIV TAT peptide and analogues induced by multiplexed membrane and cytoskeletal interactions. *Proceedings of the National Academy of Sciences* **108,** 16883–16888 (2011).
90. Casares, D., Escribá, P. V. & Rosselló, C. A. Membrane lipid composition: effect on membrane and organelle structure, function and compartmentalization and therapeutic avenues. *International journal of molecular sciences* **20,** 2167 (2019).

91. Monnard, P.-A. & Deamer, D. W. Membrane self-assembly processes: Steps toward the first cellular life. *The Anatomical Record: An Official Publication of the American Association of Anatomists* **268,** 196–207 (2002).
92. Deamer, D. W. & Pashley, R. Amphiphilic components of the Murchison carbonaceous chondrite: surface properties and membrane formation. *Origins of Life and Evolution of the Biosphere* **19,** 21–38 (1989).
93. Breton, M., Amirkavei, M. & Mir, L. M. Optimization of the electroformation of giant unilamellar vesicles (GUVs) with unsaturated phospholipids. *The journal of membrane biology* **248,** 827–835 (2015).
94. Shimokawa, N. & Hamada, T. Physical Concept to Explain the Regulation of Lipid Membrane Phase Separation under Isothermal Conditions. *Life* **13,** 1105 (2023).
95. Semrau, S. & Schmidt, T. Membrane heterogeneity–from lipid domains to curvature effects. *Soft Matter* **5,** 3174–3186 (2009).
96. Dreher, Y., Jahnke, K., Bobkova, E., Spatz, J. P. & Göpfrich, K. Division and regrowth of phase-separated giant unilamellar vesicles. *Angewandte Chemie International Edition* **60,** 10661–10669 (2021).
97. Cebecauer, M. Role of lipids in morphogenesis of T-cell microvilli. *Frontiers in immunology* **12,** 613591 (2021).
98. Cebecauer, M. *et al.* Membrane lipid nanodomains. *Chemical reviews* **118,** 11259–11297 (2018).
99. Müller, A. *et al.* Daptomycin inhibits cell envelope synthesis by interfering with fluid membrane microdomains. *Proceedings of the National Academy of Sciences* **113,** E7077–E7086 (2016).
100. Nakazawa, K. *et al.* Budding-driven localization of lipid domains at prescribed positions in confined giant unilamellar vesicles (2023).
101. Sarmento, M., Prieto, M & Fernandes, F. Reorganization of lipid domain distribution in giant unilamellar vesicles upon immobilization with different membrane tethers. *Biochimica et Biophysica Acta (BBA)-Biomembranes* **1818,** 2605–2615 (2012).
102. Stögbauer, T, Hennig, M & Rädler, J. Alignment and Deformation of Lipid Bilayer Domains in Vesicles Adhering to Microstructured Substrates. *Biophysical Reviews and Letters* **5,** 153–161 (2010).
103. Honigmann, A. *et al.* A lipid bound actin meshwork organizes liquid phase separation in model membranes. *Biophysical Journal* **106,** 634a (2014).
104. Szabo, A. & Ostlund, N. S. *Modern quantum chemistry: introduction to advanced electronic structure theory* (Courier Corporation, 2012).

105. Hollingsworth, S. A. & Dror, R. O. Molecular dynamics simulation for all. *Neuron* **99,** 1129–1143 (2018).

106. Thornburg, Z. R. *et al.* Fundamental behaviors emerge from simulations of a living minimal cell. *Cell* **185,** 345–360 (2022).

107. Doye, J. P. *et al.* in *DNA and RNA Origami: Methods and Protocols* 93–112 (Springer, 2023).

108. Swegat, W., Schlitter, J., Krüger, P. & Wollmer, A. MD simulation of protein-ligand interaction: formation and dissociation of an insulin-phenol complex. *Biophysical Journal* **84,** 1493–1506 (2003).

109. Brodland, G. W. *How computational models can help unlock biological systems* in *Seminars in cell & developmental biology* **47** (2015), 62–73.

110. Joy, D. C. An introduction to Monte Carlo simulations. *Scanning microscopy* **5,** 4 (1991).

111. Frenkel, D. & Smit, B. *Understanding molecular simulation: from algorithms to applications* (Elsevier, 2023).

112. Metropolis, N., Rosenbluth, A. W., Rosenbluth, M. N., Teller, A. H. & Teller, E. Equation of state calculations by fast computing machines. *The journal of chemical physics* **21,** 1087–1092 (1953).

113. Amazon, J. J., Goh, S. L. & Feigenson, G. W. Competition between line tension and curvature stabilizes modulated phase patterns on the surface of giant unilamellar vesicles. A simulation study. *Biophysical Journal* **104,** 192a (2013).

114. Schwille, P. & Frohn, B. P. Hidden protein functions and what they may teach us. *Trends in Cell Biology* **32,** 102–109 (2022).

115. Tsuji, G., Sunami, T. & Ichihashi, N. Production of giant unilamellar vesicles by the water-in-oil emulsion-transfer method without high internal concentrations of sugars. *Journal of bioscience and bioengineering* **126,** 540–545 (2018).

116. Boban, Z., Mardešić, I., Subczynski, W. K. & Raguz, M. Giant unilamellar vesicle electroformation: what to use, what to avoid, and how to quantify the results. *Membranes* **11,** 860 (2021).

117. Bonnemay, L. & Ruaudel, J. High-throughput micropatterning on 96 well plates using PRIMO contactless photopatterning system (2019).

118. Dreher, Y., Niessner, J., Fink, A. & Göpfrich, K. GeoV: An Open-Source Software Package for Quantitative Image Analysis of 3D Vesicle Morphologies. *Advanced Intelligent Systems* **5,** 2300170 (2023).

119. Harris, C. R. *et al.* Array programming with NumPy. *Nature* **585,** 357–362. `https://doi.org/10.1038/s41586-020-2649-2` (Sept. 2020).

120. Van Rossum, G. & Drake Jr, F. L. *Python reference manual* (Centrum voor Wiskunde en Informatica Amsterdam, 1995).

121. Chilkoti, A. & Stayton, P. S. Molecular origins of the slow streptavidin-biotin dissociation kinetics. *Journal of the American Chemical Society* **117,** 10622–10628 (1995).

122. Weber, P. C., Ohlendorf, D. H., Wendoloski, J. & Salemme, F. Structural origins of high-affinity biotin binding to streptavidin. *Science* **243,** 85–88 (1989).

123. Ren, C.-l., Carvajal, D., Shull, K. R. & Szleifer, I. Streptavidin- biotin binding in the presence of a polymer spacer. A theoretical description. *Langmuir* **25,** 12283–12292 (2009).

124. Aoki, P. H. B., Schroder, A. P., Constantino, C. & Marques, C. Bioadhesive giant vesicles for monitoring hydroperoxidation in lipid membranes. *Soft Matter* **11,** 5995–5998 (2015).

125. Dirscherl, C., Hein, Z., Ramnarayan, V. R., Jacob-Dolan, C. & Springer, S. A two-hybrid antibody micropattern assay reveals specific in cis interactions of MHC I heavy chains at the cell surface. *Elife* **7,** e34150 (2018).

126. Batalov, I., Jallerat, Q., Kim, S., Bliley, J. & Feinberg, A. W. Engineering aligned human cardiac muscle using developmentally inspired fibronectin micropatterns. *Scientific Reports* **11,** 11502 (2021).

127. Engel, L. *et al.* Extracellular matrix micropatterning technology for whole cell cryogenic electron microscopy studies. *Journal of Micromechanics and Microengineering* **29,** 115018 (2019).

128. Théry, M. *et al.* Anisotropy of cell adhesive microenvironment governs cell internal organization and orientation of polarity. *Proceedings of the National Academy of Sciences* **103,** 19771–19776 (2006).

129. Streicher, P. *Studying integrin-mediated cell spreading using a biomimetic system* PhD thesis (2008).

130. Lipowsky, R. *et al.* Droplets, bubbles, and vesicles at chemically structured surfaces. *Journal of Physics: Condensed Matter* **17,** S537 (2005).

131. Jansen, S. *et al.* Mechanism of actin filament bundling by fascin. *Journal of Biological Chemistry* **286,** 30087–30096 (2011).

132. Lukinavičius, G. *et al.* Fluorogenic probes for live-cell imaging of the cytoskeleton. *Nature methods* **11,** 731–733 (2014).

133. Bashirzadeh, Y., Moghimianavval, H. & Liu, A. P. Encapsulated actomyosin patterns drive cell-like membrane shape changes. *Iscience* **25** (2022).

134. Xu, T. *et al.* SOAX: a software for quantification of 3D biopolymer networks. *Scientific reports* **5,** 9081 (2015).

135. Jahnke, K., Huth, V., Mersdorf, U., Liu, N. & Göpfrich, K. Bottom-up assembly of synthetic cells with a DNA cytoskeleton. *ACS nano* **16,** 7233–7241 (2022).

136. Huber, F., Strehle, D., Schnauß, J. & Käs, J. Formation of regularly spaced networks as a general feature of actin bundle condensation by entropic forces. *New Journal of Physics* **17,** 043029 (2015).

137. Lembo, S. *et al.* The distance between the plasma membrane and the actomyosin cortex acts as a nanogate to control cell surface mechanics. *bioRxiv,* 2023–01 (2023).

138. Müller, P. *et al. Shape-Out version 2.15.4: Analysis software for real-time deformability cytometry* `https://github.com/ZELLMECHANIK-DRESDEN/ShapeOut2`.

139. Otto, O. *et al.* Real-time deformability cytometry: on-the-fly cell mechanical phenotyping. *Nature methods* **12,** 199–202 (2015).

140. Miller, C. J. & Davidson, L. A. The interplay between cell signalling and mechanics in developmental processes. *Nature Reviews Genetics* **14,** 733–744 (2013).

141. Heberle, F. A. & Feigenson, G. W. Phase separation in lipid membranes. *Cold Spring Harbor perspectives in biology* **3,** a004630 (2011).

142. Li, Q., Wang, X., Ma, S., Zhang, Y. & Han, X. Electroformation of giant unilamellar vesicles in saline solution. *Colloids and Surfaces B: Biointerfaces* **147,** 368–375 (2016).

143. Beales, P. A., Ciani, B. & Cleasby, A. J. Nature's lessons in design: nanomachines to scaffold, remodel and shape membrane compartments. *Physical Chemistry Chemical Physics* **17,** 15489–15507 (2015).

144. Veatch, S. L. & Keller, S. L. Separation of liquid phases in giant vesicles of ternary mixtures of phospholipids and cholesterol. *Biophysical journal* **85,** 3074–3083 (2003).

145. Robinson, T. & Dittrich, P. S. Observations of membrane domain reorganization in mechanically compressed artificial cells. *ChemBioChem* **20,** 2666–2673 (2019).

146. Lipowsky, R. Multispherical shapes of vesicles with intramembrane domains. *The European Physical Journal E* **47,** 4 (2024).

147. Wongsirojkul, N., Masuta, A., Shimokawa, N. & Takagi, M. Control of Line Tension at Phase-Separated Lipid Domain Boundaries: Monounsaturated Fatty Acids with Different Chain Lengths and Osmotic Pressure. *Membranes* **12,** 781 (2022).

148. Frey, F. & Idema, T. More than just a barrier: using physical models to couple membrane shape to cell function. *Soft matter* **17,** 3533–3549 (2021).

149. Tee, Y. H. *et al.* Cellular chirality arising from the self-organization of the actin cytoskeleton. *Nature cell biology* **17,** 445–457 (2015).

150. Afting, C., Walther, T., Wittbrodt, J. & Göpfrich, K. DNA microbeads for spatiotemporally controlled morphogen release within organoids. *bioRxiv,* 2024–01 (2024).

151. Roder, F., Birkholz, O., Beutel, O., Paterok, D. & Piehler, J. Spatial organization of lipid phases in micropatterned polymer-supported membranes. *Journal of the American Chemical Society* **135,** 1189–1192 (2013).

152. Okada, F. & Morigaki, K. Micropatterned model membrane with quantitatively controlled separation of lipid phases. *RSC Advances* **5,** 1507–1513 (2015).

153. Gordon, V. D., Deserno, M., Andrew, C., Egelhaaf, S. & Poon, W. Adhesion promotes phase separation in mixed-lipid membranes. *Europhysics Letters* **84,** 48003 (2008).

154. Lipowsky, R. & Dimova, R. Domains in membranes and vesicles. *Journal of Physics: Condensed Matter* **15,** S31 (2002).

155. Boedec, G., Leonetti, M. & Jaeger, M. 3D vesicle dynamics simulations with a linearly triangulated surface. *Journal of Computational Physics* **230,** 1020–1034 (2011).

156. Das, S. K., Cenanovic, M. & Zhang, J. A physics-based estimation of mean curvature normal vector for triangulated surfaces. *arXiv preprint arXiv:1902.02271* (2019).

157. Schoenit, A., Cavalcanti-Adam, E. A. & Göpfrich, K. Functionalization of cellular membranes with DNA nanotechnology. *Trends in Biotechnology* **39,** 1208–1220 (2021).

158. Jahnke, K. *et al.* Proton gradients from light-harvesting E. coli control DNA assemblies for synthetic cells. *Nature communications* **12,** 3967 (2021).

159. Khmelinskaia, A., Mücksch, J., Petrov, E. P., Fr anquelim, H. G. & Schwille, P. Control of membrane binding and diffusion of cholesteryl-modified DNA origami nanostructures by DNA spacers. *Langmuir* **34,** 14921–14931 (2018).

160. Khmelinskaia, A., Schwille, P. & Franquelim, H. G. in *DNA and RNA Origami: Methods and Protocols* 231–255 (Springer, 2023).

161. Schoenit, A. *et al.* Tuning epithelial cell–cell adhesion and collective dynamics with functional DNA-E-cadherin hybrid linkers. *Nano Letters* **22,** 302–310 (2021).

162. Jin, C. *et al.* Phosphorylated lipid-conjugated oligonucleotide selectively anchors on cell membranes with high alkaline phosphatase expression. *Nature Communications* **10,** 2704 (2019).

163. Staufer, O., Schröter, M., Platzman, I. & Spatz, J. P. Bottom-up assembly of functional intracellular synthetic organelles by droplet-based microfluidics. *Small* **16,** 1906424 (2020).

164. Hennig, M., Neumann, J., Wixforth, A., Rädler, J. O. & Schneider, M. F. Dynamic patterns in a supported lipid bilayer driven by standing surface acoustic waves. *Lab on a Chip* **9,** 3050–3053 (2009).
165. Yagüe Relimpio, A. *et al.* Bottom-up Assembled Synthetic SARS-CoV-2 Miniviruses Reveal Lipid Membrane Affinity of Omicron Variant Spike Glycoprotein. *ACS Nano* **17,** 23913–23923 (2023).
166. Levario-Diaz, V. *et al.* 1D micro-nanopatterned integrin ligand surfaces for directed cell movement. *Frontiers in Cell and Developmental Biology* **10,** 972624 (2022).